LATTICE DEFECTS IN QUENCHED AND DEFORMED METALS

by

K. A. SHOAIB

A dissertation submitted for the degree of
Doctor of Philosophy at the University of Warwick

APRIL 1970

M E M O R A N D U M

This dissertation is submitted to the University of Warwick for admission to the degree of Doctor of Philosophy. It contains an account of the work performed during the period October 1966 to March 1970 at the School of Physics, University of Warwick under the general supervision of Dr. R.L. Segall. The results described in this dissertation are original, except where specifically acknowledged in the text. No part of this dissertation has been submitted previously for a degree at this or any other University.

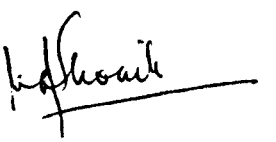

K. A. Shoaib
April 1970

School of Physics,
University of Warwick,
Coventry, England.

ACKNOWLEDGEMENTS

I am grateful to Professor A.J. Forty for making the research facilities of the laboratories at the School of Physics, University of Warwick available to me. I am greatly indebted to Dr. R.L. Segall for his continued interest and encouragement, and valuable suggestions and advice throughout the course of this work. I would also like to thank my colleagues and members of the School of Physics, especially Dr. H. Mykura and Dr. M.H. Lewis for many useful discussions and Mr. I.D. Ward for the excellent maintenance of the electron microscopes and his help in technical problems.

I would like to express my gratitude to Dr. P. Humble of the Division of Tribophysics, CSIRO, Melbourne, Australia for doing invaluable computations for me. I also wish to thank Mr. J.F. Nicholas of the Division of Tribophysics, CSIRO, Melbourne, Australia, Mr. M.H. Loretto and Dr. C.N. Reid of the Department of Physical Metallurgy, Birmingham University, Professor R.B. Nicholson and Dr. G.W. Lorimer of the Department of Metallurgy, Manchester University, and Dr. L.M. Brown, Dr. A. Howie and Mr. M.H. Spring of the Cavendish Laboratory and Dr. J.W. Edington of the Department of Metallurgy, Cambridge University, for various discussions and helpful criticisms.

Finally, acknowledgements are due to the Colombo Plan Authorities for providing me with a research scholarship and to the Pakistan Atomic Energy Commission for granting me leave of absence.

PUBLICATIONS

Some parts of the work described in this dissertation have been published or are in the course of publication. The papers, published jointly with Dr. R.L. Segall, are as follows :

(i) 'Nucleation of point defect clusters in aluminium'. Proc. Fourth European Regional Conf. Electron Microscopy, Rome 1968, Vol. I, p.433. Rome : T.P. Vaticana.

(ii) 'The detection of submicroscopic lattice defects in aluminium utilizing a vacancy supersaturation'. Proc. Roy. Soc. Lond. A. 314, 129 (1969).

(iii) 'Segmented helices in high purity aluminium'. Phil. Mag. (1970). In the press.

Further parts of this dissertation may be submitted for publication in due course.

A B S T R A C T

The conditions under which submicroscopic defects can be revealed due to decoration by the precipitation of vacant lattice sites from a supersaturated solution have been investigated in aluminium. Two particular defects, rows of loops along <110> directions and narrow faulted dipoles with their axes along the same direction, were studied in specimens quenched to and deformed at low temperatures and subsequently aged up to room temperature. The primary observations are that the visibility of these defects is favoured by high purity and a moderate quenching temperature, i.e. by conditions where a moderate supersaturation of vacancies is present after quenching, without the existence of many nuclei for the formation of self-sinks. Thus the conditions under which the faulted dipoles and rows of loops are observed are just those where a decoration phenomenon would be expected.

The decoration technique has been used in quenched and deformed single crystals oriented for single slip to investigate the mechanism of formation of these defects. It is suggested that the observed narrow dipoles along <110> grow from similar submicroscopic dipoles produced from sessile jogs on moving screw dislocations. It is then proposed that the observed rows of loops along <110> are formed in two ways: from the break-up of these submicroscopic dipoles at an early stage, and/or from the break-up of vacancy platelets formed along <110> by the same mechanism. This hypothesis is confirmed by the single crystal experiments which show that the faulted dipoles lie along a particular <110> direction. A 90° jog in a screw dislocation can produce a faulted dipole along either of the <110> directions in the slip plane not parallel to its Burgers vector. The observed dipole direction, for a given tensile axis, was always found to coincide with that predicted from the known stress on the jog.

The occurrence of a high density of helical dislocations is

reported in zone-refined aluminium quenched to temperatures above room temperature and deformed during the quench. The conditions of quenching and deformation indicate that helices are not normally seen in pure metals partly due to the presence of effective competing sinks and partly due to the annihilation of screw dislocations by cross-slip during plastic deformation. The helices observed in aluminium are not circular helices but consist of straight segments. It is shown that these helices are approximately the geodesics on a right prism with a rhombus base, whose generator is the Burgers vector $\underline{b}$ and whose faces are the {111} planes containing $\underline{b}$. This configuration is attributed to the effect of dislocation core energy, the core energy being lowest if the dislocation lies in a {111} plane containing $\underline{b}$ i.e. a glide plane. This observation is used to estimate the ratio of the core energy of a dislocation when it is not on its glide plane and when it is on it.

Finally, a sensitive technique for the detection of radiation damage, by the annihilation of small quenched-in vacancy loops during irradiation, is described. An increase in certain inelastic scattering processes is known to occur under anomalous absorption conditions due to higher electron density at the atom positions. Using the detection technique mentioned above, a similar expected enhancement in displacement damage during anomalous absorption was investigated in the 200 kV electron microscope. Preliminary results suggest that this effect, if present, is small.

CONTENTS

CHAPTER ONE

INTRODUCTION

1.1. Historical

Modern technology is based entirely on the efficient use of appropriate materials, and specially of metals. In order to fully exploit the materials it is essential to have an understanding of their physical properties. The knowledge, gained but lately, about the behaviour of materials has now reached a stage when properties can be designed, not just selected. Metals have been known for their versatility throughout their use over the centuries. Although their macroscopic properties have been familiar for quite some time, the correlation of their bulk behaviour with the microscopic structure is very recent. It is now well-known that many of the physical, mechanical and electrical properties of metals are affected, to varying degrees, by crystalline imperfections of atomic dimensions called point defects.

Point defects include vacant lattice sites, interstitial atoms and impurity atoms, but generally the term is meant to imply structural irregularities, i.e. vacancies and interstitials. Frenkel (1926) was the first to propose that crystals in thermal equilibrium should contain a significant and well-defined concentration of point defects. Schottky and Wagner (1930) elaborated these ideas, and their application to the diffusion process, by their experimental work on ionic crystals. The emphasis soon shifted to metals where, in the absence of any charge effects, the analysis was relatively simple. The stimulus was again provided by the attempt to clarify the nature of self-diffusion in metals. Pioneering work of Huntington and Seitz (1942) and Huntington (1942) on the formation energies of point defects in copper led them to

suggest that self-diffusion in metals occurred by a vacancy mechanism. The behaviour of point defects in metals has since then been investigated at an ever-increasing rate.

The main reason for the vigorous research in this field was the increasing realization of the important influence point defects have on numerous properties of materials. Self-diffusion in metals, diffusion in substitutional alloys, and many processes of solution, precipitation, sintering and polygonization are dominated, to different extents, by the migration of vacancies. While at high temperatures vacancies may cause softening of metals by enabling dislocations to climb over obstacles, at low temperature the interaction of point defects and impurities with dislocations produces hardening and embrittlement. Vacancies play a leading part too in certain aspects of the strength of intermetallic compounds, of fatigue deformation in metals and alloys, and ageing processes in cold-worked alloys. Formation, during irradiation, cold work or quenching, and annihilation during annealing, of point defects partly accounts for the storage and release of energy in metals subjected to these processes. Volume changes due to the dilation and compression associated with point defects are responsible for density changes in materials containing them, while the scattering of conduction electrons by the lattice distortion around these defects contributes to the change in electrical resistivity. Some of these effects, such as fatigue deformation and hardening in metals, and precipitation and ageing in alloys, are of technological importance. Other effects, such as the changes in electrical resistivity, density and the stored energy, are of scientific interest, and have in fact been used for the indirect investigation of point defects.

High concentrations of point defects can be produced in crystals by a variety of processes. Irradiation with energetic particles, plastic deformation, or quenching from high temperatures, have all been used to

produce these defects in non-equilibrium concentrations. The former two methods produce both vacancies and interstitials, while the latter produces vacancies only. This is because the quenched material represents a 'frozen-in' state of the equilibrium concentration of point defects at the temperature where the specimen was quenched from. As the energy of formation of the vacancies is considerably smaller than that of the interstitials the former would be the dominating defects in thermal equilibrium at any temperature (Huntington and Seitz 1942; Huntington 1942). Nowick (1951) and Kauffman and Koehler (1952) experimentally demonstrated that excess vacancies can be successfully quenched in metals and alloys. Quenching thus has an advantage as a means of introducing imperfections because only one type of defect need be considered, making the analysis relatively simple.

The density of the point defects introduced by any of the above methods is greater than that which could be in thermal equilibrium. Thus, if given the chance, these must gradually disappear to restore the equilibrium concentration. If the temperature is high enough for the point defects to be mobile, these would tend to annihilate themselves by several mechanisms. The mechanism through which the defects annihilate is governed by the degree of supersaturation, the temperature, the efficiency and the density of the sinks, and the interactions among the point defects. Infinite sinks, such as surfaces, grain boundaries and pre-existing dislocations, are obvious sites where the point defects can be absorbed. Since this process depends on the availability of a nearby infinite sink, at moderate annealing temperatures the excess point defects can be eliminated by a different process. It was Seitz (1950) who suggested that the point defects might also be annihilated by the formation of internal 'self-sinks'. This formation of self-sinks, i.e. the aggregation of point defects into clusters, occurs because the energy of two or more point defects is less when these are bound together than when they are

isolated. These self-sinks might take different forms. Nabarro (1948) had visualized the formation of prismatic dislocation loops by the condensation of vacancies on a single plane, while Frank (1949, 1950) had described the formation of faulted loops in f.c.c. metals by the collapse of discs of vacancies on the {111} planes. The detailed analysis of Kuhlmann-Wilsdorf (1958) indicated that the collapse of point defect clusters into secondary defects is not a simple process and that many different configurations might occur.

Since its first application to the observation of thin metal foils (Heidenreich 1949; Hirsch et al 1956; Bollmann 1956), transmission electron microscopy has proved to be a very powerful and versatile technique for the study of lattice defects. Though individual point defects are too small to be visible in the electron microscope, small clusters of these defects are well suited for electron microscope examination. The direct observation of secondary defects in metals by this method has confirmed all the predictions made above about the aggregation of point defects. The first observations, by transmission electron microscopy, of point defect clusters in metals which had been quenched, irradiated or deformed were made respectively by Hirsch et al (1958), Silcox and Hirsch (1959b) and Segall and Partridge (1959). Electron microscopy has also revealed a rich variety of different configurations of secondary defects. The four basically different types of defects resulting from the aggregation of point defects were first identified in the electron microscope as prismatic dislocation loops (Hirsch et al 1958), faulted loops (Yoshida et al 1962), stacking-fault tetrahedra (Silcox and Hirsch 1959a) and voids (Kiritani and Yoshida 1963).

1.2. The Nucleation of Point Defect Clusters

There have been several attempts to demonstrate the fact that the formation of secondary defects is essentially a nucleation controlled process since the original suggestion by Brooks (Read Jr. 1953b).

Aluminium and gold are the metals which have been extensively examined, both experimentally and theoretically, for the formation of vacancy clustered defects after quenching. Though considerable experimental evidence has accumulated on the nucleation of defects in quenched aluminium and gold (Meshii 1965; Kiritani 1965; Chik 1965a; Meshii et al 1966; Kiritani et al 1966b, Davis and Hirth 1966b), the theoretical models available (Kiritani 1965; Chik 1965b, Meshii et al 1966; Davis and Hirth 1966a, Davis 1967) are still unsatisfactory and there is some disagreement among the proposers. The confusion that exists in the theoretical treatment of the nucleation of point defect clusters will be obvious from the following brief review of the conclusions drawn by various authors.

In their analysis of the resistivity recovery of quenched gold, de Jong and Koehler (1963) have suggested that the nucleation of tetrahedra occurs over a considerable part of the recovery period. This result however contradicts the experimental observations in quenched gold (Westdrop et al 1964; Mori and Meshii 1964; Chik 1965a, Meshii 1965) where tetrahedron nucleation is found to occur in the initial stages of annealing. However, Chik (1965b) has, in his treatment, succeeded in explaining the experimentally observed dependence of tetrahedron density on the vacancy concentration and the annealing temperature, and the observed kinetics of nucleation.

The nucleation process in aluminium has been analyzed by Kiritani (1964, 1965). The earlier work, based on the idea of a critical sized nucleus, explains some of the qualitative features of defect formation but is quantitatively in disagreement. The later detailed formulation, based on positive and negative reactions, i.e. reactions involving respectively the absorption and the emission of vacancies from clusters, arrives at some surprising conclusions. It predicts no definite critical

size of the nucleus of the faulted loop and assumes the transition from a vacancy disc to a dislocation loop to be continuous through intermediate stages. The role of impurities is treated in terms of the effect these can have on vacancy mobilities and hence on the positive and negative reactions. Thus heterogeneous nucleation, in the sense that the impurities may form nucleation sites, is assumed impossible. Though the nucleation kinetics derived by Kiritani explain his own experimental results qualitatively, they are in conflict with those of Meshii et al (1966) and Chen and Meshii (1966) who predict a critical sized nucleus. Indeed Davis (1967) has succeeded in explaining the experimental results of Kiritani (1965) on the basis of a theory assuming a critical sized nucleus. Kiritani's model is also unsatisfactory in the sense that it does not include heterogeneous effects adequately which, as discussed below, are often predominant.

Recognizing the importance of heterogeneous nucleation Meshii et al (1966) have derived approximate nucleation kinetics based upon the attrition of heterogeneous nucleation sites with the time of ageing. They assume that nuclei have a critical size where there is a sudden gain of stability, or a sudden decrease of energy. While sub-critical clusters are liable to break up, the dissociation of the nuclei is not too likely. In confirmation of their experiments, the authors have defined ranges of critical temperature within which either nucleation, or growth, or annealing of clusters can occur.

An elegant mathematical treatment of the nucleation of vacancy clusters in aluminium and gold has been given by Davis and Hirth (1966a) and Davis (1967). Davis and Hirth (1966a) have applied formal nucleation theory (Hirth and Pound 1963) to develop rate equations for the nucleation of perfect and faulted loops in these metals. These authors assumed a critically sized nucleus, in the

collapsed form, of the pertinent defect. The calculated nucleation rate, which is too low to account for the experimentally observed densities of defects, suggests that negligible amount of homogeneous nucleation takes place and that the nucleation must be entirely heterogeneous. This formulation of Davis and Hirth (1966a) has been criticized (McComb and Meshii 1967) on the grounds that continuum theory and macroscopic energy values have been used to describe a microscopic phenomenon. It was agreed (Davis and Hirth 1967) that the difficulty arose because the size of the nuclei lay in the intermediate region where the application of both the atomistic and the continuum theories is uncertain.

Davis (1967) has subsequently redeemed the application of formal nucleation theory to vacancy clusters by assuming the nucleus to be a non-collapsed disc of vacancies, with its size dependent on the vacancy concentration and the temperature, and by using energy values based on the formation energy of single vacancies. Like the analysis of Meshii et al (1966) the ageing cycle has again been divided into a number of critical ranges corresponding to nucleation, growth or annealing out of defects. The experimental results of Kiritani (1965) have also been explained on this theory assuming a nucleus of definite critical size, and the calculated and observed densities of loops in aluminium have been found to be in reasonable agreement. It is also seen that both the pre-ageing temperature (where nucleation is expected to take place) and the ageing temperature (where nucleation ceases and only growth of the nuclei occurs) investigated by Kiritani (1965) lie in the critical temperature range where nucleation can occur, thus giving the density dependence of the nuclei on the ageing temperature in these experiments.

Despite all the uncertainties in the theoretical descriptions of the nucleation of clusters there is unequivocal experimental evidence

regarding the importance of heterogeneous nucleation on impurities. Dislocation loop density has been found to be higher in quenched aluminium of lower purity as compared to that in zone-refined aluminium (Yoshida et al 1963). Similar increase in loop density in quenched aluminium has also been reported with a decrease in purity by Davis and Hirth (1966b) and Kiritani et al (1969), though the interpretation in these cases is complicated by impurity clustering and vacancy impurity interaction. Dissolved hydrogen is known as well to nucleate voids, whether directly or indirectly, in aluminium, copper and silver (Shimomura and Yoshida 1967; Clarebrough et al 1967).

The marked effect of impurities in the heterogeneous nucleation of defects is particularly well demonstrated in gold. Segall and Clarebrough (1964) found a decrease in the electrical resistivity of gold specimens when annealed at high temperature in oxygen, while a similar anneal in carbon monoxide resulted in an increase in resistivity. Furthermore, electron microscopy of quenched and aged gold specimens, given the two different pre-anneals, showed that the density of stacking-fault tetrahedra was much larger (and their size smaller) in the specimens which had been given a reducing treatment than in those given an oxidizing treatment. The results of resistivity measurement and electron microscopy, taken together, show that a reducing treatment of gold released impurities (which were probably in form of oxides) which acted as sites for the heterogeneous nucleation of tetrahedra. Meshii et al (1966) and McComb and Meshii (1966) also observed a decrease in the number of tetrahedra in gold specimens when these were given oxygen pre-anneals. Similarly, with a decrease in the purity of their samples, Ytterhus and Balluffi (1965) noticed a large increase in the density of vacancy clusters after ageing. Siegel (1966) made a detailed correlation of electrical resistivity recovery and the electron microscopy of aged gold specimens of various purities. He found a considerable increase in the density of vacancy clusters

with decreasing purity and established that certain impurities were more efficient as heterogeneous nucleation sites than others. Further confirmation of these two facts has been reported by Quader and Dodd (1968) and Johnston et al (1968).

The role of impurities in the heterogeneous nucleation of defects is not fully understood, but it is known that impurities can affect quenched-in vacancies in several ways. Firstly, strain fields around impurities affect vacancy clustering process and may help in stabilizing the sub-critical nuclei with which they might associate. Secondly, impurities modify the effective migration energy by forming impurity-vacancy pairs and thus affect the nucleation kinetics. Finally, because of a binding energy between impurities and vacancies during pairing, the formation energy of vacancies is lowered, thereby increasing their concentration. The interpretation of impurity effects is further complicated by the fact that different impurities may behave in different ways. Thomas and Washburn (1963) and Doyama (1965b) have described this behaviour in terms of the impurity concentration relative to the vacancy supersaturation, and the impurity vacancy binding energy.

The discussion given above indicates that, in general, the nucleation of vacancy clusters in quenched metals is largely heterogeneous. The present investigation is aimed at establishing the experimental conditions where the probability of heterogeneous nucleation is minimized. In other words, an attempt is made to create a situation analogous to that in a conventional cloud chamber, i.e. to produce a supersaturation of vacancies which could be used to 'decorate' submicroscopic defects one chooses to introduce. Thus by the condensation of quenched-in vacancies on these submicroscopic defects, this method should enable the observation, in the electron microscope, of defects that would otherwise be invisible.

Aluminium has been selected for the purpose of these experiments as it can be obtained in high purity, is not contaminated by the

atmosphere during quenching, has been extensively investigated, and its elastic constants, stacking-fault energy etc. are reasonably accurately known. Other reasons for the use of aluminium will also emerge in the following discussion. As described in the subsequent chapters, experimental conditions are going to be established where the nucleation of 'self-sinks', i.e. random dislocation loops, is reduced to a minimum, with an adequate supersaturation of vacancies available for decoration.

1.3. Rows of Secondary Defects, and Faulted Dipoles, along <110>

Two obvious ways of introducing submicroscopic defects for subsequent decoration by quenched-in vacancies are by irradiation and by plastic deformation. The second method was used for this purpose in the work described in this thesis. Different types of defects were found to predominate for the two different temperatures of decoration. For a temperature well below room temperature these defects consisted of rows of loops and faulted dipoles along <110> directions, while at a decoration temperature above room temperature dislocation helices composed of straight segments were observed.

Rows of secondary defects aligned along <110>, and faulted dipoles along this direction, have previously been observed in quenched and/or deformed materials. However, the present observations must be distinguished from these, as in a majority of the reported cases these defects have nothing to do with the decoration phenomenon.

There are four mechanisms which could account for the observation of rows of secondary defects in quenched and aged metal foils. Jones and Mitchell (1953) were the first to demonstrate the generation of rows of prismatic loops by stresses around inclusions in a specimen. Two prominent examples of rows of loops punched out due to quenching stresses are those reported in copper (Barnes and Mazey 1963) and magnesium (Lally and Partridge 1966). The sources of these rows are identifiable as precipitate particles in the former and dissolved hydrogen bubbles in the

latter. Such rows are also recognizable, as they emanate along different close-packed directions from a common centre. Furthermore, due to the compressive nature of the strain generating the rows the component loops are of interstitial type. Because of interaction with the quenched-in vacancies the interstitial loops gradually decrease in diameter away from the source, giving the rows a tapering shape.

A second process known to produce rows of loops is the degeneration of helical dislocations. A row of loops results if a helical dislocation intersects a screw dislocation, or a helix, of equal and opposite Burgers vector. A similar annihilation of the screw part of the helical dislocation results under the stress induced bowing of one or more of its segments. Clear-cut cases of rows of loops forming from helices have been reported by Authier et al (1965) in aluminium, by Thomas and Whelan (1959) in Al - 4 wt. % Cu, by Eikum and Thomas (1963) in Al - 5% Mg and by Embury et al (1962) in Al - 7% Mg. The loops in the rows formed in this way are prismatic and of nearly equal size, and have their Burgers vector along the row direction. The loops in such rows also have a characteristic appearance as these are arranged like a stack of plates, so that in long rows, which are at a shallow angle to the foil surface, the loops are viewed edge-on.

The formation of rows of loops by the break-up of dipoles has been observed in zinc by Price (1960, 1961a) and in magnesium oxide by Washburn et al (1960). The dipoles, formed as a consequence of low temperature straining, were seen to break up, as the temperature was raised, into a number of circular loops with about the same total area. It has been suggested that the dipoles decompose for the sake of a reduction in the dislocation line energy which occurs when the spacing between the loops in the rows is greater than 1.57 times their diameter (Washburn et al 1960). This process of 'pinching'

of dipoles has also been considered by Segall et al (1961) in some detail.

The last mechanism for the generation of rows of defects, which is of particular interest, is the nucleation of these rows on the dislocation trails formed along <110> directions during deformation. Apart from occasional observations in silver (Smallman et al 1959-60) and aluminium (Meshii 1965; Kiritani et al 1966a) the reports of rows of defects along <110>, which could be attributed to this mechanism, are confined entirely to gold. The first observations of rows of tetrahedra in quenched gold are those of Clarebrough et al (1964) and Segall and Clarebrough (1964). These authors assume that the rows nucleate preferentially in the strain fields of the observed <110> dipoles in conditions where general nucleation is difficult. Seidman and Balluffi (1964) have correlated their observation of the rows of tetrahedra in quenched and deformed gold with plastic deformation. They suggest that nucleation of the rows of tetrahedra takes place on the dislocation debris along <110> produced by deformation. Kiritani et al (1968) have investigated the effect of plastic deformation on quenched gold to a greater extent. Though they did not find any rows of tetrahedra in specimens given tensile strain they did find some in specimens deformed in bending. They found a higher density of rows in specimens aged alternately at -195°C and 20°C a large number of times. Kiritani et al conclude that the rows of tetrahedra result from the vacancies formed by the motion of jogs along <110>, and that their occurence depends on the mode of deformation but not on the thermal treatment.

All the observations of the rows of defects reported above have been more or less incidental and no effort has been made to optimize conditions for a maximum in the density of these rows. Though proposals have been made that in some cases, such as that of gold,

these rows nucleate on dislocation debris, and that this is not a strong nucleation site (Segall and Clarebrough 1964), quenching variables have not been adjusted to give suitable conditions of decoration or growth. Moreover, the nature of the dislocation debris, and how exactly it formed, has not been analyzed. In the present work the conditions of decoration appropriate for the observation of a consistently high density of rows of defects are fully investigated. The nature of the dislocation trails, and their formation during deformation, is also examined in detail. Due to the fact that, despite extensive electron microscope investigation, the rows of defects in aluminium are almost non-existent, and that there is no obvious reason why this should be so, aluminium has been selected for experimentation.

In quenched gold Segall and Clarebrough (1964) and Seidman and Balluffi (1964) have also reported faulted dipoles along <110> which were presumably formed due to deformation. Since the first observation of narrow faulted dipoles along <110> directions in deformed Ni - 40% Co alloy by Mader (1963) these have been observed in a number of f.c.c. metals deformed at the end of Stage I. Hirsch and Steeds (1963), Essmann (1963), Basinski (1964), Steeds (1966) and Haussermann and Wilkens (1966) have reported faulted dipoles in copper, Steeds (1966) and Rapp (Haussermann and Wilkens 1966) in silver, Steeds (1966) and Ramsteiner (Haussermann and Wilkens 1966) in gold, and Thieringer (Haussermann and Wilkens 1966) in nickel. These very narrow dipoles, which essentially consist of two Frank dislocations enclosing a stacking-fault, have been found to lie along the two <110> directions in the primary slip plane other than the primary Burgers vector direction. Sometimes these faulted <110> dipoles are observed in a bent or zig-zag form with an angle of 120° between adjacent segments.

The formation of a faulted dipole along <110> was first described by Hirsch and Steeds (1963) in terms of the dissociation of a 60° jog

in a moving screw dislocation. The jog is dissociated into a Frank and a Shockley partial, and as the dislocation moves the Shockley glides along on an inclined {111} plane, leaving behind it a strip of fault bounded by Frank partials. Seeger (1964), Seeger and Wobser (1966) and Steeds (1967a) considered the formation of the faulted dipole by the dissociation of an unfaulted 60^0 dipole, resulting in a configuration similar to that of Hirsch and Steeds but with the Frank partials extended on the primary plane. Haussermann and Wilkens (1966) and Steeds (1967b) have used the latter configuration of the faulted dipole for the evaluation of stacking-fault energies from the widths of the observed dipoles. The above two configurations of the faulted dipole are discussed further in the appropriate section of this thesis.

The faulted dipoles observed in these metals of low stacking-fault energy are extremely narrow and faint. It is thus not surprising that similar dipoles have not been reported in deformed aluminium, which has a relatively high γ/Gb value (where γ is the stacking-fault energy, G the shear modulus, and b the magnitude of the Burgers vector). However this is not an argument against their formation in aluminium. It is most likely that the faulted dipoles that are formed are too narrow to be visible in the electron microscope. If these narrow dipoles in aluminium could be induced to grow larger they might become visible in the electron microscope. For example, if a specimen of aluminium were to be deformed in a situation where a carefully controlled supersaturation of vacancies existed, these vacancies might condense on the submicroscopic dipoles causing them to grow. Just such experiments are described in this dissertation, and the observation of comparatively wide faulted dipoles in aluminium is a demonstration of the development of a successful technique of decoration by quenched-in vacancies. The formation of the initial submicroscopic faulted dipoles from sessile 90^0 jogs, in a manner similar to that of Hirsch and Steeds (1963) is also proposed.

1.4. The Observation of Helices in Aluminium

It was mentioned in the last section that in the present work helical dislocations along <110> have also been produced by quenching aluminium to a temperature above room temperature. The formation of helical dislocations by the condensation of vacancies on screw dislocations was first suggested by Seitz (1952). There have been numerous reports of helices in metallic alloys and ionic crystals since these were first observed in calcium fluoride by Bontinck and Amelinckx (1957) using the conventional decoration technique. Amelinckx et al (1957a) have given a detailed mechanism for the formation of helices in terms of climb of the dislocations in near-screw orientation in a supersaturation of vacancies. Tweet (1958) observed helices in germanium, while Dash (1960) demonstrated their formation in silicon in an undersaturation of vacancies. Helices have been described in a number of metallic alloys (see e.g. Thomas 1959; Thomas and Washburn 1963) but the most extensive experimental investigation of helical dislocations in these alloys is that of Thomas and Whelan (1959) on Al - 4 wt. % Cu. These authors were able to account satisfactorily for all the main features observed in this alloy. They attributed the high density of these helices to the preferential condensation of vacancies on existing dislocations because of difficulty of loop nucleation due to vacancy trapping at the solute atoms.

The formation of helices has been theoretically analyzed by a number of authors. Weertman (1957) has shown that the equilibrium form of a dislocation line in the presence of a supersaturation or an undersaturation of vacancies, assuming isotropic line energy, is a curve whose radius of curvature is constant and whose tangent vector keeps a constant angle with the Burgers vector direction, i.e. a circular helix. Mitchell (1962) has also pointed out that there is no activation energy barrier for the nucleation of helical turns up

to a certain number dependent on the vacancy supersaturation. Thomson and Balluffi (1962) have discussed the nucleation of the initial turns of a helix in terms of dissociation of the vacancies, on reaching the dislocation core, into mobile kinks, and the build up of helical turns by the aggregation of ordered arrangements of these kinks.

The above authors have restricted their treatment to circular helices. Helices composed of straight segments, which are of relevance with regard to the present work, have not been considered. One type of curve which satisfies the equilibrium conditions of Weertman (1957), except at a finite number of points, are the geodesics on any prism, since for these the tangent vector makes a constant angle with the generator of the prism, and, except at the prism edges, the curvature is everywhere zero. Such a departure from the circular form would not be expected if the line tension were isotropic, but could occur if the line energy was orientation dependent. These curves which form a 'helix' with straight segments will be referred to as 'segmented helices'.

The work currently described is prompted by two notable deficiencies in previous observations of helices. Firstly, no satisfactory explanation has been proposed for the well known fact that while helices are abundant in many quenched aluminium alloys, they have rarely been found in quenched pure aluminium. It is generally assumed that helices formed in pure metals soon degenerate due to an absence of pinning points. Secondly, a remarkable feature of some of the earlier observations remains unexplained, that is, in a number of alloys and ionic crystals, such as calcium fluoride (Bontinck 1957), sodium chloride (Amelinckx et al 1957b), aluminium-copper (Smallman et al 1959-60), aluminium-zinc (Thomas 1959), lead iodide (Forty 1960, 1961), aluminium-silicon (Westmacott et al 1961), aluminium-magnesium (Embury 1963; Imura and Hashimoto 1966), and beryllium-iron (Morozumi et al 1969) the 'helices' were not circular helices as observed by Thomas and Whelan (1959), but consisted of straight segments. No

investigation has previously been made as to whether these were segmented helices in the strict sense defined above. Embury (1963) has considered these helices as resulting due to anisotropy of climb, while Amelinckx et al (1957b) have suggested that these lie on a specific prism of {001}{110} planes containing the $\langle\bar{1}10\rangle$ helix axis. These authors have however stopped short of any detailed discussion.

It is shown in the present experiments that appropriate quenching conditions can be utilized to effectively decorate the screw dislocations in aluminium by vacancy condensation, thus converting them into helices. The configuration of these helices, which are found to be segmented, has been deduced from the detailed analysis of their geometry, and this can be usefully employed in interpretting the formation of previously reported angular helices.

1.5. Radiation Damage during High Voltage Electron Microscopy

Electron microscopes have until now mainly been employed in the study of materials for the direct observation of minute features. The usefulness of the instrument in this respect has been indubitably proved. A further use to which this instrument can be put to has grown out of the development of microscopes of ever-increasing electron energies. If the electron beam has a high enough energy that it imparts to the atoms of the sample an energy greater than a threshold value, it should be possible to use the microscope for electron irradiation. Such experiments have been carried out recently by Makin (1968a, 1968b) who used a 600 kV electron microscope to produce and observe radiation damage in copper and aluminium, and by Venables and Lye (1969) who used a 100 kV electron microscope for the irradiation of $V_6 C_5$.

The threshold energy for displacement in aluminium is ≈ 16 eV (Iseler et al 1966) which corresponds to a minimum required incident electron energy of ≈ 166 keV to produce displacement of atoms (Makin

1963b). Thus it should be possible to produce irradiation damage in aluminium down to this value of electron energy, though the displacement cross-section would be very low. Simpson and Chaplin (1969), using electrical resistivity measurement, have in fact been able to observe damage down to incident electron energies of 160 keV.

A very sensitive technique, developed to detect the damage produced in aluminium when irradiated in a 200 kV electron microscope, utilizing the annihilation of small quenched-in vacancy loops, is described in the last section of this thesis. This method is used to investigate the enhanced inelastic scattering occurring during the anomalous absorption of incident electrons in aluminium. The wave function of the incident electron inside the crystal is represented, on the two beam dynamical theory of electron diffraction, by a linear combination of two Bloch waves (Howie and Whelan 1961). The phenomenological explanation of anomalous absorption (Hashimoto et al 1962) is based on the consideration that one of these Bloch waves has its maxima between the atomic planes and the second on the atomic planes. The second wave, being concentrated in the vicinity of atoms, thus suffers greater inelastic scattering. Experimental evidence to this effect is provided by the low transmission when the deviation parameter w ($= s\xi_g$) < 0 (i.e. when Bloch wave 2 dominates) and by the observation of increased X-ray emission from dark absorption bands (Hirsch et al 1962; Duncumb 1962; Hall 1966). The technique for the study of radiation damage described above, which is sensitive to small changes in the displacement damage, is particularly suited to this type of investigation.

1.6. General Layout of the Thesis

The various aspects of the investigations reported in this dissertation can be conveniently divided into a number of chapters. Chapter 2 summarizes the experimental procedure adopted in general, and describes the materials, methods and the techniques used. Chapter 3 is devoted to the establishment

of appropriate conditions for the decoration of submicroscopic defects, introduced by deformation, in aluminium. Variables such as specimen purity, vacancy supersaturation, ageing characteristics etc. are investigated in detail to optimize these conditions. The variation in the density of the observed rows of dislocation loops along <110> is used as a criterion for the best visibility of defects. It is shown that the optimum decoration conditions can be rationalized in terms of creating a situation where the nucleation of self-sinks is difficult, although an adequate vacancy supersaturation is still maintained.

Chapter 4 deals at length with the mechanism of formation of rows of loops and faulted dipoles in quenched and deformed aluminium. The role of deformation in the production of these defects is examined in detail. A mechanism for the formation of narrow faulted dipoles along <110> from sessile 90^{o} jogs on moving screw dislocations is suggested. It is then proposed that the rows of loops along <110> are formed in two ways : from the break-up of these dipoles at an early stage, and/or from the break-up of vacancy platelets formed along <110> by the same mechanism, but without the intermediate stage of dipole formation.

Chapter 5 investigates the occurence of segmented helical dislocations in aluminium. It is shown that a high density of such helices can be produced in zone-refined aluminium under suitable conditions of quenching. The geometry of these helices is analyzed and they are shown to be geodesics on a {111} glide prism. The observation of segmented helices in a very pure and almost elastically isotropic material under specific quenching conditions is used to obtain some general information about dislocation behaviour.

Chapter 6 reports some preliminary experiments on irradiation damage in aluminium in a 200 kV electron microscope. Annihilation, during irradiation, of small vacancy loops in a previously quenched specimen is shown to be a very sensitive method for the detection of damage. This

technique is employed in the study of anomalous absorption and it is demonstrated that the contribution of displacement events, if any, to this effect is small. Chapter 7 concludes by giving a summary of the results, and suggests, on this basis, further experiments that might be scientifically useful.

All the electron microscope plates in this thesis have been printed emulsion side upwards so that the micrographs represent the specimen as viewed along the direction of the electron beam. This is consistent with the micrographs in Mazey et al (1962), Silcock and Tunstall (1964) and Loretto et al (1966) but inconsistent with those in Hirsch et al (1965a). 'Foil normal' has been used to imply the upward drawn normal to the foil, and hence it makes an acute angle with the upward drawn normal to the micrographs. 'Beam direction' has been defined to be identical with the upward drawn normal to the micrographs and is hence opposite in sense to the actual current of electrons.

The magnification marks on the micrographs correspond to 0.5 μm, unless otherwise stated, while the arrow marks indicate the reflecting vector $\underline{g}$. It should be pointed out that, consistently with previous publications (Shoaib and Segall 1968; Shoaib and Segall 1969; Segall and Shoaib 1970), the 180^{0} rotation between the micrograph and the diffraction pattern has not been incorporated when marking $\underline{g}$. This would introduce an error in the determination of the sense of the Burgers vector if a method such as that of Groves and Kelly (1961, 1962) or of Mazey et al (1962) is used where a correlation of the diffraction pattern with the micrographs is necessary (to determine the sense of tilt for example). For the Burgers vector analysis in the present work such a correlation was not required. The micrographs were consulted only to see if a defect was in contrast or not in a particular reflection. The sense of tilt of the specimen was determined either from the actual tilt of the goniometer stage or from the movement of the Kikuchi pattern.

CHAPTER TWO

EXPERIMENTAL PROCEDURE

2.1. Introduction

The investigation of point defects requires their production in high enough concentration so that their interactions and effects may be observable. It has already been pointed out that quenching from high temperatures produces a supersaturation of only one type of defect, i.e. vacancies, and hence the data are easier to manipulate. The quenching process is also simpler to perform as no elaborate equipment is required. This chapter describes the method of quenching used, and the general techniques involved in sample preparation before these can be quenched or observed in the electron microscope. The usual procedure consisted of quenching thin sheet specimens in suitable media, giving them the appropriate deformation treatments and ageing them adequately. The specimens were then thinned by electrolytic or chemical polishing techniques and observed in the electron microscope. All these stages are described in detail in the following sections while the combination of conditions required to achieve the desired results are discussed, where appropriate, in the subsequent chapters.

2.2. Specimens used for Quenching

The experiments were conducted mostly on pure aluminium, though some aluminium alloys were also briefly investigated. Three different grades of aluminium were used, 99.99% Al, 99.999% Al and zone-refined (nominally 99.9999%) Al, generally referred to as Al 4N, Al 5N and Al 6N in the following chapters. Al 4N ('British Super Pure') was supplied by British Aluminium Co. Ltd., Al 5N ('Super Raffinal') by Mining and

Chemical Products Ltd., and Al 6N by Swiss Aluminium Ltd. The alloys investigated were Al - 4 wt. % Cu, acquired from Dr. H.H. Jacobs at Tube Investments (Cambridge), and Al - 7 wt. % Mg, obtained from Dr. J.W. Edington at the Dept. of Metallurgy, Cambridge University.

To get a fast quenching rate specimens have to be quenched in form of thin sheets. While Al 5N and the alloys were in the form suitable for quenching, Al 4N was in the shape of a bar and Al 6N as an ingot. In the latter two cases thin sheets, 75 to 200 μm thick, had to be prepared by rolling down spark machine cut, 0.5 cm thick, slices. The rolling was done on carefully cleaned, hand operated rollers, and the reduction from 0.5 cm to the required thickness was accomplished in about 10 to 15 steps. At the final setting of the rollers a number of passes of the rolled sheets were given through the rollers to get uniform thickness (the variation of thickness after this being within 10% of the mean). Two or three times during the rolling process the surface of the sheets was cleaned by light etching (in 25% HCl, 25% HNO_3 and 50% water, plus a few drops of HF) or polishing (in NaOH solution) and the sheets given 5 min. anneals at 600°C to soften them. The foils were given a final etch or polish after the rolling and annealed for 30 min. at 600°C. A rough check on the purity of Al 6N after rolling was made by comparing the resistivity ratio, at 20°C and -195°C, of rolled Al 6N with that of the Al 5N foil. The rolled Al 6N was found to be purer than Al 5N.

The specimens used for quenching were 2 to 3 mm wide and about 10 cm long, cut lengthwise along the direction of rolling. All the preliminary experiments were performed with polycrystalline foils. The grain size in annealed Al 4N and Al 5N was about 1 mm in diameter, while the grain size in Al 6N was on the average over twice as large and elongated in the rolling direction. The thickness

of the specimens used for quenching varied and could be roughly classified as follows :

(1) Al 6N, polycrystalline - usually 75 to 100 μm thick, though sheets 150 to 200 μm thick were also used;

(2) Al 6N, single crystals - between 150 and 200 μm thick;

(3) Al 5N - uniformly rolled 25 μm thick foils were used;

(4) Al 4N - thickness varied between 75 and 100 μm;

and (5) Al - 4% Cu and Al - 7% Mg - thickness about 75 μm.

For an exact analysis of deformation effects, experiments were conducted on single crystal sheets of Al 4N and Al 6N. These large grains were grown by critical strain-anneal method (Carpenter and Elam 1921; Honeycombe 1959; Holwech and Risnes 1967) in polycrystalline foils, 200 μm thick, cut in size ready for quenching. The polycrystalline sheets were pre-annealed for 30 min. at 600°C and then carefully strained a critical amount. The surface layer, which would have had a non-uniform strain distribution, was removed by a light etch and the sheets were then left to anneal for 48 hours at 630°C. The critical strain required depends on the thickness and the purity of the specimen, and on the initial grain size. The value of this strain is in general higher for smaller thickness, greater purity and larger initial grain size (Holwech and Risnes 1967). The critical strain was determined by a number of preliminary experiments and, for a foil thickness of 200 μm, was found to be 3.5%, for Al 4N and 4.5% for Al 6N. (For an Al 6N foil 150 μm thick this value was about 5.5%). The process of grain growth was also found to be very sensitive to the uniformity of temperature over the whole specimen during the final anneal. The best results were obtained using oven type furnaces where the temperature gradient is small.

The success rate in the production of large grained foils, even under optimum conditions, was quite low. Out of the sheets given the

strain-anneal nearly half in Al 4N and a quarter in Al 6N had large grains. The good foils used for experiments usually consisted of two or three large grains in the middle of the specimen, each grain extending across the total width (≈ 3 mm) of the foil and varying from 1 to 3 cm in length. X-ray back-reflection Laue method (e.g. Barrett and Massalski 1966) was used to determine the foil normals and the tensile axes of these large grains. The grains seemed to have retained some of their rolling and annealing texture, and the tensile axes tended to be nearer the 001 corner of the [001][101][111] stereographic triangle. A similar distribution of orientations in single crystals of high purity aluminium, grown by critical strain-anneal method, has been observed by Stubicar et al (1970). The grains chosen for single-slip experiments were such that they lay at least 5^{o} away from symmetry axes and 10^{o} away from the corners.

Some uni-directional deformation experiments were also carried out on bulk single crystals of Al 4N. These single crystals had a gauge length of 10 mm and a gauge diameter of 9.5 mm, and were also grown by a strain-anneal method. The value of the critical strain in this case was as low as 1.5 - 2.0%

2.3. The Quenching Technique

Aluminium is an easy material to quench as it does not interact with the atmosphere. Though a thin layer of oxide forms on the surface when aluminium is heated in air, its thickness does not exceed 200 Å. Thus aluminium need not be quenched in vacuum or in an inert atmosphere.

Al - 4% Cu and Al - 7% Mg present some difficulty in this respect as the solute atoms are oxidizable. Further, the specimens must first be solution treated for some time, at a temperature above that of solute solubility to homogenize them. Both the alloys were solution treated at 550^{o}C for times varying between 15 min. and 15 hours. The exact composition of these alloys after the solution treatment is

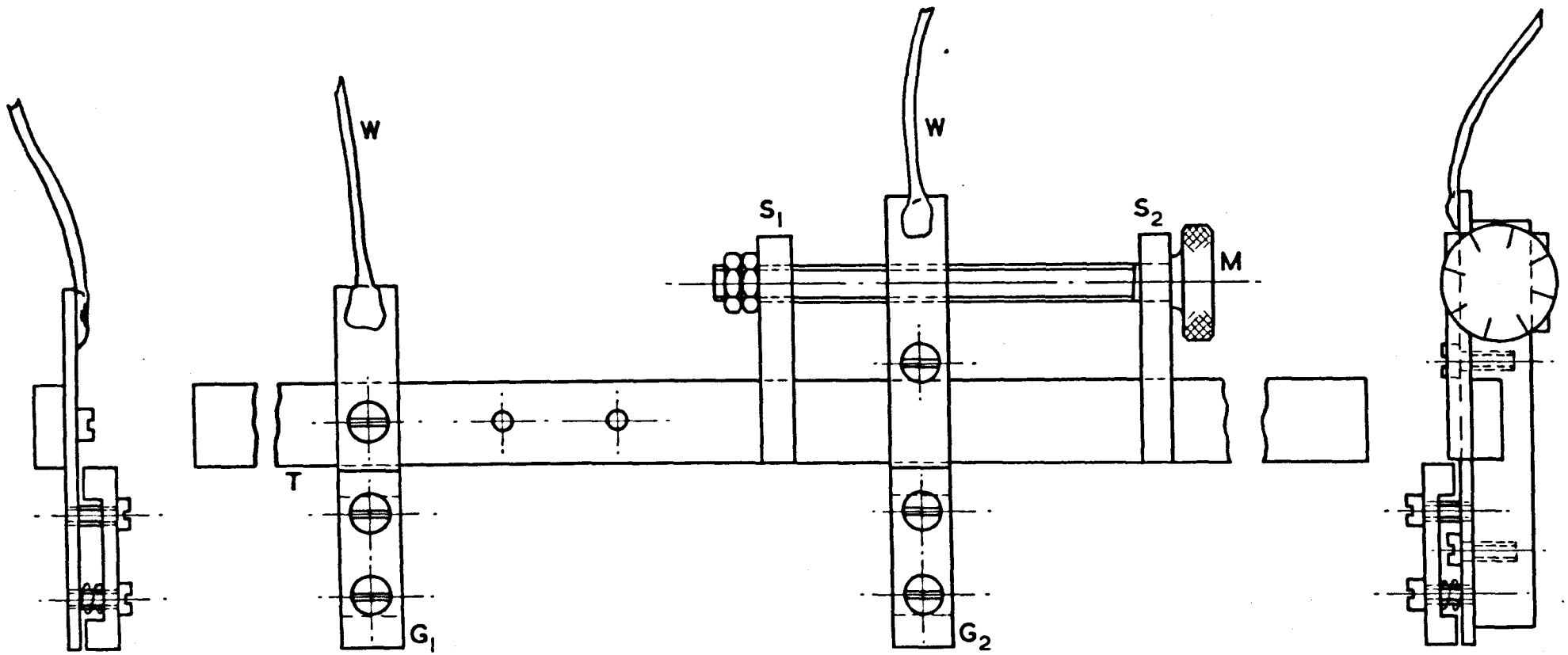

Figure 2.1. THE QUENCHING JIG.

however doubtful. Oxidation of Al-Cu was indicated by slight blackening of the surface when held at 550°C for 15 min. in air. Similarly a 48 hour anneal in vacuum led to some tarnishing of the surface of the specimen. The situation is much worse in the case of Al-Mg. Heating at 550°C for only 5 min. in air or nitrogen results in appreciable blackening of the surface, while after 15 min. the entire surface is covered with a black deposit. An electron probe analysis was carried out of a specimen of Al - 7 wt. % Mg which had been given a solution treatment of 14 hours at 540°C in air. It showed that nearly all the magnesium had come to the surface and the magnesium content in the interior had been reduced to 0.5% only.

The process of quenching consists in heating the specimen to a desired high temperature and then plunging it suddenly into a liquid at a much lower temperature. A brief review of various quenching methods has been given by Doyama (1965a). In the present series of experiments a quenching process employing direct resistance heating of the specimen was used. A simple rig was used for this purpose which enabled the specimens to be heated by passing current and also to be deformed a controlled amount. This rig, illustrated in Figure 2.1, consisted of a 15 inch long tufnol strip, T, which carried two brass grips, G_1 and G_2, for holding the specimen. One of these grips, G_1, was fixed firmly to the strip T. The grip G_2 could be moved along T, between the two stops S_1 and S_2, by means of a long screw M, the grip moving 1 mm for each turn of the screw. The two grips were soldered to thick wires which were connected to a 2 volt, 0.5 kVA step-down transformer. This transformer was fed from the mains through a variac so that the current through the specimen could be controlled. The specimen, fixed between the two grips, could be heated by turning up the current. A typical value of the heating current was about 15 amps at 1 volt. The specimen could also be

deformed by turning the screw N and moving the two grips apart.

When performing a quench, the ends of the specimen were fixed between the two grips G_1 and G_2 by tightening little screws on them. The quenching jig was held manually above the quenching bath with the edge of the specimen parallel to, and its wide face perpendicular to, the surface of the quenchant, and as near it as possible. The specimen was slowly heated up to the required temperature by passing current through it and kept at the final setting for a while to let the temperature stabilize. It was subsequently quenched by plunging the specimen into the quenching medium, and (a second person) turning the current off simultaneously. The specimen was then snipped off at the two ends and removed, or left, for the ageing treatment. In many cases a two-step quenching procedure was adopted, i.e. the specimen was quenched down to a medium at low temperature through a fast quenchant at a higher temperature. The two quenching media, at the appropriate temperatures, were kept side by side in insulated baths. The specimen was first quenched into the fast medium and then immediately afterwards into the second medium at low temperature. The transfer between the two baths took less than half a second.

The quenching jig was designed for use inside a glove box, with the electrical connection via a lead-through. By using a closed enclosure specimens could be quenched in different atmospheres, and the draughts due to specimen heating minimized. The atmospheres used, apart from air, were dry nitrogen, (white spot) hydrogen and (white spot) forming gas (20% hydrogen, 80% nitrogen). A continuous flow of the gas, at a pressure ≈ 2 in. of water above atmospheric, was maintained throughout the quench. Considerable care was taken when hydrogen or forming gas was used, as at high temperature hydrogen combines with air with an explosive reaction. The outlet of the gas flow from the glove box was through a one-way valve which allowed no entry of air. After mounting the specimen on the quenching jig, and placing the various

quenching paraphernalia inside the glove box, the port holes were closed and the glove box flushed with hydrogen or forming gas for half an hour. After this operation, and before heating the specimen for the quench, a remotely controlled test filament, fixed inside the glove box, was heated momentarily to check if the atmosphere inside was safe.

Accurate measurement of the quench temperature was not required for the purpose of the experiments described, as no quantitative deductions based on this temperature are made. The temperature distribution is not uniform all along the length of the specimen anyway, the temperature being highest in the centre and gradually falling off near the ends due to thermal conduction by the grips and the leads. Nevertheless, a number of methods were surveyed to see if a simple and quick determination of exact temperature was possible. Optical pyrometers are unsuitable for temperature measurement below 700^{o}C and for small samples. Measurement of temperature by means of a thermocouple fixed onto the specimen was not very successful. Spot-welding of the fine thermocouple junction to the specimen led to a cooling of the surrounding area so that the thermocouple did not read the actual temperature of the specimen. Improvement could be made by carefully trimming the specimen to compensate for the heat conduction of the thermocouple. This, however, raised difficulties during the deliberate deformation of the specimen, as, due to the variation in width, it made the strain non-uniform along the length of the specimen. There were also instances of the specimen tearing at the welding point during deformation. The change in the resistivity of the hot zone can also be used for the measurement of temperature. Both these methods, if used, make each quenching operation quite complicated, with every specimen being specially cut and trimmed and the thermocouple junction or the potential leads spotwelded on.

Visual judgement, in darkened surroundings, of the glow from the

heated specimen was finally adopted for the estimation of the quench temperature. The two temperatures where a determination by this method is accurate are 520°C, where the specimen just becomes visible, and 660°C, where a molten zone appears. With some practice it is possible to judge the temperatures in the in-between range to within ± 15°C. A refinement of this technique was attempted by comparing the glow from the heated specimen with that from a properly trimmed reference dummy, fixed with a thermocouple and kept at the required temperature. The improvement, however, was not significant as the comparison was made difficult by the narrow width of the specimen and the non-uniformity of the temperature along it.

The quenching temperatures investigated in pure aluminium ranged between 500°C and 650°C. As the temperature during heating of the specimen is non-uniform along the length, only samples taken from the centre of the hot zone were examined in the electron microscope. The specimens of Al - 4% Cu and Al - 7% Mg were all quenched from 550°C after being given a 5 to 15 min. solution treatment at this temperature.

In some of the cases a second method of quenching, with the specimen heated in a furnace, was also used. The specimen was fixed in a rectangular tungsten wire frame, approximately 6 cm x 1 cm, which was then suspended by means of a fine wire in the hot zone of a vertical tube furnace. A vertical quartz tube led to a beaker, containing the appropriate quenching medium (usually brine solution), which was placed just below the furnace with the liquid surface about 8 inches below the specimen. After the temperature of the specimen had equilibrated with that of the furnace, which had been pre-set to the desired quenching temperature, the wire holding the specimen was cut, letting the specimen fall into the quenching fluid. This method of quenching is however known to give a slower quench (Cotterill and Segall 1963) than that described previously, though it has the advantage that the distribution of (quench) temperature over the specimen is uniform. The quenching temperature is again not accurately

known as the specimen cools down before hitting the surface of the quenchant.

2.4. Quenching Media and the Ageing Process

Quenching consists of immersing the hot specimen in a liquid to lower its temperature rapidly. The choice of the quenching medium is determined by the temperature down to which the specimen is to be quenched and by the quenching speed required. The former depends, of course, on the freezing point of the liquid and the latter on its heat transfer properties.

The quenching cycle consists of three stages. During the 'vapour-blanket' phase, associated with high quench temperature or a volatile quenching medium, an envelope of quenchant vapour, generated by the heated specimen as it is immersed, slows the heat transfer to the surrounding medium. As the specimen temperature drops below a 'characteristic temperature', the barrier collapses and rapidly boiling liquid contacts the metal. The quench rate is highest in this 'vapour-transport' stage and the heat is removed by the vaporization of the quenchant. The last phase begins when the temperature of the specimen drops below the boiling point of the quenching medium. During this 'liquid-cooling' stage the quenchant constantly contacts the specimen surface and the cooling is by conduction and convection. The quenching stops when the specimen reaches the temperature of the bath.

The quenching media used, and the attainable quench rates for thin foil aluminium specimens, quenched from 600°C, are given in Table 2.1. The values of the quenching rates given are for the initial part of the fast linear cooling region in the vapour-transport phase. The quenching rate given for silicone oil is actually for a quench from 500°C (Lorimer 1967), and that for a quench from 600°C would be slightly higher. The quench rate for dimethyl-sulphoxide water mixture was not measured, but the density of the quenched-in defects showed it to be of

Table 2.1. Quenching Rates in various Media

(For thin foil aluminium specimens quenched from 600°C)

Quenching Medium	Temperature of the quenching bath (°C)	Quenching Rate $^{o}C\ sec^{-1}$	Reference
Iced brine	-30	50,000	Kiritani et al (1969)
Water	20	30,000	Kiritani et al (1966b)
Eutectic mixture of $CaCl_2$ and water	-40	14,000	Doyama and Koehler (1964)
Methyl alcohol	-90	9,000	Kiritani et al (1969)
Silicone oil	20	1,500	Lorimer (1967); see text
Dimethyl-sulphoxide water mixture (2:1)	-70	-	see text
Liquid nitrogen	-195	750	Kiritani et al (1969)

the same order as that of silicone oil. Saturated brine is known to be the fastest quenching medium for aluminium for a quench from 600°C or above. Lorimer (1967) has found that brine is slower than water if the specimens are quenched from 500°C. This is attributed to the fact that for such quenches there is no vapour-blanket stage for either water or brine and the linear cooling rate, during the vapour-transport phase, is slower in brine due to higher viscosity. In quenches from 600°C or above, the vapour-blanket stage occurs at a higher temperature in the brine solution than in water and hence the duration of time the specimen spends in this slow cooling phase is reduced in brine quenches. The extended vapour-blanket stage is also responsible for the low quenching speed of liquid nitrogen. The 'characteristic temperature' in liquid nitrogen has been found to be -150°C (Lorimer 1967) and thus almost

the entire quenching cycle consists of slow cooling.

In the present set of experiments specimens were quenched down to temperatures between -90°C and +90°C using appropriate quenching fluids. In many cases fast two-step quenches were made to -195°C in liquid nitrogen. In these quenches the two quenchants were brine at 0°C and liquid nitrogen, with the specimen being quenched first into brine and immediately afterwards into liquid nitrogen.

The procedure adopted for ageing the specimens was a simple one. In general the specimen was allowed to warm up, or cool down, from the temperature of the quenching bath to room temperature at a slow and gradual rate. As the exact determination of, say, the nucleation temperature of the defects was not envisaged constant temperature ageing was thought to be unnecessary. Certain difficulties of interpretation may also arise if a constant temperature ageing process is used, which it would not be possible to clear up in a limited number of experiments. Moreover, preliminary experiments showed that the nucleation of the defects that are the subject of this thesis was not very sensitive to the ageing treatment. These points are discussed further in the following chapter.

In case of the quenches made to temperatures between -90°C and +90°C the ageing method was particularly simple : the specimen was left in the thermally insulated quenching bath which was allowed to slowly come up, or down, to room temperature. For the specimens given a fast two-step quench into liquid nitrogen an improved form of ageing bath was used which was essentially meant to be a constant (low) temperature bath. It consisted of two dewars of different diameters. The smaller dewar, which contained the ageing fluid - iso-pentane in most cases - was fixed inside the bigger one. The space between the walls of the inner dewar was unevacuated but could be evacuated by means of a rotary pump. To get the ageing fluid down to the required temperature liquid nitrogen was poured into the outer dewar, and when the desired temperature

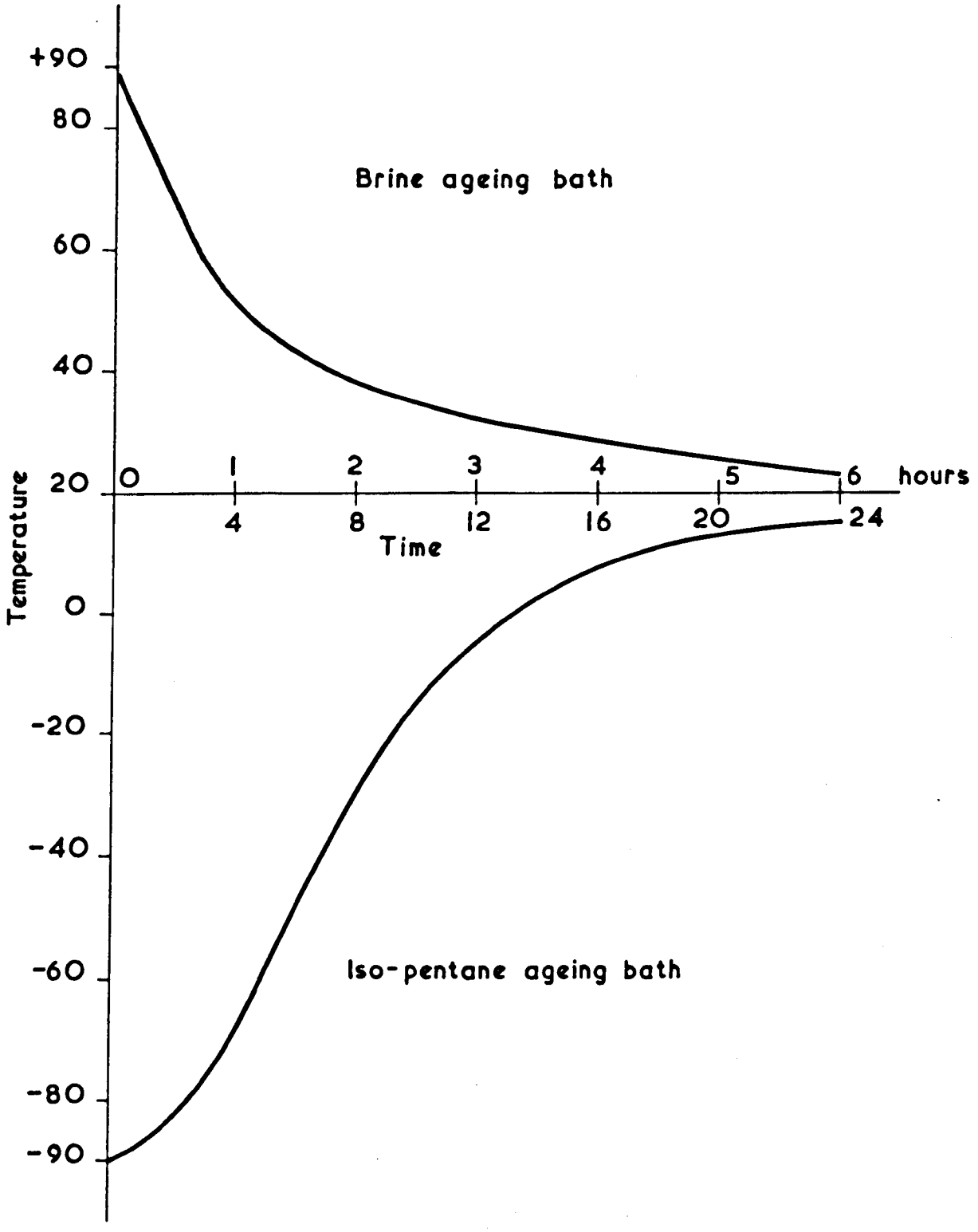

Figure 2.2. TEMPERATURE-TIME CURVES FOR THE AGEING TREATMENT.

was reached the inner dewar was effectively insulated by evacuating the space between its walls. If need be the ageing bath could be raised to a higher temperature by means of a heating filament immersed in the ageing fluid.

The specimens which were fast quenched to liquid nitrogen were up-quenched to the iso-pentane bath at various temperatures between -90°C and -40°C or to brine at 0°C, and left to warm up very slowly to room temperature. The time taken during the transfer of the specimen from the quenching bath to the ageing bath was less than 1 sec. It is assumed that due to the low temperature of the specimen no significant ageing took place during this short interval of time. The temperature-time curves for the two different gradual ageing up or down processes are shown in Figure 2.2. The upper curve corresponds to ageing down from +90°C to room temperature in the brine quenching bath. The lower curve is for gradual ageing up from -90°C to room temperature in the iso-pentane ageing bath.

2.5. Deformation Treatment

The quenched specimens were subjected to a planned, carefully controlled, deformation treatment. Three types of experiments were conducted (a) quenching the specimen without deliberate deformation; (b) deforming the specimen after the quench; and (c) deforming the specimen during the quench.

Some deformation of the specimen due to the quenching process itself is unavoidable and these effects have been discussed by Jackson (1965) and Takamura (1965). This deformation is mainly due to two factors, the thermal strain due to differential contraction of the surface and the interior of the specimen during the quench (which for thin sheet specimens is expected to be small), and the accidental strain when the specimen hits the surface of the quenchant. During the

two step quenches into liquid nitrogen through brine in the present experiments, some deformation could also be associated with the freezing of a layer of brine onto the surface of the specimen. Nevertheless, some experiments were done where attempt was made to minimize all possible deformation during quenching. This was done by fixing the specimen loosely in between the grips of the quenching jig so that no tensile deformation due to lengthwise contraction of the specimen may occur during the low temperature quenches. Moreover, extreme care was taken during the quenching operation that the specimens went exactly edge-on into the quenching medium, and in the handling of the specimen before and after ageing.

In the experiments on deformation after quenching, the specimen was strained immediately after the quench into the final bath, and hence at the temperature of this bath. Various temperatures of deformation were studied by quenching the specimens down to different temperatures and deforming them there. The specimen was fixed taut between the two grips before quenching, and was pulled immediately after the quench by turning the screw M. Depending upon the amount of deformation the straining process took 1 to 5 sec. The approximate value of strain was controlled by giving the screw M an appropriate number of turns, which could be easily calculated from the length of the specimen and the pitch of the screw.

It is possible to deform the specimen only an approximate amount in the way described above. An accurate measurement of strain was carried out each time by measuring the distance between fiduciary marks on the specimen. Faint marks, at 5 mm intervals, were made on the annealed specimen prior to the quench. The distance between the marks was read before the quench and the specimen fixed carefully on the quenching jig to avoid any accidental deformation. The distance between the fiduciary marks was read again after the completion of quenching and ageing, and the strain calculated. The accurate measure of the strain obtained this way was usually found to be within ± 20% of the approximate value calculated from the fractions of the

screw turns. The measurement of strain was generally found to be reasonably uniform within each grain in case of large grained foils, and uniform overall for fine grained polycrystalline foils. A useful measure of strain could only be obtained above a value ≈ 0.5% as the range below this was dominated mostly by uncontrolled deformation. Evidence of accidental deformation was also observed in some cases when the measured value of strain was found to be non-uniform, and abnormally high in places. This was confirmed by the observation of high dislocation density in these regions in the electron microscope.

Experiments were also carried out in which the specimen was deliberately deformed during the quench. This was achieved by removing all the slack in the specimen, produced due to thermal expansion, when at the quenching temperature by turning the screw M to move the two grips G_1 and G_2 apart. Contraction in length during the quench to a lower temperature caused the tensile deformation of the specimen. From the value of the coefficient of thermal expansion of aluminium it can easily be calculated that a quench from 650°C to 0°C would result in a strain $\lesssim$ 2%. This was verified in actual experiments by the measurement of strain from fiduciary marks as outlined above.

In the series of experiments described in this dissertation the tensile strain investigated was in the range 0 to 8% for the specimens deformed after the quench, while it was 1.5 to 2% in case of deformation during the quench. Various temperatures of deformation, between 0°C and -195°C, were examined in the former case, while for the latter the deformation was continuous over the entire range of cooling during the quench.

2.6. Electron Microscopy

Transmission electron microscopy was used extensively for the direct observation of clustered vacancy defects and the dislocation structure. As thin foils only a few thousand Angstroms thick are

transparent to the electrons in conventional microscopes, and as the usual thickness of the specimens is much greater than this, specialized techniques have to be used to suitably thin down the specimens. Some of these techniques have been reviewed by Tegart (1959) and Hirsch et al (1965b). The thinning or the polishing techniques, and the polishing solutions, used in the present work are given in Table 2.2 and are discussed below in detail.

Thin sheet aluminium specimens were polished in the perchloric-ethanol solution given in the table. The beaker containing the polishing solution was surrounded by a jacket of ice to keep the temperature near zero. This temperature gives a good polish and the solution, which is known to be explosive, is also safe to use. During polishing the temperature was never allowed to exceed $30^{o}C$. The cathode used was an aluminium sheet and the specimen, held by a pair of tweezers at the end which was cooler during quenching, formed the anode. The variable voltage was supplied by a 30 volt, 6 amp, D.C. source. The specimen was polished by immersing about a cm length in the electrolyte and using a value of voltage inside the polishing plateau. Depending on the thickness of the specimen, it took 10 sec. to 10 min. to thin down. The thinning occurs round the edges of the specimen and it was visually judged from the appearance if it had adequately polished. The specimen was then taken out of the polishing bath, washed by squirting methanol over it, and dried in a stream of warm air.

It was observed that larger thin areas resulted for smaller thicknesses of the initial specimens. It is also known that the polish is more uniform if the specimen is kept moving during the polishing operation. Furthermore, the sample polishes better if the voltage used is at the higher end of the polishing plateau. However, one has to be a little careful, for if this voltage is exceeded, resulting in a sharp increase in the polishing current, a thin film (probably an oxide) tends to form

Table 2.2. Polishing Techniques used in Specimen Preparation

(An aluminium cathode used in the electrolytic polishing methods)

Material	Polishing Technique	Polishing solution	Voltage V	Current Density Acm^{-2}	Temperature ^{o}C	Reference
Aluminium	Electrolytic Window	20% perchloric acid 80% ethyl alcohol	12-15	0.1	<0	Tomlinson (1958)
Aluminium	Electrolytic P.T.F.E. holder	40% acetic acid 30% phosphoric acid 20% nitric acid 10% water	20-25	10	<0	Dawe and Dewey (1963)
Al - 4% Cu	Electrolytic Window	30% nitric acid 60% methyl alcohol 10% glycerol	15-20	0.2	<-30	Jacobs (1969)
Al - 7% Mg Al - 0.5% Mg	Chemical Immersion	65% phosphoric acid 17.5% sulphuric acid 17.5% nitric acid	-	-	>90	Edington (1969)

on the surface of the sample which is difficult to polish off. Cleaner thin foils are also obtained if the time interval between taking the specimen out of the electrolyte and washing it is kept as short as possible.

The polished sample was sandwiched between a filter paper and a tissue paper and a part of the thinned edge, about a mm square, was cut off using a sharp razor. The thin foil was then lifted off with fine vacuum tweezers, put between two 100 mesh grids, and then into the electron microscope specimen holder. The thin foils could also be stored, almost indefinitely, under vacuum.

The window technique is suitable only for samples less than 250 μm thick. In case of bulk specimens of aluminium a different method of polishing was used. Slip plane slices, 1 mm thick, were cut from the specimen using a spark slicer. 3 mm diameter discs were then cut out from this slice using the spark machine. The surface of the discs was cleaned and their thickness reduced to ≈ 0.7 mm by chemical polishing in NaOH solution. The discs were then put in a P.T.F.E. holder and electrolytically polished in the solution given in Table 2.2. The temperature of the electrolyte was kept at $0^{o}C$ and the current was finely controlled with a micro-switch. The use of an optical bench, with a source of light behind the beaker containing the polishing solution and the P.T.F.E. holder, enabled the exact moment of perforation to be judged. Polishing was stopped immediately and the specimen washed in hot phosphoric acid and boiling distilled water and then squirted with methanol. Good polish resulted, though some difficulty was encountered during polishing due to the formation of bubbles on the surface of the specimen.

A polishing method similar to that for thin sheet aluminium was used for Al - 4% Cu. The electrolyte was kept cool by arranging the beaker above a dewar of liquid nitrogen. After the polish the specimen

was washed in boiling water, rinsed in cold ethanol and dried by blowing cold air over it.

Chemical polishing, with the solution given in the table, was found to be the most effective method of thinning Al - Mg. A 3 mm x 3 mm piece of the specimen was cut and dropped in the hot polishing solution. Vigorous reaction took place and the specimen polished and reduced in size in 5 to 10 min. A rounding off at all the corners of the sample was the sign that it had adequately polished. It was picked out by dipping a 2 mm bore glass tube over it and dropped into a watch glass containing methyl alcohol. The specimen was then floated directly onto an electron microscope grid for examination. This polishing method gives very good results for Al - Mg though it was not found to be very satisfactory for aluminium. One has also to be a little careful at the end of the polishing reaction as the polishing rate is very high and the specimen can totally disappear if one is not quick.

The appropriately thinned specimens were examined in the JEM7, or the JEM200 electron microscopes operating at 100 kV and 200 kV respectively. The 100 kV electron microscope is now a conventional instrument though the 200 kV electron microscope is not in wide use. JEM200 is an extended version of JEM7 in its constructional details. Apart from the standard voltage of 200 kV it can also operate at stabilized voltages of 100 kV and 150 kV, and at unstabilized stages of 125 kV, 175 kV and 220 kV.

High voltage electron microscopy has been reviewed by Cosslett (1967) and Hakin and Sharp (1968). The main advantage offered by the operation at a higher voltage is the greater transmission. To a first approximation, the transmission increases directly as v^2, where v is the velocity of the electrons. Thus the transmission in a 200 kV microscope is expected to be 1.6 times as high as that in a 100 kV microscope. The transmission in practice is however found to be even

higher. Perfectly good micrographs have been obtained in the 200 kV microscope for aluminium foils of thickness as high as 1.3 μm. Another consequence of the increased voltage is an improvement in the quality of the images. This is due to the reduction in chromatic and spherical aberrations resulting from an increase in the voltage. Also, the extinction distance, which goes up directly with v, is 1.27 times greater at 200 kV than at 100 kV. The foils are thus effectively thinner at the higher voltage and hence the contrast from the defects is better (Humble 1969). Another point in favour of the 200 kV microscope is the appreciably reduced contamination of the specimen (contamination rate goes down sharply with an increase in the voltage).

The 200 kV electron microscope was also used for producing and examining the radiation damage in aluminium due to the high energy electrons. Details of these experiments are however discussed in the relevant chapter.

During the observation of specimens in the two microscopes the contamination rate was kept to a minimum by the use of a liquid nitrogen cooled anticontamination device. All the specimens were examined using the bright field images. The rise in the temperature of the specimen due to beam heating is difficult to estimate, but because of its good thermal conductivity the temperature of the specimen is not expected to be very much higher than room temperature. Quite low beam currents, < 50 μamp (the leakage current read on the panel, the actual electron beam current being nearly two orders of magnitude lower), with a condenser aperture size of 200 μm, were used during examination.

The two electron microscopes are fitted with a goniometer stage for tilting the specimen. The tilting axis of the specimen holder can be rotated to any position around 360° and the holder can then be tilted up to ± 30° about this axis. This large tilt enabled the specimen to be observed in a large number of different orientations and reflections.

With a suitable foil normal it was possible to use nearly all the orientations within two adjacent stereographic triangles. For example, with a foil normal near [1$\bar{1}$2] all the orientations within the two triangles defined by [001][1$\bar{1}$1][101] and [001][1$\bar{1}$1][0$\bar{1}$1] are within reach.

In the JEM7 the micrographs were usually taken at a magnification of x22,000, which corresponds to its selected area diffraction setting. In the JEM200 some of the micrographs were taken at its S.A.D. setting, i.e. at a magnification of x15,000, and some at x22,000 for direct comparison with the micrographs taken on JEM7. The average thickness of the areas examined was about 3,000 Å in the 100 kV microscope and 5,000 Å in the 200 kV, though foils were found to be still transparent for thicknesses of 7,000 Å in the former and over 1 μm in the latter.

The measurement of thickness of the foils examined was also made in some cases. Rough estimation of thickness was sometimes obtained in terms of the extinction distance by simply counting the number of fringes from the edge under w = 0 conditions. A more accurate measure of thickness was obtained by using stereo-microscopy (Nankivell 1962). A stereo-pair of the same area was taken with a tilt 2θ (of the order of 5 to 10°) between them. These were then examined in a Hilger and Watts stereoscope designed for thickness measurement. The parallax p between the two surfaces was removed by adjusting a floating point of light to coincide with objects on the two surfaces. The value of p was then directly read off a micrometer, and, knowing the magnification M, the thickness t was calculated as :

$$t = p/2M \sin \theta$$

This is a simple method to use and can also be employed to find the depth of a particular defect in the foil.

Another method for finding the foil thickness used the projected length of an extended defect intersecting both the top and bottom

surfaces. This becomes very simple in the case when the extended defect is straight and lies along a known direction, such as a dislocation helix or a row of loops. When such a defect was not conveniently available, this method was used by finding the projected length, and the orientation, of the line joining the points where a dislocation intersected the two surfaces. The thickness t can then be calculated from the projected length p of the defect, in a particular beam direction, by :

$$t = p \operatorname{cosec} \phi \cos \theta$$

where θ and ϕ are the angles which the direction along which the defect lies makes with the foil normal and the beam direction respectively.

CHAPTER THREE

THE DECORATION OF SUBMICROSCOPIC DEFECTS

3.1. Introduction

Quenched aluminium has been extensively investigated using transmission electron microscopy and three different types of vacancy clustered defects have been recognized - prismatic dislocation loops (Hirsch et al 1958), faulted loops (Yoshida et al 1962) and voids (Kiritani and Yoshida 1963). These defects were observed in specimens quenched from temperatures between 550°C and 650°C to room temperature or thereabouts. Such specimens when deformed at the temperature of the quenching bath show an increase in the density of the defects (Kiritani et al 1966a) but no change in the defect distribution or character. There are no reports on the electron microscope observations of aluminium quenched, with a high quenching rate, to temperatures very much below 20°C, and then deformed at this temperature. The investigation of precisely these conditions in aluminium, i.e. fast quenches to temperatures ranging down to -195°C and subsequent deformation at these temperatures, is now going to be described. The observation of defects for various quenching conditions, in specimens deformed a fixed, appropriate, amount after the quench, forms the subject of this chapter, while the effect of the deformation treatment on these defects is discussed in detail in the following chapter.

The two interesting configurations of defects observed under the conditions described above are rows of dislocation loops along <110> and narrow faulted dipoles with their axis along the same direction. Previous observations of these defects in other metals have been described in detail in Chapter 1 and will not be repeated here. It will be shown in

this chapter that these two defects are made observable in aluminium due to the decoration, by quenched-in vacancies, of submicroscopic defects produced during deformation.

The difficulty in investigating, and in describing, the appropriate conditions of decoration arises from the fact that none of these conditions is independent of the other. The determination of only one of these conditions unambiguously meant doing a set of experiments. In the following, the effect of these conditions is described one by one, and while the defect character and density is described for the variation of each condition, it is assumed that all the others are set to their optimum value and remain the same for any variation of the particular parameter being investigated.

The general procedure found most effective for the observation of rows of loops and faulted dipoles, and referred to subsequently as the 'standard' treatment, was :

(i) A quench from air from a temperature of between 500 and 650^{o}C into brine at 0^{o}C and then into liquid nitrogen;

(ii) Tensile deformation of the specimen at this temperature (-195^{o}C); and then

(iii) An up-quench into iso-pentane bath at -90^{o}C and a gradual ageing-up to room temperature.

As the details of the deformation treatment are not discussed until the next chapter, it should be assumed, unless otherwise mentioned, that in each case the specimen was given a tensile strain of 4% at the temperature of the quenching bath. The optimum conditions for decoration were established by maximizing the density of the rows of loops along <110>. This is because the rows of loops are more readily observable in comparison with the faulted dipoles, as they are longer, are in a higher density, and are less sensitive to the amount of deformation. Even though some sections of this chapter are described entirely in terms of the rows of loops,

the statements made are nonetheless equally applicable to the faulted <110> dipoles (i.e. dipoles lying along <110> directions).

The exact quenching conditions investigated, and the effect these have on the density of the rows of loops and faulted dipoles, are described in Section 3.2., while in the following section it is shown that these defects are not observed in unquenched specimens given the same deformation treatment. Section 3.4. analyses the nature of the defects, i.e. the Burgers vector of the loops in the rows and of the faulted dipoles, and also examines the way in which computed images may be used to determine the dipole widths. The formation of the rows of loops is discussed in Section 3.5. in the context of previously reported mechanisms while Section 3.6. shows that the conditions of quenching where the rows of loops and the faulted dipoles are observed are indeed those where a decoration phenomenon might be expected.

3.2. The Effect of Quenching Conditions

3.2.1. Specimen purity. The three different purities of aluminium quoted in Chapter 2 were given varying, but identical, quenching treatments. The density and size of the random dislocation loops showed the expected behaviour, their number decreasing and the size increasing with increasing purity. This effect is consistent with that observed by other workers (Yoshida et al 1963; Segall and Clarebrough 1964; Siegel 1966; Davis and Hirth 1966b; Kiritani et al 1969) in aluminium and gold, and shows that the type of impurities present are active sites for the heterogeneous nucleation of loops. While the number of loops increases in the impure material due to the increased number of nuclei, the number of vacancies going to each loop, and hence the size of the loop, decreases. The distribution of the random loops also changed with purity, becoming less uniform with increasing purity. This fact has been noted by previous authors as well (Embury et al 1962; Kiritani 1964; Meshii et al 1966). This non-uniformity of density in high purity aluminium, where loops

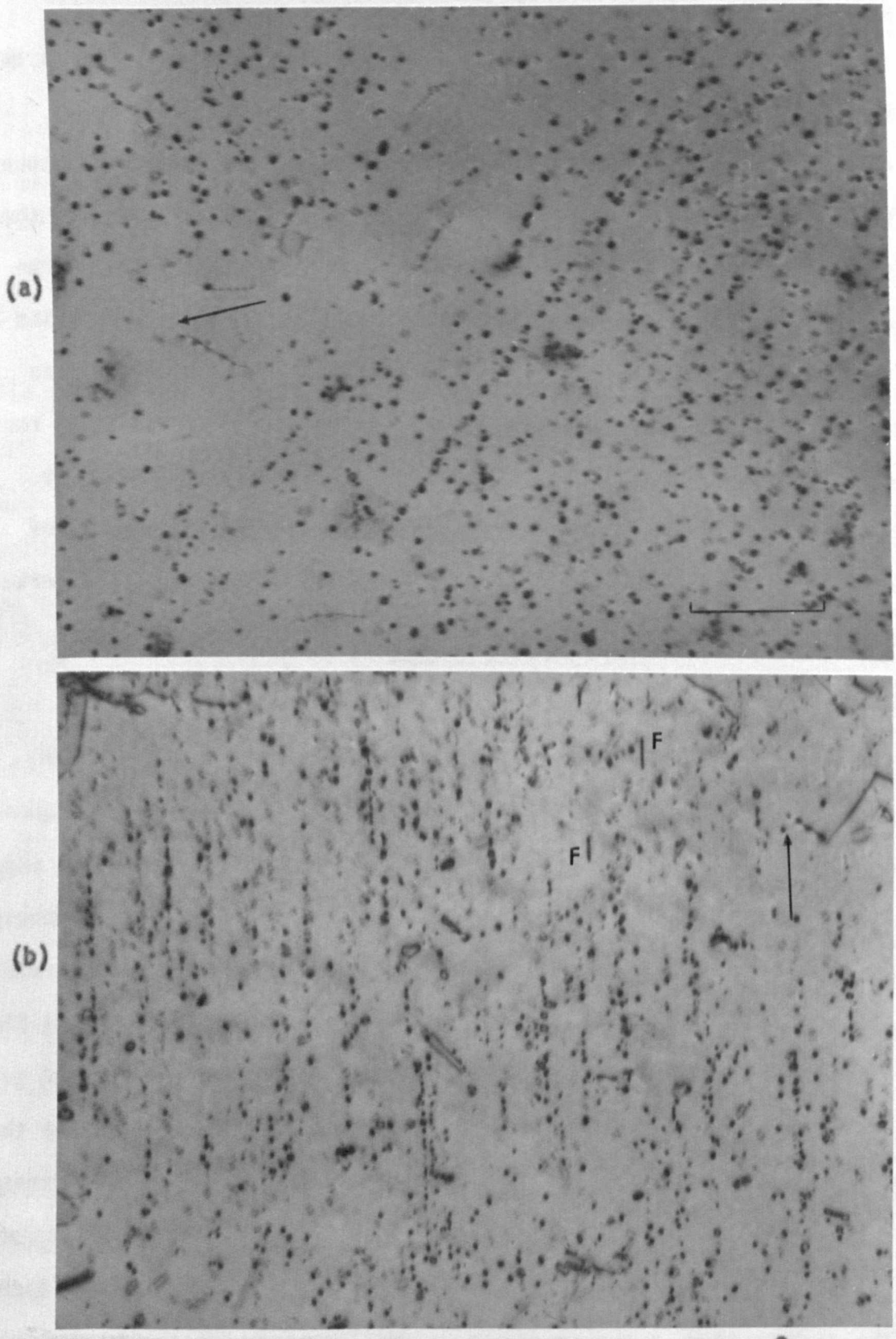

Figure 3.1. Rows of loops in specimens quenched from 550°C.

(a) Al 4N. Beam direction : [103]; $\underline{g}$: 020; 100 kV.

(b) Al 6N. Also showing faulted dipoles at F.
Foil normal : near [105]; Beam direction : [001];
$\underline{g}$: 020; 100 kV.

tended to exist in form of colonies, was particularly marked in case of deformed specimens.

The density of the rows of loops, as compared to that of random loops, showed an opposite purity dependence. The number of rows increased sharply with increasing purity. While the density of loops decreased by a factor of about 50 in going from Al 4N through Al 5N to Al 6N the mean density of rows increased approximately as 1:50:500. Thus the fraction of loops occurring in rows increased by more than four orders of magnitude as the purity was increased from 99.99% to 99.9999%. Though a very detailed examination of the lower purities was not made, the faulted dipoles were observed only in Al 6N. Table 3.1. gives the size of the observed loops, and the mean densities of random loops, and rows of loops, for different purities, while Figures 3.1(a) and (b) show rows of loops in Al 4N and Al 6N, respectively, quenched from 550°C and given the standard treatment. Both the micrographs illustrate areas of maximum row density and Figure 3.1(b) also shows narrow faulted dipoles at F. The loop density is not representative in case of Figure 3.1(a), as rows of loops in Al 4N are observed only in areas with loop density well below the average. Similar observation, i.e. the occurrence of rows of loops in areas of low defect density, was made in silver by Smallman et al (1959-60).

3.2.2. Quenching temperature. The range of quenching temperatures investigated was from 500°C to the melting point (660°C). Increase in the quenching temperature resulted in an increase in the density of the random loops. The density of the rows of loops on the other hand declined very markedly with increasing temperature. The optimum quenching temperature for a high density of rows of loops depends very sensitively on other quenching conditions. For a fast quench to liquid nitrogen in an air atmosphere, and a deformation of about 4%, maximum density of the rows was observed for a quench from 550°C. Figures 3.2(a) and 3.2(b) show

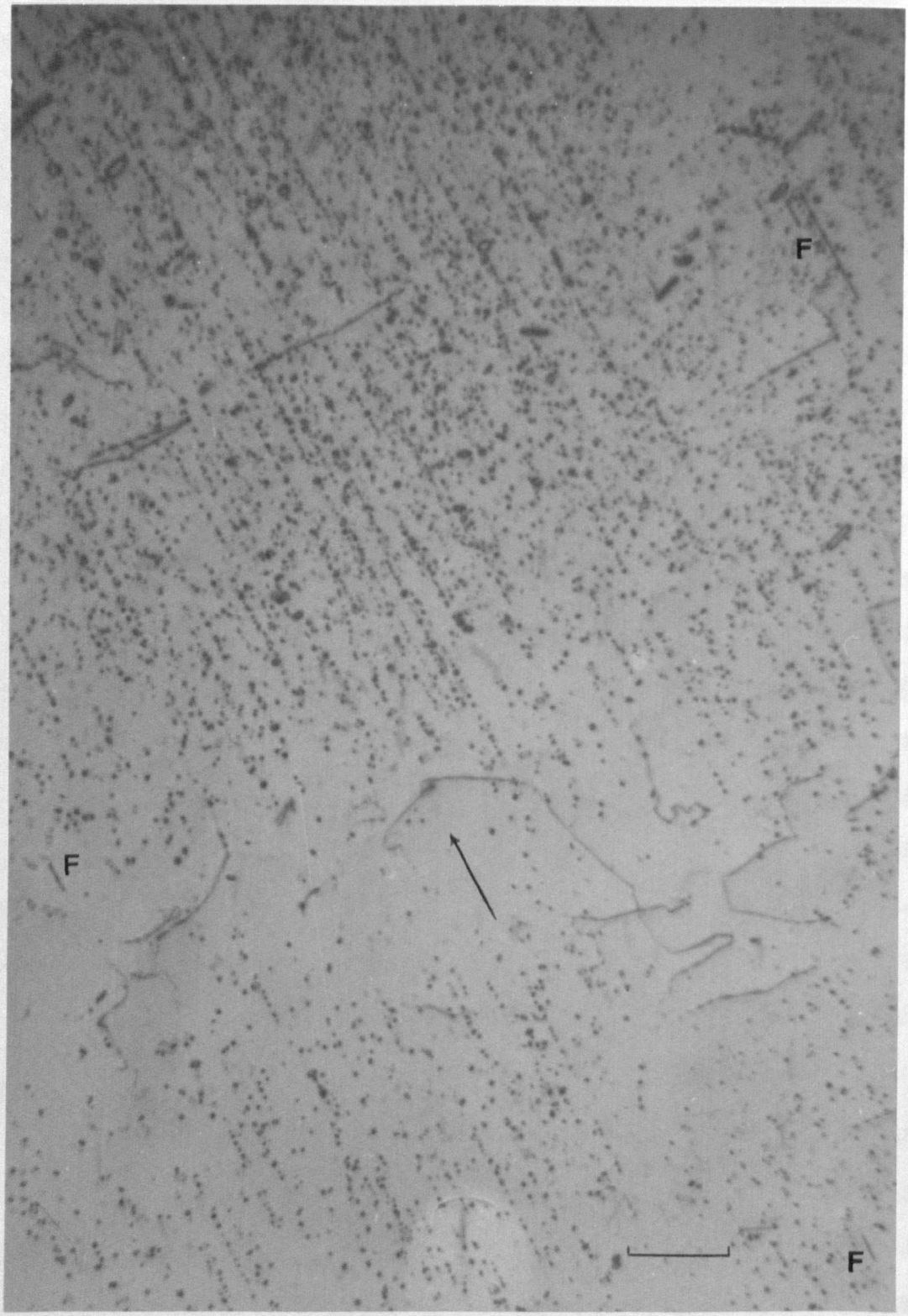

Figure 3.3. A high row density area in a specimen quenched from 550°C. The direction of the rows and the faulted dipoles F is along $[\bar{1}01]$, inclined at about 27° to the (103) foil plane.

Beam direction : [001]; $\underline{g}$: 200; 100 kV.

(a)

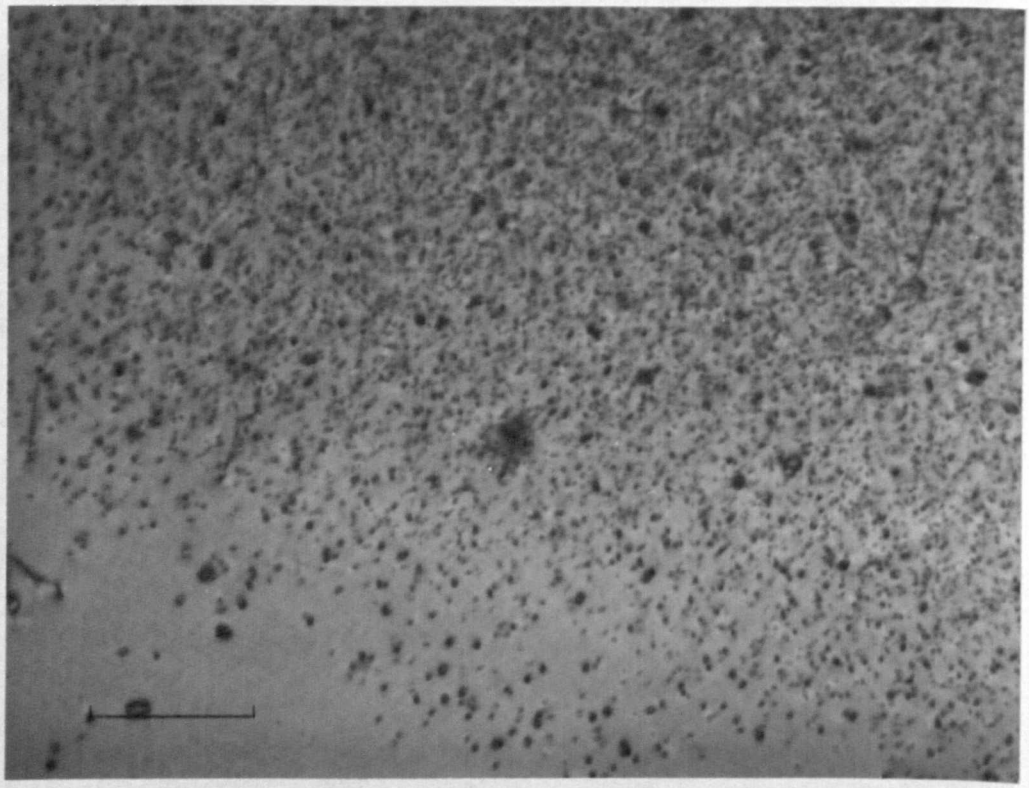

(b)

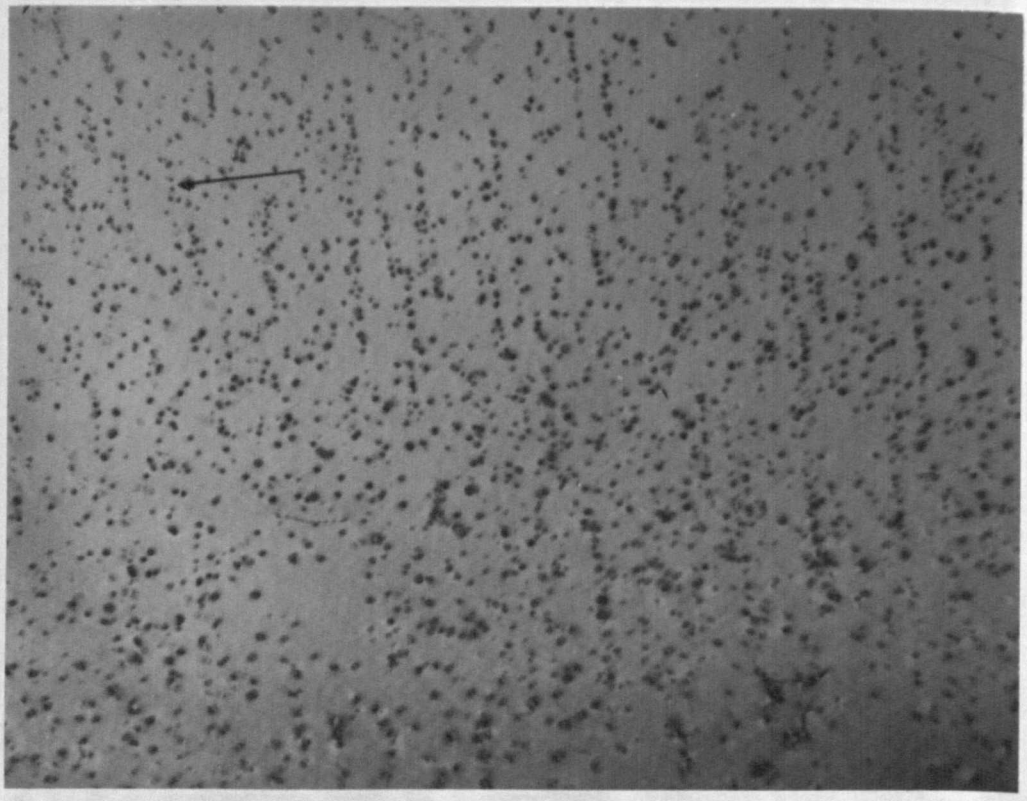

Figure 3.2. Representative areas from Al 6N quenched (a) from 630°C, and (b) from 550°C.

(a) Beam direction : [103]; $\underline{g}$: 020; 150 kV.

(b) Foil normal : near [102]; Beam direction : [001]; $\underline{g}$: 020; 100 kV.

representative areas of Al 6N specimens quenched from 630°C and 550°C respectively and given the standard treatment described earlier. The loops in the specimen quenched from the lower temperature are larger in size, lower in density, and have a tendency to be aligned in rows. The mean densities of the random loops and the rows of loops in Al 6N quenched from different temperatures are given in Table 3.1. As will be shown in the following sub-section, the optimum value of the quenching temperature was higher when the quenching atmosphere was hydrogen.

It was found that the density of the rows of loops was high only in a narrow range of temperature. While a high density of loops was observed in standard quenches from temperatures above 600°C, very few of these were aligned in rows. For temperatures below 550°C the number of loops went down sharply and these occurred in small scattered colonies, but few in rows. At the appropriate quenching temperature, where a high density of rows of loops was observed, a large fraction of the loops, sometimes as much as a half, occurred in the form of rows. Such an area, from a specimen quenched from 550°C and given the standard quenching and deformation treatment is shown in Figure 3.3. The figure also shows a number of faulted dipoles, along [$\bar{1}$01], at F.

3.2.3. Quenching atmosphere. Four different atmospheres were used during quenching - hydrogen, forming gas, nitrogen, and air. There was no appreciable difference in the observed defect characteristics for specimens quenched in hydrogen or forming gas, and similarly for those quenched in nitrogen or air. The presence of hydrogen during quenches from high temperatures markedly increases the row density. Specimens were quenched both in hydrogen and in air atmospheres from temperatures above 600°C to liquid nitrogen through cold brine. While the specimens quenched from air contained only a few or no rows of loops, the specimens quenched in hydrogen consistently gave an appreciable density of the

Table 3.1. Density and Size of the Random Loops, and the Density of the Rows of Loops, in Aℓ Specimens Fast Quenched to -195°C and then Deformed 4%

	Specimen Purity (Quench Temperature 550°C)			Quenching Temperature (Aℓ 6N specimens)			
				Air atmosphere		Hydrogen atmosphere	
	Aℓ 4N	Aℓ 5N	Aℓ 6N	630°C	520°C	630°C	550°C
Size of the loops, Å	100	200	200	100	200	100	200
Density of the (random) loops, cm^{-3}	5×10^{14}	5×10^{13}	10^{13}	5×10^{14}	10^{12}	5×10^{13}	5×10^{12}
Density of the rows of loops, cm^{-3}	2×10^{7}	10^{9}	10^{10}	-	10^{8}	10^{9}	5×10^{8}

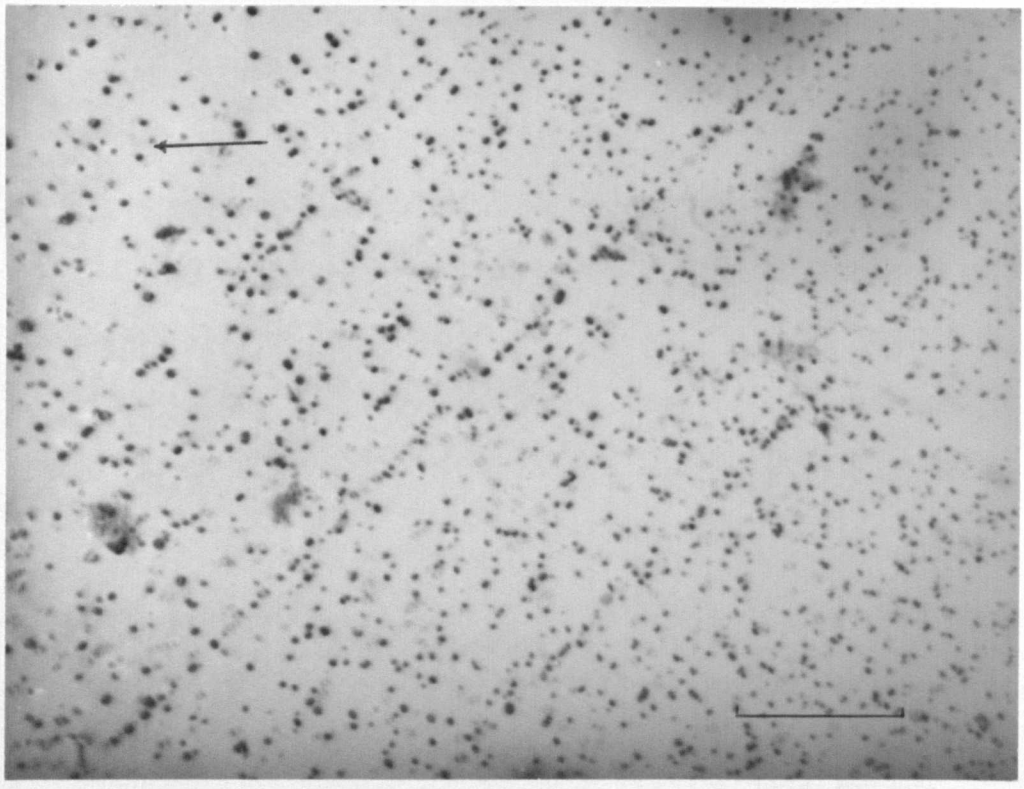

Figure 3.4. An area from Aℓ 6N quenched in a forming gas atmosphere from a temperature of 630°C.

Beam direction : [001]; $\underline{g}$: 020; 100 kV.

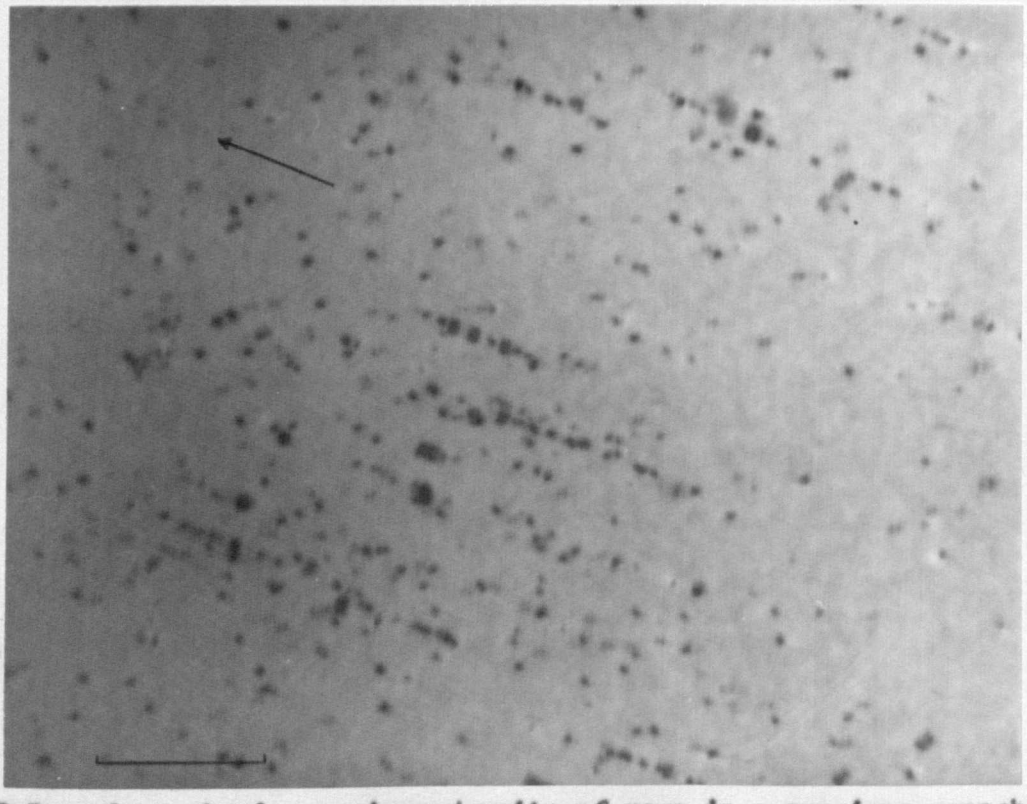

Figure 3.5. Area showing maximum density of rows in a specimen quenched from 550°C to methanol at -90°C.

Beam direction : [001]; $\underline{g}$: 020; 100 kV.

rows. Figure 3.4. shows the rows of loops in an Al 6N specimen fast quenched from 630°C to liquid nitrogen in a forming gas atmosphere, deformed 4% at -195°C, and given the standard ageing treatment. A specimen quenched similarly from 630°C, but in air, contains virtually no rows, as can be seen from Figure 3.2(a). However, for a quench from 550°C in hydrogen the density of the random loops, and that of the rows, is much lower. The latter result is in contrast to that for an air quench from the same temperature. The observed effect of hydrogen atmosphere on the loop and the row densities is given in Table 3.1.

3.2.4. Quenching speed. The different quenching media used, and their quenching speeds, have been given in Table 2.1. For a quench from 600°C, brine at 0°C gives the fastest quench rate of $\approx 5 \times 10^4$ °C sec^{-1}, while a direct quench into liquid nitrogen, with a quench rate of ≈ 750°C sec^{-1}, is the slowest. The quenching speed also changes when a specimen is quenched to the same medium, but from a different temperature or to a different temperature. The effect of quenching speed on the dislocation loops was predictable, i.e. their size increased and the density decreased for slower quenches. This could be partly due to the loss of vacancies during quenching and partly due to an increase in the density of voids which nucleate earlier than the loops (Kiritani et al 1966b). The formation of the rows of loops was not affected by the quenching speed in any direct way. The effect of using a more or less efficient quenching medium was similar to that obtained by raising or lowering the quench temperature. That is, a quench in a slower medium was analogous to a quench from a lower temperature. This would of course be true if no nucleation occurs during the quenching process. Al 6N specimens fast quenched from 550°C into liquid nitrogen through brine have been illustrated in Figures 3.1(b), 3.2(b) and 3.3. Figure 3.5 shows a high row density area from an Al 6N specimen quenched from 550°C to methanol at -90°C and given the usual deformation and ageing treatment.

Comparison with previous figures is not straightforward as here the specimen was deformed at a comparatively higher temperature (-90°C).

3.2.5. Specimen thickness. Specimens of thicknesses varying between 75 μm and 200 μm were given similar quenching treatment. No difference in the density of loops, or of rows, was observed for various thicknesses. Two likely reasons for any effect are the change in the thermal strain, and in the quenching rate for specimens of different thicknesses. The former is expected to be very small in any case for this thin specimens, while for the latter it has been shown (Lorimer 1967) that the quenching rate is effectively the same for all specimens of thickness below 200 μm.

3.2.6. Ageing temperature. A systematic investigation of the ageing temperature was found to be difficult. The ageing procedure used, described in detail in Chapter 2, consisted of gradually warming up the specimen to the room temperature from that of the quenching bath. Constant temperature ageing was not used as it would strictly be unambiguous only if the specimen was aged at the temperature of the quenching bath. Otherwise there is an uncertainty as to what happens during the interval when the temperature of the specimen is changed from that of the quenching bath to that of the ageing bath. If different ageing temperatures T_a are investigated, by quenching each time to this temperature, and, what is more important, deforming at T_a, it is difficult to separate the effects due to ageing at T_a, deformation at this temperature, and, to a lesser degree, the change in vacancy supersaturation. Furthermore, if the ageing is incomplete at the fixed ageing temperature T_a, it is likely to be affected by the change to room temperature where electron microscope observation is to be made.

Keeping the above considerations in mind, the specimens were quenched down, through cold brine, to -195°C and deformed 4% at this

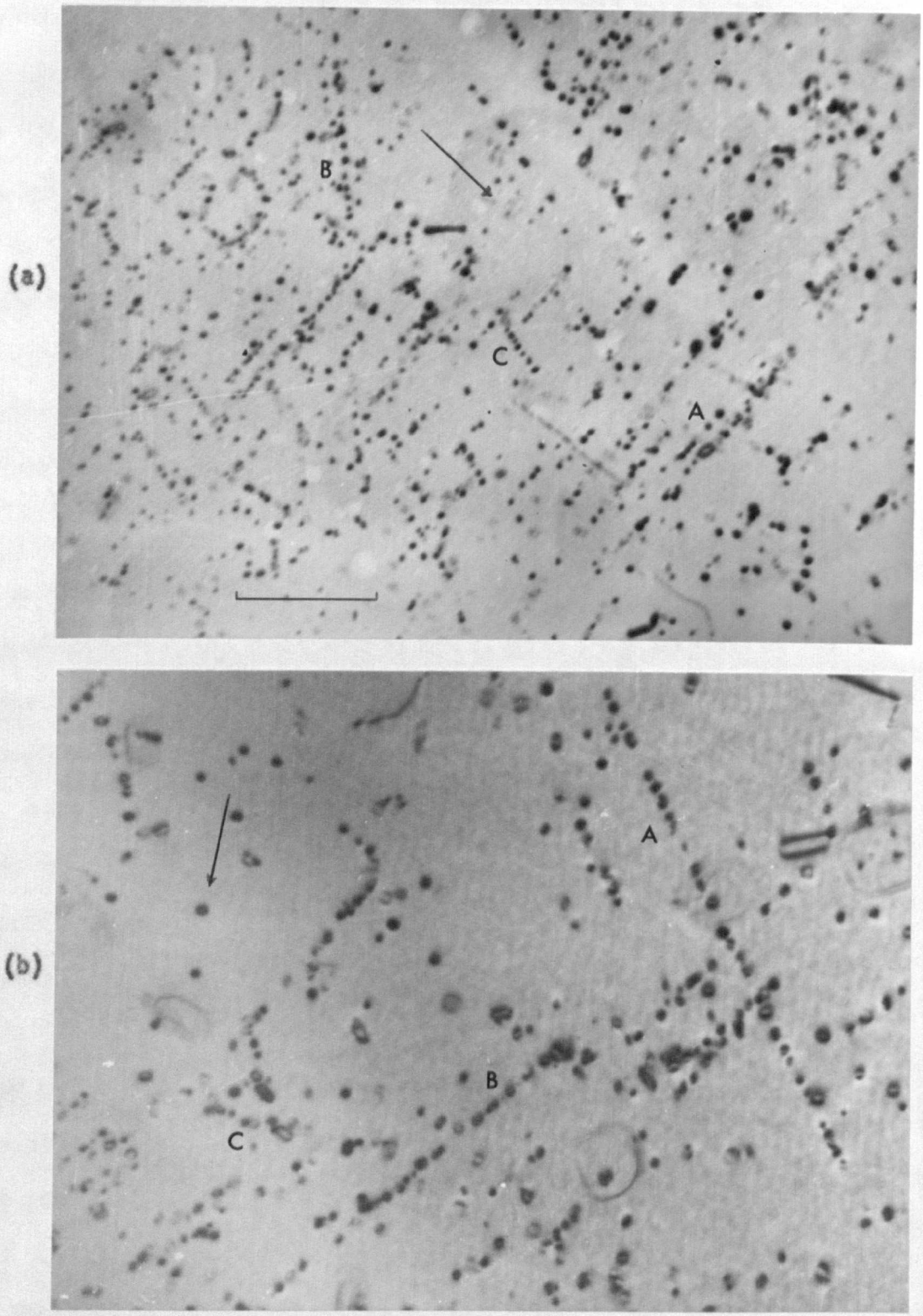

Figure 3.6. A specimen fast quenched, in a forming gas atmosphere, to liquid nitrogen and then cut in two halves. Figure (a) shows an area from the half aged up from -90°C, and (b) an area in the half aged at 0°C. Note the rows along three different <110> directions at A, B and C.

(a) Beam direction : near [105]; $\underline{g}$ = 020 ; 100 kV.

(b) Beam direction : [101] ; $\underline{g}$ = 020 ; 100 kV.

temperature. The ageing processes then investigated consisted of up-quenching from -195°C to -90°C, -40°C or 0°C and then gradually ageing up to room temperature. It was recognized that some ageing, though very little due to the low temperature, could take place during the up-quench. As far as the density of rows of loops is concerned, the results proved that a more detailed enquiry into the ageing treatment was not required. No major difference in the density of the rows was observed for specimens given identical treatment but aged up from different temperatures. The effect of the ageing treatment was evident only in the size of the dislocation loops. For the specimens aged up from higher temperatures the loops were larger in diameter. Thus the rows were composed of a smaller number of loops of larger size. The overall density of the random loops was found to be smaller as well. Figure 3.6. illustrates the above mentioned facts regarding the effect of ageing temperature on the rows of loops. An Al 6N specimen was quenched, in a forming gas atmosphere, from 550°C to liquid nitrogen via brine at 0°C. It was not deliberately deformed, but was cut in two halves while at -195°C. One half was transferred to an iso-pentane bath at -90°C and slowly aged up from there, while the other half was transferred back to brine at 0°C. Figure 3.6(a) shows an area from the specimen given the low temperature age, while Figure 3.6(b) is from the specimen aged up from 0°C. Rows along different <110> directions at A, B and C are characteristic of those formed due to accidental deformation.

3.3. Experiments on Unquenched Crystals

The last section has dealt extensively with the observation of rows of loops along <110>. This description has tended to underemphasize the occurrence of faulted dipoles with their axis also along this direction. Though the density of these dipoles ($\sim 10^7$ cm^{-3}) is three orders of magnitude lower than that of the rows of loops it is not insignificant. Examples of these dipoles have been shown in Figures 3.1(b) and 3.3.

The observation of narrow faulted dipoles in a number of metals and alloys of low stacking-fault energy, deformed in simple tension, has been described in Chapter 1. These dipoles were very narrow, giving extremely weak images. There are however no reports of similar dipoles in deformed aluminium. In view of the present observation of quite wide faulted dipoles, giving surprisingly strong images, in quenched and deformed aluminium, a search was made for these dipoles in unquenched, but deformed, specimens.

Two different crystals were studied. A bulk single crystal of At 4N, with a tensile axis 4° from 111 and 3° inside the 001-111 symmetry axis, was pulled 4-5% in tension at $-195^{\circ}C$. This deformation temperature was chosen because it was found to be the most effective temperature for a 4% strain for the production of faulted dipoles in quenched and deformed specimens. A large grained foil of At 6N, with the largest grain having about the same orientation as that of the bulk crystal, was also given similar deformation treatment. Thinned slip plane slices from the bulk crystal, and thinned specimens from the foil were observed in the 200 kV electron microscope. As the dipoles were expected to be too narrow to be visible on the screen, a large number of pictures were taken in and around areas showing evidence of deformation in form of <211> dipoles and dislocations. The reflections used for observation were 200 type and the deviation parameter $w = s\xi_g = 1.0$. Careful examination of the plates showed no faulted dipoles.

The optimum conditions for the observation of narrow defects in aluminium have subsequently been found to be a small w (Section 3.4.4.), and electron microscope examination at a voltage $\leq$ 150 kV to avoid any annealing due to radiation damage (Chapter 6). However the failure to observe faulted dipoles in the above experiments is still significant and not entirely unexpected. The highest stacking-fault energy material

in which faulted dipoles have been seen is nickel (Haussermann and Wilkens 1966) and these images were very faint. As aluminium has a higher γ/Gb value ($\approx 17.5 \times 10^{-3}$ as compared to 11.6×10^{-3} for nickel), the dipoles in aluminium are expected to be narrower than those in nickel ($\approx$ 40 Å) and hence it is not surprising that they are not observed. The observation of faulted dipoles, almost 150 Å wide, in quenched and deformed aluminium is a clear indication of the fact that these were made visible by decoration of the sub-microscopic dipoles formed during deformation.

3.4. Detailed Analysis of the Observed Defects

3.4.1. The determination of Burgers vector. The determination of Burgers vector of dislocations and dislocation loops, using contrast experiments, is now a standard technique (see, e.g., Hirsch *et al* 1965a). The Burgers vector has been defined in a number of equivalent ways (see, e.g., de Wit 1960), which has resulted in some confusion as, depending on the convention used, the sense of the Burgers vector can be different by 180°. Similarly, the positive sense of the dislocation line in a loop has also been defined in two different and opposite ways. The conventions which are to be used in this dissertation for these two characteristic directions will be clearly stated in this sub-section. The method of determining the Burgers vector of the loops, and its sense, will also be briefly described.

The FS/RH (perfect crystal) convention, originally described by Frank (1951) and elaborated by Bilby *et al* (1955), will be used throughout to define the Burgers vector. A closed Burgers circuit is drawn round the dislocation related by a right-hand (RH) rule to the positive sense of the dislocation (i.e. a clockwise circuit looking down the positive direction of the dislocation), which starts at S and finishes at F. The Burgers vector is then the closure failure FS in the

corresponding circuit drawn in the perfect reference crystal. This convention has been used by de Wit (1960), Friedel (1964a), Hirsch et al (1965a), and Hirth and Lothe (1968a), while an opposite convention is used by Read Jr. (1953a), Weertman and Weertman (1964a), and Nabarro (1967).

In the determination of Burgers vector $\underline{b}$ of loops and dipoles the visibility criteria used for observation in various reflections $\underline{g}$ were as follows (Silcock and Tunstall 1964; Hirsch et al 1965a; Loretto et al 1966) :

Loops and dipoles in contrast for $\underline{g} \cdot \underline{b} = \pm 1, + \frac{2}{3}, \pm \frac{4}{3}, \pm 2$;

Loops and dipoles out of contrast for $\underline{g} \cdot \underline{b} = 0, \pm \frac{1}{3}, - \frac{2}{3}$.

The criterion of $\underline{g} \cdot \underline{b} = + \frac{2}{3}$ for visibility and $\underline{g} \cdot \underline{b} = - \frac{2}{3}$ for invisibility of the bounding dislocation in a Frank loop is very useful for establishing the faulted nature of small loops which do not show stacking-fault contrast. In such a determination all the eight possible <111> Burgers vectors should be considered, as [111] behaves differently than $[\bar{1}\bar{1}\bar{1}]$. This criterion must however be used with caution as it is applicable only for large values, ≥ 1.0, of the deviation parameter w (Silcock and Tunstall 1964). Even then the faulted loops and the faulted dipoles show a weak contrast, which will be evident from the $\underline{g} \cdot \underline{b} = - \frac{2}{3}$ pictures shown in subsequent figures. If one is not careful, this faint contrast from the faulted defects could be confused with the weak contrast resulting from unfaulted defects when they are observed in conditions where the image lies outside the defect. Another point to note is that the edge contrast condition, i.e. total invisibility of $\underline{g} \cdot \underline{b} = 0$ pictures when $m = \frac{1}{g} \underline{g} \cdot (\underline{b} \times \underline{u}) \leq 0.08$, $\underline{u}$ being a unit tangent vector to the dislocation line (Howie and Whelan 1962), perhaps requires reconsideration for Frank dislocations observed under $\underline{g} \cdot \underline{b} = \pm \frac{1}{3}$ conditions, for many

of the dipoles in these conditions showed a contrast for m < 0.08.

The sense of the Burgers vector was determined to establish the vacancy or interstitial nature of the loops in the rows and of the faulted dipoles. The positive sense of the dislocation line in a loop or a dipole was taken as anticlockwise when looking along the electron beam, i.e. when looking down on the micrographs as they are printed (emulsion side upwards). This convention is consistent with that used by Silcock and Tunstall (1964), Hirsch et al (1965a) and Loretto et al (1966), but opposite to that used by Howie and Whelan (1962) and Mazey et al (1962). Using the FS/RH convention for the Burgers vector it can then easily be shown that the Burgers vector of a vacancy loop makes an acute angle, and that of an interstitial loop an obtuse angle, with the upward drawn foil normal. The sense of the Burgers vector is determined uniquely for faulted loops due to reversal of their contrast in reflections of the type $\underline{g} = \pm 200$ (Tunstall 1969). For the unfaulted loops and dipoles, however, the sense of the Burgers vector is not resolved by the ordinary visibility criteria. The sense of the Burgers vector is then determined by noting the size of the image in $\pm \underline{g}$ conditions (see e.g. Hirsch et al 1965a). With the definition of anti-clockwise sense round the loop as positive, the image of the loop would lie inside the loop if $(\underline{g} \cdot \underline{b})\, s > 0$ and outside if $(\underline{g} \cdot \underline{b})\, s < 0$, s being the deviation from the exact Bragg position. This convention is again opposite to that used by Howie and Whelan (1962) and Mazey et al (1962). The nature of the loop is then determined by correlating the Burgers vector direction with the foil normal.

It is obvious from the above discussion that finding the sign of $\underline{b}$ requires the determination of the sense of $\underline{g}$, and a further decision about the vacancy or interstitial nature of the loops requires the determination of the sense of the foil normal, i.e. whether it is

[hkl] or [$\bar{h}\bar{k}\bar{l}$]. In the present experiments, the sense of the upward drawn normal was resolved from a nearby asymmetric diffraction pattern. (This step is of course unnecessary if the zero-tilt pattern in the electron microscope is a non-symmetrical one itself, e.g. [7$\bar{3}\bar{2}$] is different from [$\bar{7}$32]). The ambiguity of 180° inversion in $\underline{g}$ was then removed by using a method similar to that of Loretto et al (1966). The specimen was tilted from one diffraction pattern to another about the relevant $\underline{g}$, and the direction of the tilt was noted. The sense of $\underline{g}$ was then determined by correlating the direction of tilting with the emergence of various diffraction spots as one pattern changes to the other. The direction of tilting was found either from the actual tilt of the goniometer stage itself, or from the motion of the Kikuchi pattern on the screen (the apparent motion of the pattern being opposite in sense to the actual tilt). The above points are described in greater detail in Appendix A.

3.4.2. Nature of the loops in the rows and of <110> dipoles.

The general characteristics of the rows of loops and faulted dipoles were mostly determined from the quenching and deformation experiments on polycrystalline foils. The directions along which these two defects lay were ascertained from micrographs of the same defect taken in a number of widely separated electron beam directions. The projections of the dipoles or the rows of loops in at least three non-colinear beam directions were plotted on a Wulff net and thus the direction along which the defect lay was uniquely determined.

A typical row consisted of about 15 to 50 loops which were of equal size (diameter ≈ 200 Å in appropriately quenched and deformed specimens) and nearly equally spaced. The length of the rows varied between 0.5 and 2 μm, although rows as long as 4 μm have been observed (such as the rows A in Figure 4.2). However the lower and upper limits on the lengths of the rows may be superficial. If the rows are short it is difficult to recognize them as such, and if the

rows are too long their observed length would be limited by the foil thickness. The faulted dipoles observed were also of different lengths, the mean length being around 0.4 μm, and the longest observed dipole 1.1 μm long (shown at F_1 in Figure 3.11(a). These dipoles gave quite strong images and their approximate width, as estimated in the following sub-sections, was 100 to 150 Å. The mean densities of the rows of loops and the faulted dipoles in specimens given the optimum quenching and deformation treatment were nearly 10^{10} cm^{-3} and 10^7 cm^{-3} respectively.

The observed rows of loops and the faulted dipoles were found to lie strictly along <110> directions. In each grain the faulted dipoles lay along the same direction as the rows of loops. The rows of loops and the faulted dipoles lay along only one <110> direction in specimens appropriately deformed after the quench. However the rows observed in quenched specimens which were not deliberately deformed were often along several <110> directions. This was seen in Figure 3.6. and is again illustrated in Figure 3.7. which is also from a specimen not deliberately deformed but is assumed to have received accidental deformation. Rows of loops along four different <110> directions are observable at A, B, C and D.

Contrast experiments showed that nearly all the loops in the specimens were faulted, with an $\frac{a}{3}$ <111> Burgers vector. An important feature of the loops in the rows was that the majority of these, in a given row, had one or the other of the two $\frac{a}{3}$ <111> Burgers vectors perpendicular to the <110> direction of the row. The proportion of the loops having one of these two Burgers vectors varied and occasionally there were rows with the predominance of one Burgers vector. There was also a strong tendency for the neighbouring loops to have the same Burgers vector.

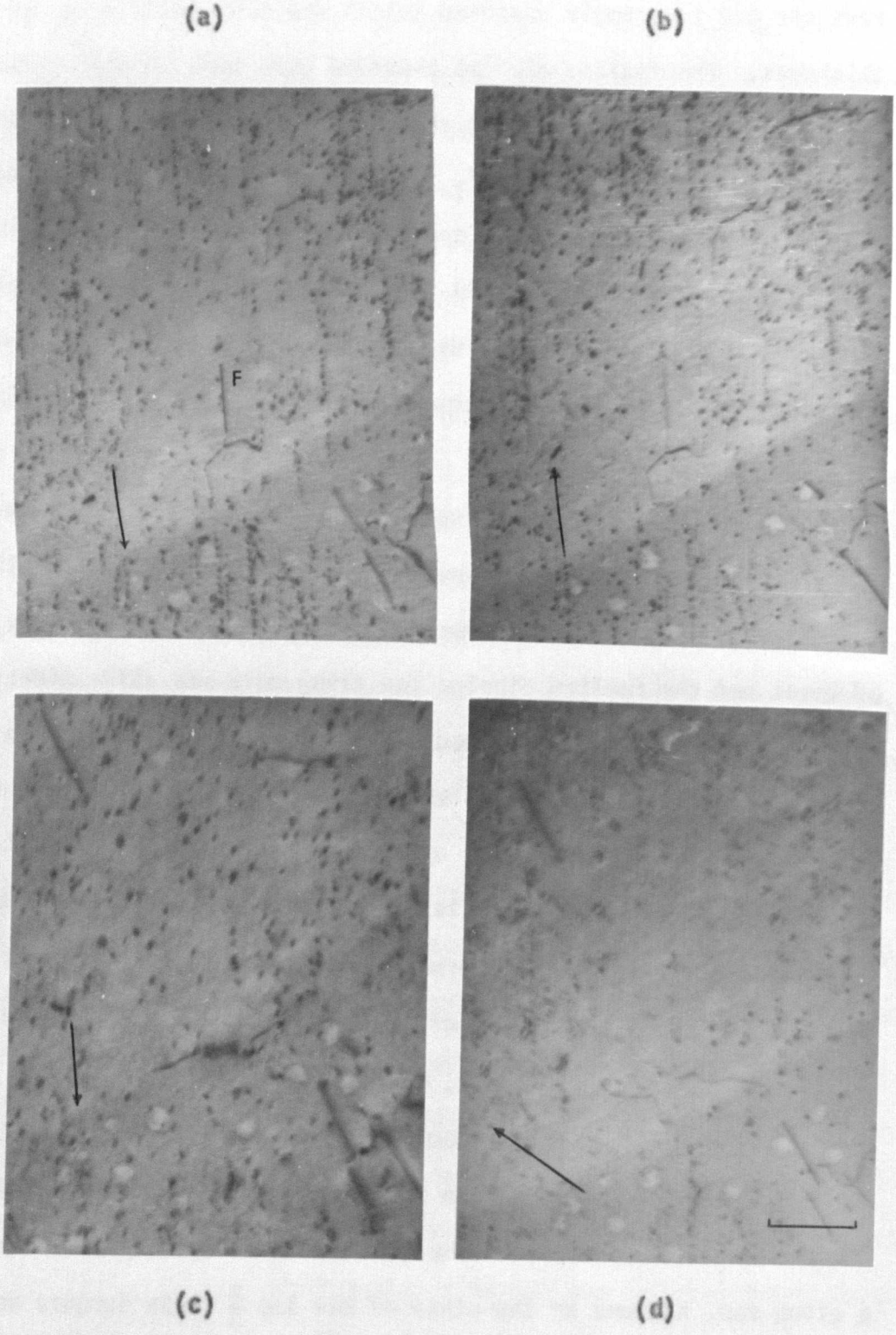

Figure 3.8. Burgers vector analysis for a faulted dipole F, and for loops in parallel rows, along [110] in Aℓ 6N given the standard quenching and deformation treatment. Micrographs show the same area in four different reflections, $\underline{g}$: (a) 200, (b) $\bar{2}00$, (c) 220, and (d) $\bar{2}0\bar{2}$.

Foil normal : $[1\bar{2}0]$; Beam direction : $[0\bar{1}0]$ in (a), (b) and (d), and $[1\bar{1}0]$ in (c); 100 kV.

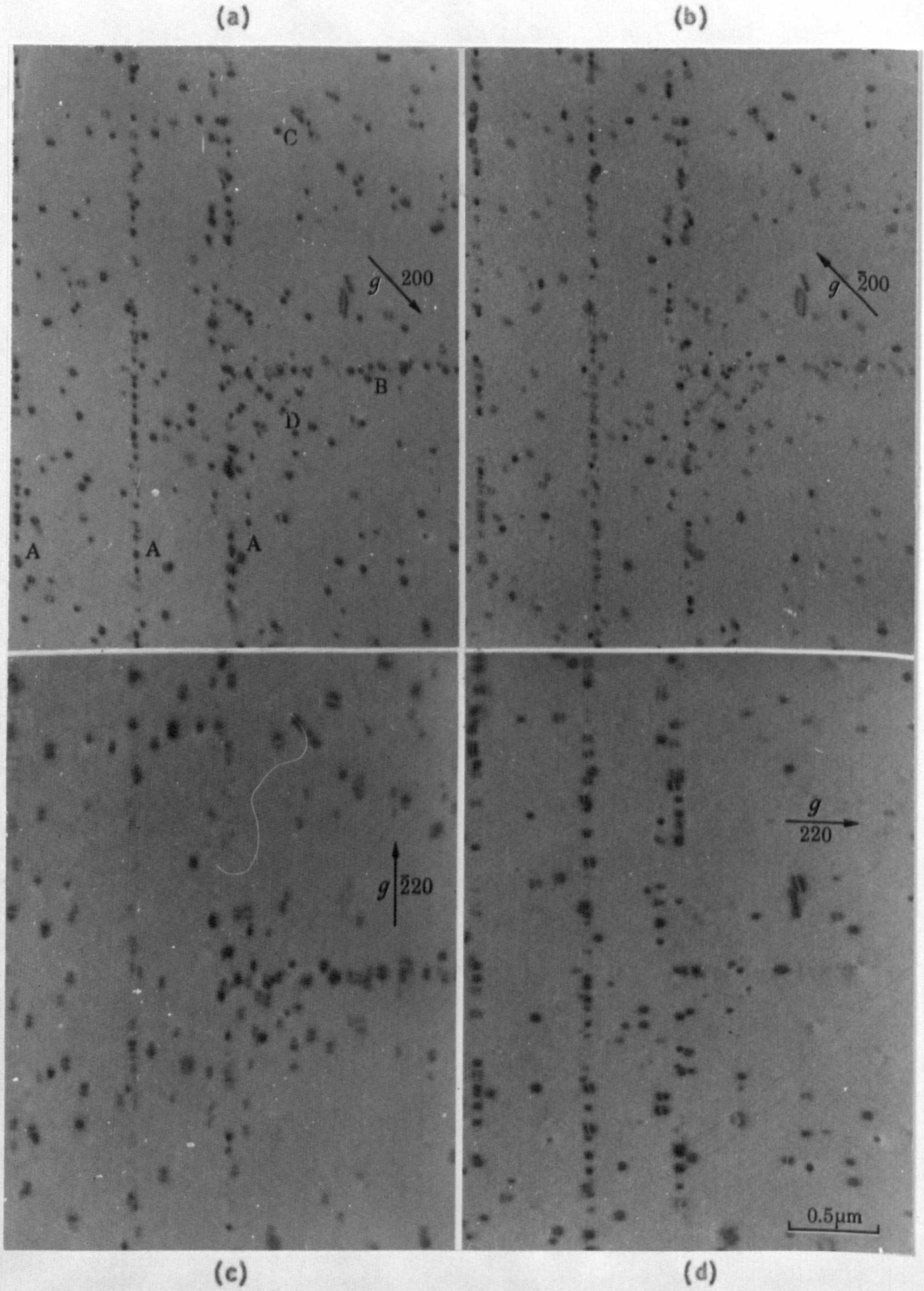

Figure 3.7. An Aℓ 6N specimen given the standard quenching treatment, with the difference that the specimen was not deliberately deformed after the quench. Rows of loops along four different <110> directions are seen at A, B, C and D. The micrographs, taken in four different reflections, illustrate the analysis of the Burgers vector of the loops.
Foil normal and beam direction : near [001]; 100 kV.

The above mentioned facts are illustrated in Figures 3.7 and 3.8. Figure 3.7 shows an area, in four different relfections, of Al 6N quenched from 550°C to liquid nitrogen through cold brine and given the standard ageing treatment. Figures 3.7(a) and (b) show the faulted nature of the dislocation loops. In 3.7(a), where $\underline{g} = 200$, the majority of the loops in the rows are in good contrast, the Burgers vector being such that $\underline{g} \cdot \underline{b} = +\frac{2}{3}$. A reversal of contrast is observed in 3.7(b), where $\underline{g} = \bar{2}00$ and $\underline{g} \cdot \underline{b} = -\frac{2}{3}$. In Figure 3.7(c) $\underline{g} = \bar{2}20$, and most of the loops in rows A, which are along $[\bar{1}10]$ are out of contrast. The loops in row B, which is parallel to [110] are seen to disappear in 3.7(d) where $\underline{g} = 220$. These last two figures show that most of the loops in a given row have either one or the other of the two $\frac{a}{3}$ <111> Burgers vectors perpendicular to the row direction.

Figures 3.8(a)-(d) show a similar, but complete, analysis of the Burgers vector of a faulted dipole F, and of the loops in parallel rows, in an Al 6N specimen given the standard quenching and deformation treatment. The dipole and the rows are along [110], at an angle of 71° to the $[1\bar{2}0]$ foil normal. The faulted nature of the [110] dipole and of the loops is illustrated by the reversal of contrast in Figures 3.8(a) and (b) which are in 200 and $\bar{2}00$ reflections. Invisibility of the faulted dipole, and of the loops in the rows, in 220 reflection in Figure 3.8(c) shows that their Burgers vector is perpendicular to [110]. The invisibility of the dipole, and of many of the loops in the rows, in Figure 3.8(d), in $\bar{2}0\bar{2}$ reflection, determines their Burgers vector as $\frac{a}{3}[1\bar{1}\bar{1}]$. The loops in the rows that are in contrast in this reflection have $\frac{a}{3}[1\bar{1}1]$ Burgers vector. From the fact that these Burgers vectors make an acute angle with the $[1\bar{2}0]$ foil normal, it can be concluded that the dipole and the loops are of vacancy type. An important point that emerged from the analysis of a large number of faulted dipoles was

that all the dipoles which lay along the same <110> direction had only one, and the same, Burgers vector out of the two that are perpendicular to the dipole axis.

3.4.3. Estimation of the dipole width. In the absence of detailed contrast calculations the width of the narrow dipoles can be estimated by two methods. Either the image width can be measured directly from the micrographs (or from their microdensitometer traces), or the strength of contrast of the dipole image can be noted in comparison with that from dislocations. The approximate dipole width can then be inferred from either or both.

The first method was made more difficult by the fact that in most cases the dipole image was single. Direct image width measurements were made in both the cases when the image was single and when it was resolvable into two parallel lines. Image widths were measured in the 220 reflections when the image was inside, and when it was outside (on reversing $\underline{g}$), and the mean taken. For 200 reflections image widths could only be measured when $\underline{g} \cdot \underline{b}$ was +ve, as the image became very faint when $\underline{g}$ was reversed. These measurements, carried out on a large number of dipoles, gave the estimated dipole widths of between 100 and 150 Å on the assumption that the mean image width was the approximate dipole width.

In the alternative method, applicable to single images, the dipole width could be assessed on the basis of the intensity of contrast. According to Wilkens and Hornbogen (1964) and Seeger (1964), the intensity of contrast decreases very rapidly when the width of the dipole becomes smaller than about one-quarter of the extinction distance. Similarly, on arguments based on dynamical theory it can be approximately shown that the image width and its intensity decreases very rapidly for dipoles of width less than about 40 Burgers vectors (Cass and

Washburn 1966). In aluminium the extinction distance for 200 reflection is 673 Å for 100 kV electrons (Hirsch et al 1965c) and 854 Å for 200 kV electrons, while the Burgers vector is 2.86 Å. The contrast from the observed faulted dipoles is quite strong and is comparable in intensity to that from single dislocations. Thus on the basis of this strong contrast it could be concluded that the width of the dipole is over 100 Å, and certainly not much less than this value.

3.4.4. Computation of dipole images. Image contrast for narrow dipoles has previously been calculated on the kinematical theory (Wilkens and Hornbogen 1964) as well as on two-beam dynamical theory (Steeds 1967b). These computations, for different dipole widths, consist of profiles of the intensity variation across a cross-section of the dipole. The true widths of the dipoles can then be found by comparison of the microdensitometer trace of the dipole image with the computed profiles.

To make full use of the topological information contained in the images of defects taken at a small value of the deviation parameter w, Head (1967) has developed a procedure where the computer prints out a simulated image on a basis similar to the half-tone principle. This enables a direct visual comparison of the defect image to be made with the computer printout. Humble (1968) has extended the program to compute images from a configuration containing two parallel dislocations and up to three stacking-faults. This method can be used to find the width of a narrow faulted dipole by computing images for given diffraction conditions under which a set of electron-micrographs of the dipole has been taken. As, for given diffraction conditions, the characteristic contrast of the image (i.e. the variation of the black and white along the image), is a function of the dipole width, images are computed for the possible values of dipole width. The actual width of the dipole

can then be determined by matching the micrographs with the computed images.

Computation of images of the faulted dipoles in aluminium was undertaken on the above principle. The configuration of the dipole was assumed to consist of an intrinsic fault on a {111} plane bounded by Frank partials (discussed in Chapter 4 and illustrated in Figure 4.7(a)). All the computations, based on the data and the micrographs supplied by the author, were done on a CDC 3600 computer of CSIRO at Canberra, Australia, by Dr. P. Humble, and all the results, deductions and suggestions described in this subsection are his. The purpose of the computations was to find the actual width of a faulted dipole by matching the observed image with the image computed for a possible width. It was also intended to find the least width of the faulted dipoles in aluminium which would, in principle, still be visible in the electron microscope, and to ascertain the optimum diffraction conditions for observing such narrow dipoles.

Most of the microscopy during observation of the dipoles, and the determination of their Burgers vector, was done using the anomalously high transmission region corresponding to a comparatively large deviation parameter, i.e. $w = 1.0$. The images in such a case show very little characteristic contrast and are not suitable for image computing. For image computation, additional micrographs were taken in various values of w. As expected, the pictures for low values of w, < 0.5, were 'full of character'. The specimen chosen was such that the dipoles did not lie in the foil plane as the computer program is not valid in such a case.

A set of electron micrographs of a faulted dipole was taken on the 200 kV electron microscope, and images were computed for this dipole. Figures 3.9 and 3.10 show two micrographs of this dipole with the computed images that give a near match. The conditions corresponding

(a)

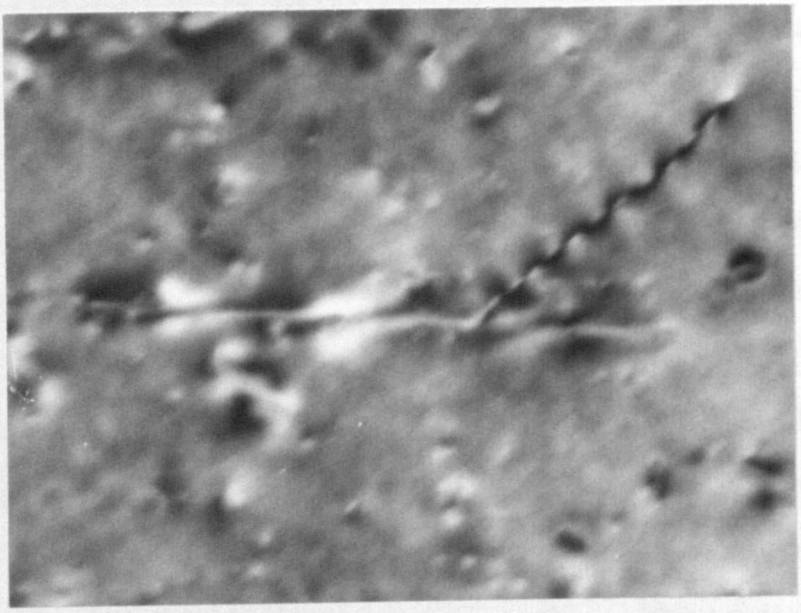

(b)

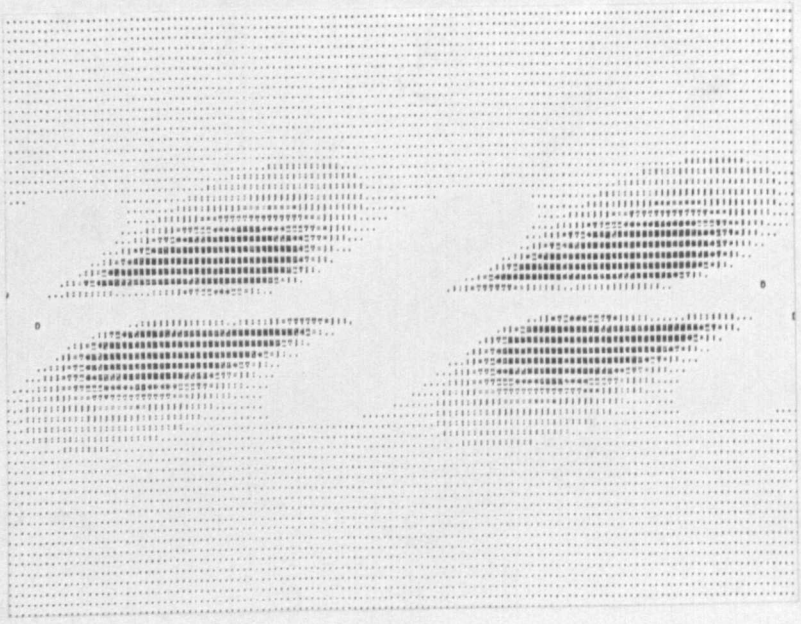

Figure 3.10. (a) The electron micrograph, and (b) the computed image for the same dipole as shown in Figure 3.9, and for the same conditions but with w = 0.

(a)

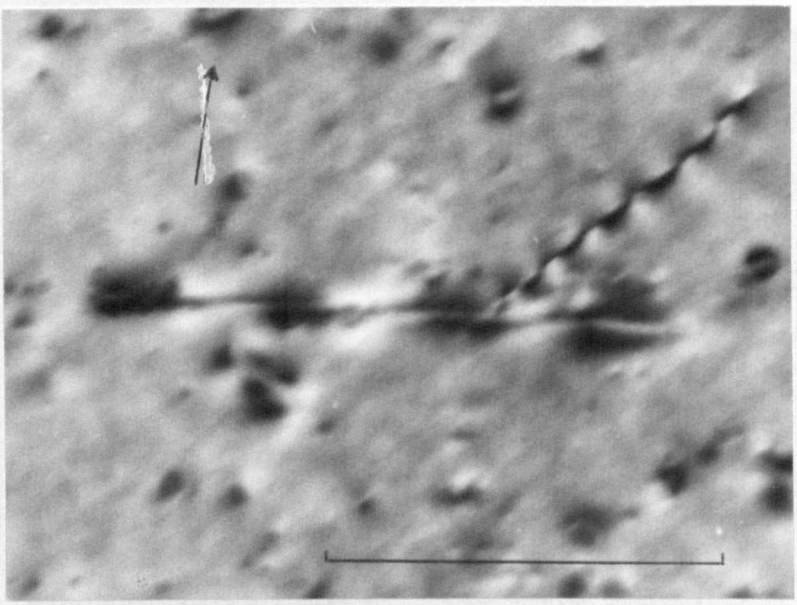

(b)

Figure 3.9. (a) The electron micrograph, and (b) the computed image of a faulted dipole. The micrograph taken, and the image computed, under the conditions given in the text. $w = 0.4$.

Foil normal : $[7\bar{3}\bar{2}]$; Beam direction : $[3\bar{1}0]$; $\underline{g}$: $00\bar{2}$; 200 kV.

to the two micrographs are :

Foil Normal	$\underline{n}$: $[7\bar{3}\bar{2}]$
Dipole direction	$\underline{u}$: [110]
Burgers vector	$\underline{b}$: $\frac{a}{3}$ $[1\bar{1}\bar{1}]$
Plane on which the dipole lies	$(1\bar{1}\bar{1})$
Stacking-fault energy	γ : 135 erg cm^{-2} (Dobson et al 1967)
Elastic constants in 10^{11} dyne cm^{-2}	C_{11} : 10.82, C_{12} : 6.13, C_{44} : 2.85
Anomalous absorption coefficient	-0.03
Extinction distance for 200 reflection	ξ_g : 854 Å
Foil thickness	t : 5300 Å (≈ 6.2 ξ_g)
Depth of the dipole in the foil	extending through 3/5 of the foil and centred approximately at the middle
Dipole length	9000 Å
Electron beam direction	$\underline{E}$: $[3\bar{1}0]$
Reflection	$\underline{g}$: $00\bar{2}$
Deviation parameter	w : 0.4 (Figure 3.9)
	: 0 (Figure 3.10)

The method of measuring w, and the particular choice of the anomalous absorption coefficient, are discussed in Appendix B.

The near-match of the micrographs and the computed images was achieved for a dipole width of 150 Å, which was also the estimated width from the direct measurement of image width of the dipole pictured in the usual w = 1.0 conditions.

A careful comparison of the micrographs and the corresponding computed images in Figures 3.9 and 3.10 shows that the matching can still be greatly improved. However, exact matching was not attempted as, at the low values of anomalous absorption used, the details in the

images are extremely sensitive to the parameters w, t and ξ_g. In order to get an exact match the anomalous absorption, the dipole width, w and t have to be varied over a great many closely spaced values, resulting in a total of over 400 computations. The number of computations could perhaps be reduced if very accurate measurement of t and w, which in this case involved an error of 5 to 10%, could be obtained. Furthermore, the particular dipole whose image was computed had a high density of small loops around it which could have an unknown effect on the actual contrast and thus an exact match may not exist. It has however been demonstrated that, if required, it is possible to find the dipole width very accurately by this method. This method can also be used to differentiate between various defects, e.g. a faulted dipole would give a different image than an unfaulted dipole. Similarly, a faulted dipole also along [110], but with $\underline{b} = \frac{a}{3}[1\bar{1}1]$, shows up differently than the one under consideration. However, to get a unique identification images of the defects must be matched for at least three non-coplanar reflections. For example, under the diffraction conditions given for Figures 3.9 and 3.10, the two 60^0 dipoles along [110], with their Burgers vector in the primary plane $(1\bar{1}1)$, give computed images that are identical with each other and very similar to those given in Figures 3.9 and 3.10 for a faulted dipole.

Computations for optimum diffraction conditions for viewing narrow dipoles showed that most contrast was observed for 220 type reflections, rather than 200 type, and for small values of w, i.e. $w \lesssim 0.4$. It was found that, in principle, there is no lower limit on the dipole width for its visibility. Computations on the type of the dipole specified earlier on, showed that it was visible for a width of 34 Å, with the strongest 220 (type) image reaching about 55% below background intensity and the strongest 200 image about 40%

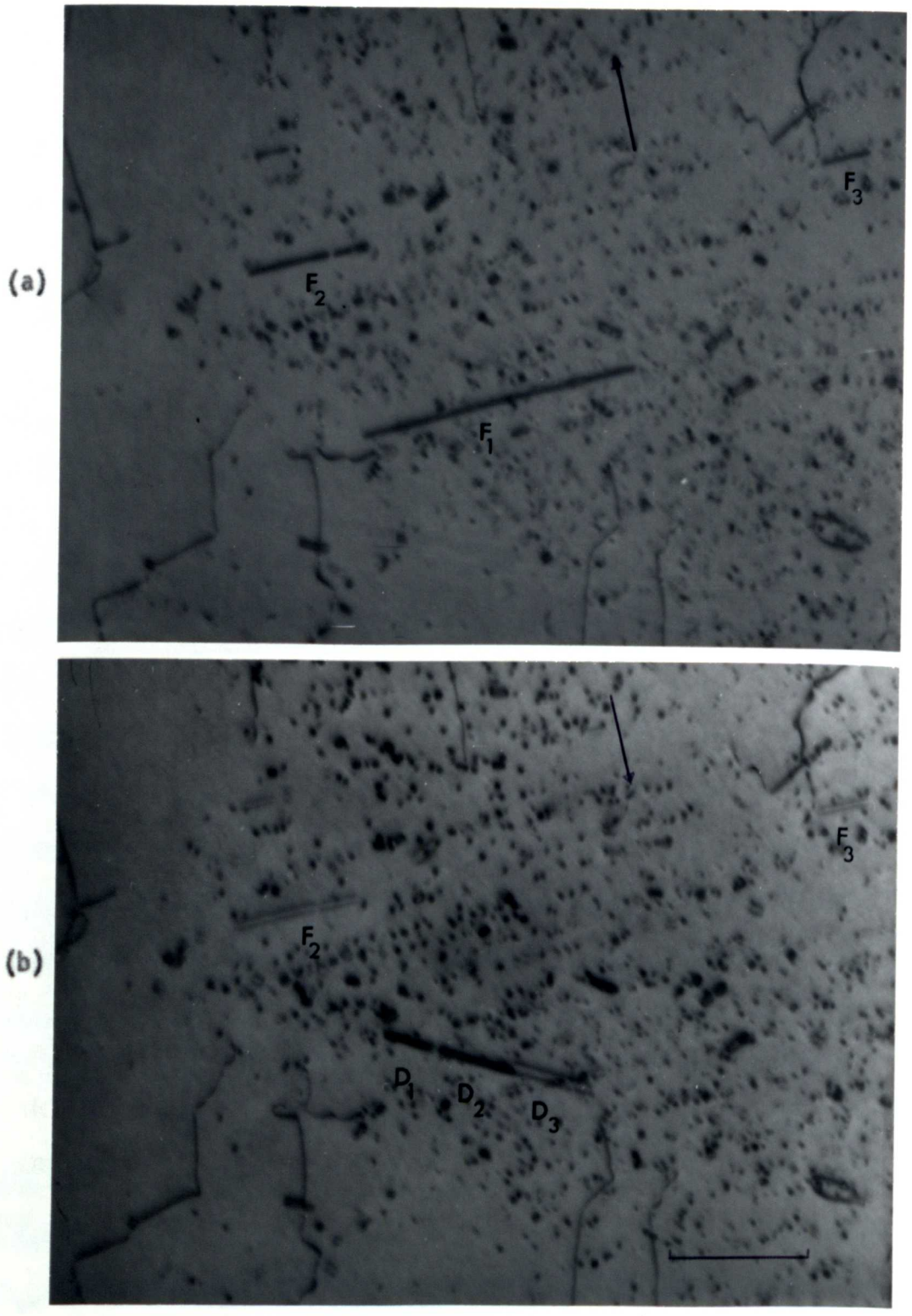

Figure 3.11. The unfaulting of a [110] dipole. The 1.1 μm long dipole F_1 in Figure (a) is seen in Figure (b) to have unfaulted and dissociated into pure edge dipoles D_1, D_2 and D_3. The reversal of contrast of the faulted dipoles with the reversal of $\underline{g}$ is also seen.

Foil normal : $[7\bar{3}\bar{2}]$; Beam direction : $[3\bar{1}0]$; $\underline{g}$: (a) $00\bar{2}$, (b) 002; 200 kV.

below background. An even thinner dipole might still be visible on the micrographs of clear foils with few loops, as a 7% below background visibility-criterion is known to work for dislocations. Even a 5 Å wide dipole was visible when computed in what is probably close to the optimum condition for detecting the dipoles, i.e. using the 311 reflection closest to the Burgers vector.

The above computations have served a very useful purpose in that these have fully borne out the deductions made experimentally about the nature and the width of the defects. In confirmation of the experimental data supplied, the detailed computations showed that the dipole was faulted, was on the appropriate {111} plane with the appropriate Burgers vector, and that its width was the same as that estimated from the direct measurement of the image width.

3.4.5. Stability of the faulted dipoles. Considering the large width of the observed faulted dipoles, and the high stacking-fault energy of aluminium, one would expect the dipoles to be in unstable equilibrium. Such cases have been observed for wide faulted dipoles in silver (Steeds 1967b). However, in aluminium the observed faulted dipoles were found to be extremely stable. Only two cases ever of the unfaulting of a dipole and its change to pure edge orientation were observed. One of these cases is illustrated in Figure 3.11. The long faulted dipole F_1 in Figure 3.11(a) is of vacancy type with $\frac{a}{3}$ $[1\bar{1}\bar{1}]$ Burgers vector and lies along [110]. The dipole is 1.1 μm long and its two ends lie quite near the two surfaces of the 8000 Å thick foil. After being in the electron beam for nearly half an hour, this dipole transformed into three unfaulted dipoles D_1, D_2 and D_3, the total length then decreasing to 0.9 μm. These dipoles, shown in Figure 3.11(b), lay along a direction about 8^0 away from $[\bar{2}\bar{1}1]$. The Burgers vector of the three dipoles, and its sense, was determined to be $\frac{a}{2}$ $[0\bar{1}\bar{1}]$, which with the foil normal $[7\bar{3}\bar{2}]$, makes these dipoles vacancy type (i.e., the extra half planes lie outside

the dipole). The dipole D_3 shows an opposite image reversal to that of dipoles D_1 and D_2. It is assumed that D_3 lies on a plane orthogonal to that on which D_1 and D_2 lie and hence this behaviour. However this could not be confirmed as it was not possible to give the specimen a large tilt about the dipole axis.

The transformation of the faulted dipole probably took place due to the electron beam induced stresses or due to the interaction of the very long dipole with surface. The reaction

$$\frac{a}{3}[1\bar{1}\bar{1}] + \frac{a}{6}[\bar{2}\bar{1}\bar{1}] \rightarrow \frac{a}{2}[0\bar{1}\bar{1}]$$

could be expected to occur and unfault the [110] dipole. The dipole would then flip to the pure edge orientation similar to that shown in Figure 4.7(b), and could also break into three in the process. One of them then took the equilibrium configuration corresponding to $\theta = \frac{\pi}{4}$ and the other two $\theta = \frac{3\pi}{4}$ (or vice versa), where θ is the angle between the slip plane of the dislocations and the plane on which the dipole lies.

3.5. Formation of the Rows of Loops

It has emerged from the earlier sections in this Chapter that a consistently high density of rows of dislocation loops along <110> directions is observed in aluminium given the appropriate quenching and deformation treatment. Even earlier on, in Chapter 1, the observation of similar rows of defects in other metals by various authors was quoted and the mechanisms which could be responsible for their formation were described. The formation of the rows of loops in the present case will now be reviewed with reference to these mechanisms. It will briefly be shown that these rows in aluminium are formed as a consequence of the motion of jogged screw dislocations during deformation. As the investigation of deformation is not described until later, the detailed discussion of the origin of the rows of loops and of the

faulted dipoles, on this basis will be deferred to Chapter 4.

The three possibilities that will be considered for the formation of the rows of loops in aluminium are :

(i) Prismatic punching from a precipitate particle or a gas bubble;

(ii) Degeneration of a helical dislocation by the cancellation of its screw component;

and (iii) Nucleation on the debris left by a moving jogged dislocation.

The first two of these mechanisms can easily be rejected as the sources of the rows of loops in aluminium from the characteristics of these rows.

All the distinctive features associated with prismatic punching were absent in case of the observed rows in aluminium. No precipitate particle or gas bubble, which could be the cause of punching was ever observed. The loops in the rows were vacancy type, of nearly equal size, and regularly spaced. In cases where rows in different <110> directions were observed, they did not emanate from a common centre. In contrast the loops in prismatically punched rows are of interstitial nature, their size decreases as one moves away from the centre of dilation, and the spacing often increases according to the relation given by Bullough and Newman (1960). However, the most decisive evidence against prismatic punching in the case of the rows of loops in aluminium is provided by the fact that the loops in the rows do not have the same Burgers vector, and that none of these Burgers vectors is along the row direction.

Formation of the rows from helical dislocations could also be discounted in the present case. This is because of the extreme rarity of helices in aluminium under the quenching conditions when the rows of loops are observed. Even in the particular conditions, described in Chapter 5, where helices were produced in pure aluminium, no rows

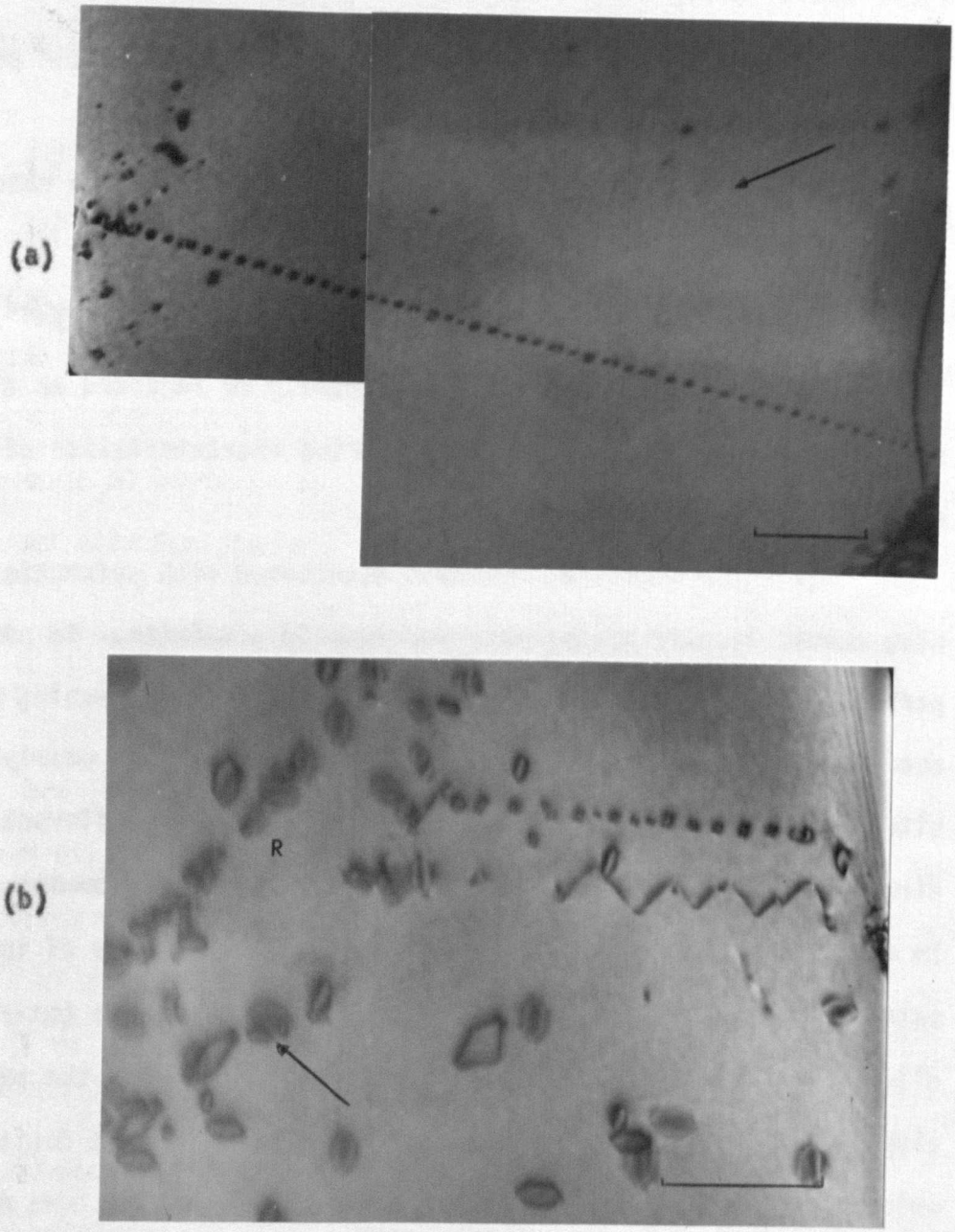

Figure 3.12. Rows of loops in Al 6N formed (a) due to prismatic punching, and (b) from a helical dislocation. Note the characteristic appearance of the two rows. The row R in Figure (b) has features common to those of the rows in previous figures.

(a) Quenched from 630°C to water at 20°C and deformed during the quench. Beam direction : [101]; $\underline{g}$: $\bar{1}\bar{1}1$; 200 kV.

(b) Quenched from 630°C to silicone oil at 0°C and then deformed 4%. Beam direction : [001]; $\underline{g}$: 020; 200 kV.

which could have formed from these were seen. In addition, the rows arising out of helices would be expected to consist of prismatic loops with their Burgers vector along the row direction. The observed rows on the other hand are composed of faulted Frank loops with their Burgers vectors perpendicular to the row direction.

Loops in the rows originating from prismatic punching and dislocation helices are also characterised by the planes on which they lie. The loop plane normals make acute angles with the Burgers vector and hence in cases where the row axis is nearly in the foil plane, i.e. in the observed long rows, the projection of the loops in the rows is elongated perpendicular to the row direction. The loops in the rows observed in aluminium appear elongated along the row direction which is consistent with their Burgers vector being perpendicular to the row direction.

There were in fact two observations of rows of loops in aluminium which had formed due to punching and from a helical dislocation. These two cases are respectively illustrated in Figures 3.12(a) and (b). These rows show all the characteristics, recounted above, for the rows forming due to the two respective mechanisms. It is immediately obvious from the comparison of this figure with other pictures of the rows in aluminium that if any more rows were formed in Al due to punching, or from helices, these could not be confused with those normally observed.

The observed features of the rows of loops in aluminium can be explained on the basis of the last mechanism. The formation of these rows reproducibly only in deformed specimens is of significance in this respect. The debris left behind jogs on moving screws could consist both of narrow dipoles along <110> (whose observation, after growth to a visible size, has been described in this chapter) and of lines of vacancies or vacancy platelets along this direction. It could be that the initial narrow dipoles along <110>, if very long, disintegrate into rows of submicroscopic loops (Washburn et al 1960; Price 1960,

1961a), which subsequently become observable after growth. Some complication could however be envisaged in the climb of the stacking-fault at the position where pinching of the initial dipole occurs. Moreover, the loops in the rows formed this way are all expected to have the same Burgers vector, which is not observed experimentally. It is thus likely that in most cases the rows of loops nucleate on the trails of vacancies or vacancy platelets along <110> left behind short sessile jogs on moving screw dislocations (Gilman and Johnston 1962). The formation of Frank loops from these by further vacancy condensation on the two {111} planes containing this <110> direction would then result in loops having the two $\frac{a}{3}$ <111> Burgers vectors perpendicular to the row direction. Similar assumption has been made by Seidman and Balluffi (1964) and Kiritani et al (1968) to explain rows of tetrahedra along <110> in gold. A more explicit explanation of the above mechanism, which requires a detailed consideration of the motion of jogged screw dislocations is postponed until the next chapter.

3.6. Analysis of the Decoration Conditions

It has been suggested in the preceding section that in aluminium the rows of loops and the faulted dipoles along <110> are formed in the wake of moving jogged screw dislocations. Trails of vacancies or vacancy platelets so formed are hardly expected to be visible in the electron microscope, while the faulted dipoles, even in low stacking-fault energy materials, have been reported to be very narrow and extremely faint (see Chapter 1). This is borne out by the failure to observe these defects in unquenched, but appropriately deformed, aluminium specimens. On the other hand, rows of loops with diameter ≈ 200 Å, and faulted dipoles nearly 150 Å wide, have been found in high densities in quenched and deformed specimens. These facts indicate that, in the latter case, the rows of loops and the faulted dipoles, formed during deformation, must have grown to observable

size by the condensation of vacancies. This process may be regarded as the effective 'decoration' of the original submicroscopic defects by the quenched-in vacancies.

The rows of loops and the faulted dipoles along <110> are generally observed when the density of random loops is low. This suggests that nucleation on original submicroscopic vacancy platelets or dipoles becomes important, and increasingly obvious, when the nucleation of self-sinks is suppressed (Segall and Clarebrough 1964). It was also seen in Section 3.2 that the visibility of the rows of loops and faulted dipoles is very sensitive to the exact quenching conditions. The variation in the density of these defects showed a narrow peak for a judicious combination of carefully adjusted quenching variables. It can be easily shown that this combination of quenching parameters is one which is most appropriate for the decoration of small defects by quenched-in vacancies.

The effect of various quenching conditions on the observation of the rows and the <110> dipoles will now be analysed. Two of these conditions were found to have the most significant effect on the density of these defects. For the observation of a high density of rows of loops and faulted dipoles high specimen purity and low quench temperature, i.e. a low supersaturation, were found to be essential. These two conditions indicate a situation where the nucleation of random loops, whether heterogeneous on impurities or homogeneous on quenched-in vacancies, is inhibited. In other words, this is the situation where a moderate supersaturation of vacancies would exist after quenching without the excessive nucleation of self-sinks. Thus the conditions under which rows of loops and faulted dipoles are observed are precisely those where a decoration phenomenon might be expected.

There was no measureable effect on the density of the rows and

the dipoles of varying the other quenching parameters such as the quenching speed and the specimen thickness. Any small effects due to these parameters can be rationalized in terms of the variation in the vacancy supersaturation. No systematic difference in the density of these defects was observed for different ageing temperatures either. The fact that the density of the rows of loops and the faulted dipoles is independent of the ageing temperatures investigated shows that these were nucleated at a temperature below any of these temperatures. Indeed it has been suggested that these defects are formed as a consequence of deformation, and hence must nucleate at the temperature of deformation, i.e. at -195°C in most cases. The observation of a high density of rows of loops in such specimens when upquenched to 0°C and aged at this temperature contrasts with their rarity in specimens deformed and aged at 0°C. This indicates that the initial defects produced by deformation at low temperature in the former case must have rapidly grown to a stable size in the short time interval during the up-quench to 0°C.

The presence of hydrogen during quenches from temperatures above 600°C was found to be very effective in enhancing the density of the rows of loops. The function of hydrogen in this respect needs discussion in some detail, as during the initial course of experiments its role was misinterpreted and overestimated. In these experiments it was assumed that hydrogen was active in the actual formation of the rows. However it will be shown that this is not the case and that hydrogen is only instrumental in setting up conditions suitable for the decoration of small defects.

Rows of loops, prismatically punched out by dissolved hydrogen, have been observed in magnesium by Lally and Partridge (1966). A similar process, i.e. punching by hydrogen bubbles, could be taking place in aluminium quenched in hydrogen atmosphere. Another possibility was that hydrogen reduced and freed some impurities which aggregated

and then punched out the loops in rows. Both these explanations are however hard to sustain on two counts. Firstly, the solubility of hydrogen in aluminium is not high enough (1/260th of that in magnesium, at 660°C), and secondly, as discussed already, the rows of loops in aluminium do not display any features similar to those of punched rows.

A careful examination of the density of random loops in specimens quenched from hydrogen atmosphere reveals the actual part played by hydrogen. Table 3.1. shows that a specimen quenched from hydrogen from 630°C has a much lower overall loop density than a specimen quenched similarly from air. It is thus obvious that a hydrogen atmosphere diminishes the nucleation of random loops.

There is considerable evidence that a hydrogen atmosphere during the quench favours the formation of voids in a number of metals. Shimomura and Yoshida (1967) have found that the presence of hydrogen greatly increases the density of voids in quenched aluminium, the density in such specimens being over two orders of magnitude higher than that in specimens quenched from dry air. The density of dislocation loops at the same time was nearly 15 times lower in the latter specimens. These authors attribute the occurrence of these voids to the formation of stable nuclei of hydrogen atom-multiple vacancy complexes. Clarebrough et al (1967) found that quenching copper and silver from hydrogen increases both the density and the size of voids. Following Lally and Partridge (1966), they suggest that this might occur due to the dissolved hydrogen preventing the transformation of small voids to vacancy discs which can collapse to form dislocation loops. The formation of voids thus occurs at the expense of the formation of dislocation loops. The active role of hydrogen in void nucleation has recently also been noticed in zinc (Broadway 1969).

In view of the above observations, the enhancement in the density of the rows of loops in aluminium specimens, quenched from a hydrogen atmosphere, could be attributed to a decrease in the nucleation rate of the random loops. Due to the shorter nucleation time of voids, 0.1 sec. at 30°C as compared to 1 sec. for the loops (Kiritani et al 1966b), the number of voids increases sharply in favourable quenching conditions, such as the presence of hydrogen. A complementary fall in the density of loops then results, and hence where dislocation loops are concerned hydrogen acts as if to reduce the effective vacancy supersaturation. Thus hydrogen does not produce the rows themselves, but helps in establishing the appropriate conditions for the decoration of already formed defects.

3.7. Conclusions

A detailed study has been made of aluminium quenched down to low temperatures and then deformed. Various quenching conditions have been investigated and the observation, under suitable conditions, of rows of loops along <110> and narrow dipoles along the same direction is reported. The loops in the rows, and the narrow dipoles, are shown to be faulted with an $\frac{a}{3}$ <111> Burgers vector perpendicular to the <110> direction of the row or the dipole axis. The width of the faulted dipoles, estimated from the micrographs and also measured using computer imaging techniques, has been found to be very large as compared to that of similar dipoles observed in deformed metals of low stacking-fault energy.

The formation of the rows of loops is examined in the context of previously reported mechanisms. It is suggested that the rows of loops and the faulted dipoles originate from the trails behind sessile jogs in moving screw dislocations. The conditions of quenching, i.e. high specimen purity and low quench temperature, where a high density of these defects is observed are then analysed. It is shown that these conditions,

corresponding to a minimization in the nucleation of random loops and yet a retention of adequate vacancy supersaturation, are consistent with those where a decoration of the initially produced submicroscopic defects would occur.

CHAPTER FOUR

THE PRODUCTION OF DEFECTS DURING PLASTIC DEFORMATION

4.1. Introduction

The previous chapter was devoted to the observation of rows of loops and faulted dipoles along <110> in quenched and deformed aluminium. A detailed investigation of the quenching conditions was given and it was shown that these defects were made observable as a consequence of decoration. The formation of these defects was attributed to nucleation on the debris left behind moving dislocations. It was implicitly assumed throughout Chapter 3 that the specimens were given the appropriate deformation treatment. Further, the origin of the rows and the dipoles was only briefly touched upon. These two points, which are of considerable importance in the formation of the defects, will now be elaborated.

While the discussion in the previous chapter was centred mostly around rows of loops, faulted dipoles will be the dominant subject in some sections of this chapter. This is because dipoles can be discussed in such concrete terms as dislocation line energy and stacking-fault energy, while similar terms for platelets of vacancies, from which the rows of loops often form, are uncertain due to the unknown value of binding energy of the vacancies to the platelets and the nebulous boundaries of these platelets. The results of the discussion on dipoles will however be extended to explain qualitatively the formation of the rows of loops.

A description in terms of deformation alone, without a reference to the quenching conditions, is, as before, not very meaningful. This is because of the considerable interaction between the quenched-in vacancies and the dislocations introduced by deformation. While

dislocations can act as sources and sinks for point defects, thus altering the local supersaturation, the quenched-in vacancies affect the motion and the character of dislocations by pinning them or by forming jogs. The term 'standard' quenching treatment will again be used as previously defined but with the specific conditions of a 6N purity and a quench temperature of 550°C.

Section 4.2. investigates the effect of the temperature and the amount of deformation on the density and character of the observed defects. Experiments on single-slip single crystals are also described and a correlation is made of the nature of the rows and the faulted dipoles with the active slip systems. Section 4.3. examines at length the formation of the faulted dipoles, and subsequently the rows of loops, in terms of the dragging of sessile jogs by screw dislocations. A configuration for the faulted dipole is proposed and it is shown that <211> dipoles, <110> dipoles (<211> and <110> being the directions along which the dipoles lie), and rows of loops result in general from jogs of different heights. Section 4.4. explains qualitatively some of the features of the observed defects on the basis of their formation from different jog heights, while section 4.5. discusses some of the previously reported observations in view of the present results.

Extensive use is made in some parts of this chapter of the notation of Thompson (1953) for Burgers vectors and slip planes, and it is thus appropriate to describe it briefly here. Different variations of Thompson's representation have been used since its introduction. The notation used in the following is the same as that of Whelan (1958). The letters A, B, C, D denote the corners of the tetrahedron, $\underline{a}$, $\underline{b}$, $\underline{c}$, $\underline{d}$ the planes opposite these ($\underline{a}$, $\underline{b}$, $\underline{c}$, $\underline{d}$ being the outward drawn normals to the faces), and α, β, γ, δ the mid-points of these planes. The corners A, B, C of the face $\underline{d}$ are labelled in the clockwise order when looking onto this face from outside the tetrahedron (as illustrated in

Figure 4.7). The crystallographic directions corresponding to the faces and the edges of the tetrahedron are given in Table 4.1.

Table 4.1. Crystallographic Connotation of Thomson Tetrahedron (Whelan 1958)

Face of the Tetrahedron	Crystallographic plane	Edge of the Tetrahedron	Crystallographic direction
a	(111)	AB	[011]
		BC	[1$\bar{1}$0]
b	(1$\bar{1}\bar{1}$)	CA	[$\bar{1}$0$\bar{1}$]
		DA	[$\bar{1}\bar{1}$0]
c	($\bar{1}$1$\bar{1}$)	DB	[$\bar{1}$01]
d	($\bar{1}\bar{1}$1)	DC	[0$\bar{1}$1]

4.2. The Effect of Deformation

4.2.1. Temperature of deformation. Four different temperatures of deformation, 0°C, -40°C, -90°C and -195°C, were considered. At 6N specimens were quenched from 550°C to each of these temperatures and then deformed the same amount, i.e. 4%, at the temperature of the quenching bath. The highest density of random loops, rows of loops and faulted dipoles was observed in specimens deformed at -195°C. This confirms the only other report of well-defined rows of loops in aluminium (Meshii 1965), which was also in a specimen quenched down to -195°C, and which had received some accidental deformation. The density of random loops and rows of loops decreased sharply in specimens deformed at -90°C, -40°C and 0°C, and, though <211> dipoles were seen in these specimens, no faulted <110> dipoles were observed. Figures 4.1(a)-(d) show areas containing a high density of the rows of loops in specimens quenched from 550°C to 0°C, -40°C, -90°C and -195°C (respectively), deformed at these temperatures, and given the standard ageing treatment. Note the

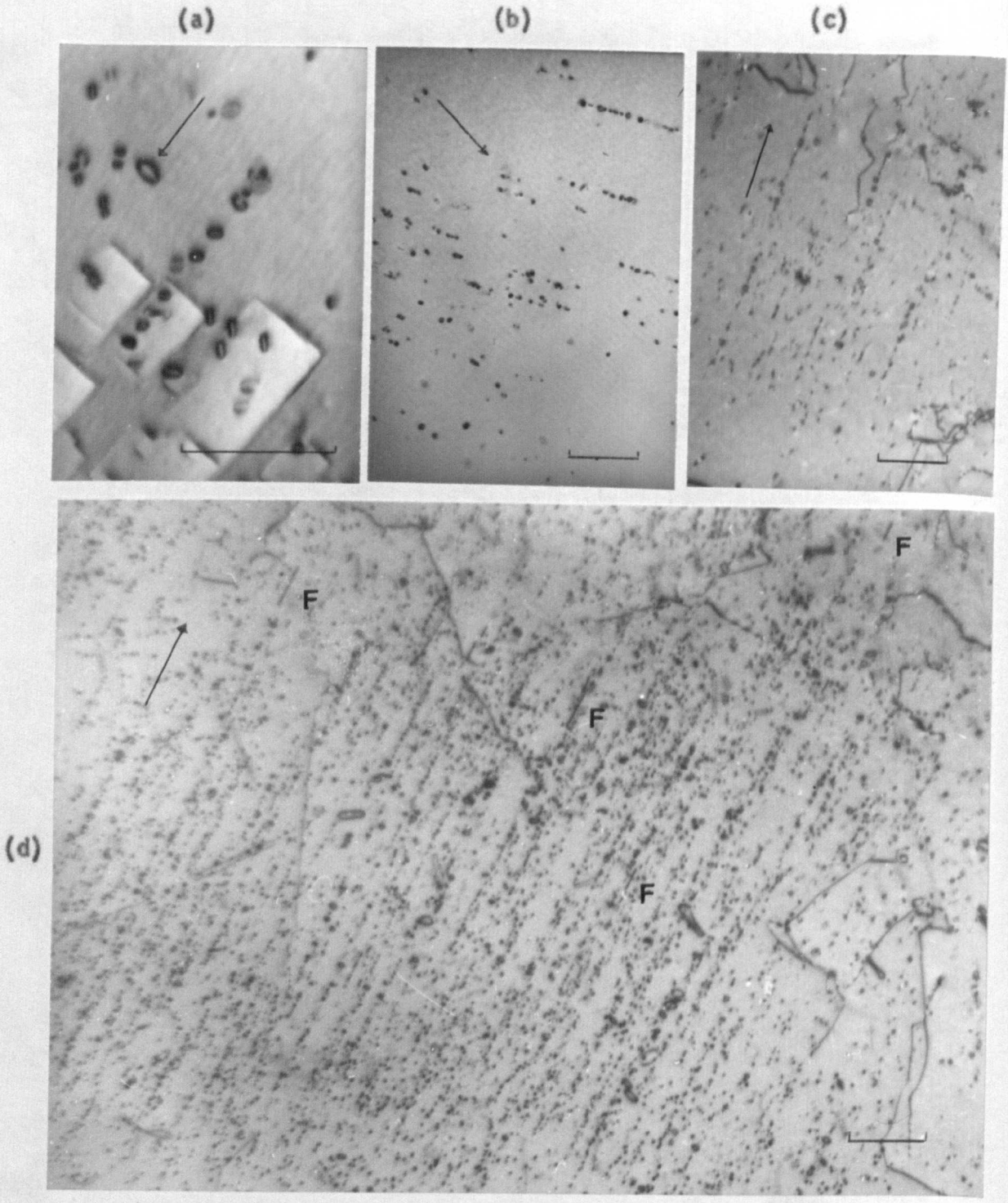

Figure 4.1. Rows of loops in Al 6N quenched down to different temperatures and then deformed 4% at this temperature.

(a) Quenched in silicone oil at 0^{0}C.
Beam direction : [001]; $\underline{g}$: 020; 200 kV.

(b) Quenched in dimethyl-sulphoxide water solution at -40^{0}C.
Beam direction : [101]; $\underline{g}$: 020; 100 kV.

(c) Quenched in methanol at -90^{0}C.
Beam direction : [001]; $\underline{g}$: 020; 100 kV.

(d) Standard quench to -195^{0}C. Faulted dipoles seen at F.
Beam direction : [001]; $\underline{g}$: 200; 100 kV.

extremely high density of the rows of loops in Figure (d), for deformation at -195°C, as compared to that in Figures (a)-(c). Faulted dipoles in case of the specimen deformed at -195°C are also seen at F. It may however be pointed out that a direct comparison between the above results is not rigorously justifiable as deforming at different temperatures also meant quenching to different temperatures. This changes the supersaturation of quenched-in vacancies which, as described in the previous chapter, is a critical parameter for the decoration of defects. A comparison for the same strain at different temperatures is also not strictly valid, as the value of stress for the same strain is different for different temperatures.

Specimens were also deformed continuously at high temperatures during the quench. This was done by removing the slack in the specimen, produced by thermal expansion, when it was at the quenching temperature. The subsequent quench, causing a contraction of the specimen, gave tensile strains up to 2%. Though in such quenches the density of random loops increased over that of loops in undeformed specimens, no rows of loops or dipoles were observed. The defect distribution was comparable in nature to the case of 2% deformation at -195°C, as described below. An entirely different feature of such high temperature deformation during the quench emerges for quenches down to temperatures higher than 20°C, and is described and discussed in Chapter 5.

4.2.2. Amount of deformation. It will be shown in this subsection that, for the specimens given optimum quenching treatment, the amount of deformation profoundly affects the density and the character of the observed defects. The relative concentrations of the various defects observed - random dislocation loops, rows of loops, <211> edge dipoles and <110> faulted dipoles - are a very sensitive function of the amount of strain. Each of these defects, however, shows a different dependence on the degree of deformation. The effect of the amount of

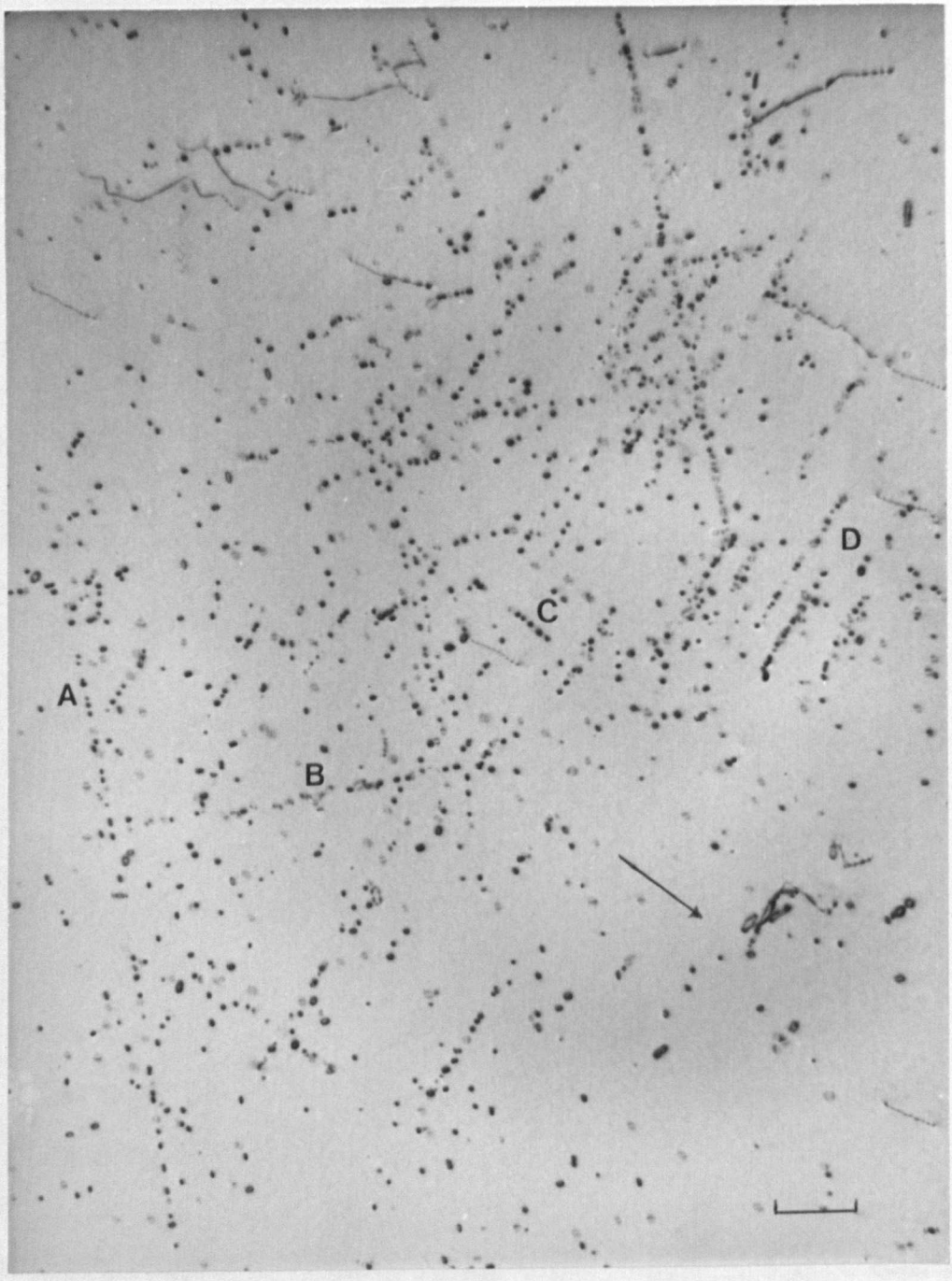

Figure 4.2. An area of high row density in a specimen given the standard quenching treatment, but not deliberately deformed. Rows along four <110> directions are seen at A, B, C and D. The long rows A and B lie in the (001) plane which is near to the foil plane. Beam direction : [001]; $\underline{g}$: 200; 100 kV.

deformation was investigated for specimens given the standard quenching and ageing treatment. The specimens were strained varying amounts in the liquid nitrogen bath, the deformation being completed within 5 sec. of the quenching operation. Though the effect of deformation on defect nucleation is known to decrease with delay in deformation at a temperature of 30°C (Kiritani et al 1966a), it is not expected to be important in the present case due to the very low temperature of deformation where the vacancies are effectively immobile ; the jump frequency of vacancies, assuming a migration energy of 0.60 eV (Doyama and Koehler 1964), is $\approx 10^{3}$ sec^{-1} at 30°C, while it is $\approx 10^{-26}$ sec^{-1} at -195°C.

A detailed description of the defect behaviour with varying amounts of deformation will now be given. A specimen which is not deliberately deformed, henceforth referred to as an 'undeformed' specimen, occasionally shows a high density of rows of loops in areas of low loop density. Such areas of high row density are shown in Figures 3.7 and 4.2 and are from specimens given the standard quenching and ageing treatment but which have not been deformed. These rows of loops are attributed to localized accidental deformation, which is difficult to avoid. This is confirmed by erratic, non-repeatable occurrence of these rows. This factor also makes the estimation of the mean density of such rows very difficult. The mean density of the rows in undeformed specimens could be said to be approximately three orders of magnitude lower than in identically quenched, but appropriately deformed, specimens. Though this proportion would not be fully conveyed, a comparison can be made of Figures 3.7 and 4.2 with the high row density areas in specimens suitably deformed, which are shown in Figures 3.3 and 4.1(d).

One characteristic feature of the rows of loops in undeformed specimens is that these are usually found to lie along several of the <110> directions. Both the Figures 3.7 and 4.2 show rows A to D along different <110> directions. While the long rows A and B are along the

two <110> directions contained in the (001) foil plane, the short rows C and D are inclined at 45° to the foil plane and can be along any of the other four <110> directions. In contrast the deformed specimens contain a more uniform density of rows of loops, which are along one and the same <110> direction. This is very obvious from a comparison of Figures 3.7 and 4.2 with Figures 3.3 and 4.1(d). Also, while deformed specimens show an appreciable number of both pure edge and faulted dipoles, none is observed in undeformed specimens.

The effect of deformation at -195°C is more complicated than that reported for room temperature deformation of quenched aluminium (Kiritani et al 1966a). These authors have shown that the specimens deformed by various amounts exhibit a continuing increase in dislocation loop density, till at 8% elongation the density is nearly an order of magnitude higher than that in undeformed specimens and beginning to saturate. In the case of deformation at -195°C the density of loops increases rapidly from 10^{14} cm^{-3} at zero deformation to reach a maximum of nearly 10^{15} cm^{-3} at about 2% tensile strain. The size of the loops in the deformed specimens decreases to 200 Å from an average of 500 Å for undeformed specimens. The rise to saturation of the loop density, for strains as low as 2% at -195°C, can be explained on the fact that a larger stress is required at low temperature to produce the same strain as at a higher temperature (Garstone et al 1956; Staubwasser 1959). The density versus strain curve, at -195°C, for the loops remains flat till about 3% tensile strain and then begins to fall sharply. While a very high density of dislocations exists at about 8% strain, very few dislocation loops are observed.

Features of greater interest appear as deformation is slowly increased above 2%. Edge dislocation dipoles are seen frequently for strains greater than 2%. These have been reported by numerous workers in case of unidirectional deformation of unquenched materials (Dash 1958; Johnston and Gilman 1960). As expected, in quenched and deformed

single-slip single crystals these dipoles had the primary Burgers vector and lay in the primary slip plane along the <211> direction perpendicular to the Burgers vector.

After 3% extension of the quenched specimen, narrow dipoles along <110> can be observed as well as rows of loops along this direction. The general nature of these defects was described in the previous chapter, while more specific observations will be made in the following sub-section. Here only the correlation of their density and size with the extent of deformation will be discussed. Apart from the direction along which they lie, the <110> dipoles are noticeable because they are very narrow, their image width being about 100 Å as compared to nearly 300 Å for <211> dipoles. The length of the <110> dipoles varied, but the mean length was between 0.4 to 0.5 μm.

When the strain approaches 4 to 5%, the density of random loops, <211> dipoles and <110> dipoles decreases sharply and a high density of rows of loops becomes evident. These rows tend to lie along a particular <110> direction in any one grain, which is the same as that of the faulted <110> dipoles in this grain. Though rows of varying lengths were observed, the mean length was ≈ 1 μm. While the loop density in such specimens is about 10^{13} cm^{-3} the mean density of the rows of loops is 10^{10} cm^{-3}. The row density however is not uniform and varies considerably even within one grain. Thus row densities as high as 10^{13} have been observed in areas of about 10 μm by 10 μm. In these areas a high proportion of the loops occur in rows. Part of such an area was shown in Figure 3.3 and is also shown in Figures 4.1(d) and 4.3(d). The density of rows of loops begins to drop rapidly above 5% strain, mainly because at higher strains dislocation loops are scarce.

The effect of varying amounts of deformation is illustrated in Figures 4.3(a)-(d). The micrographs are taken from specimens given

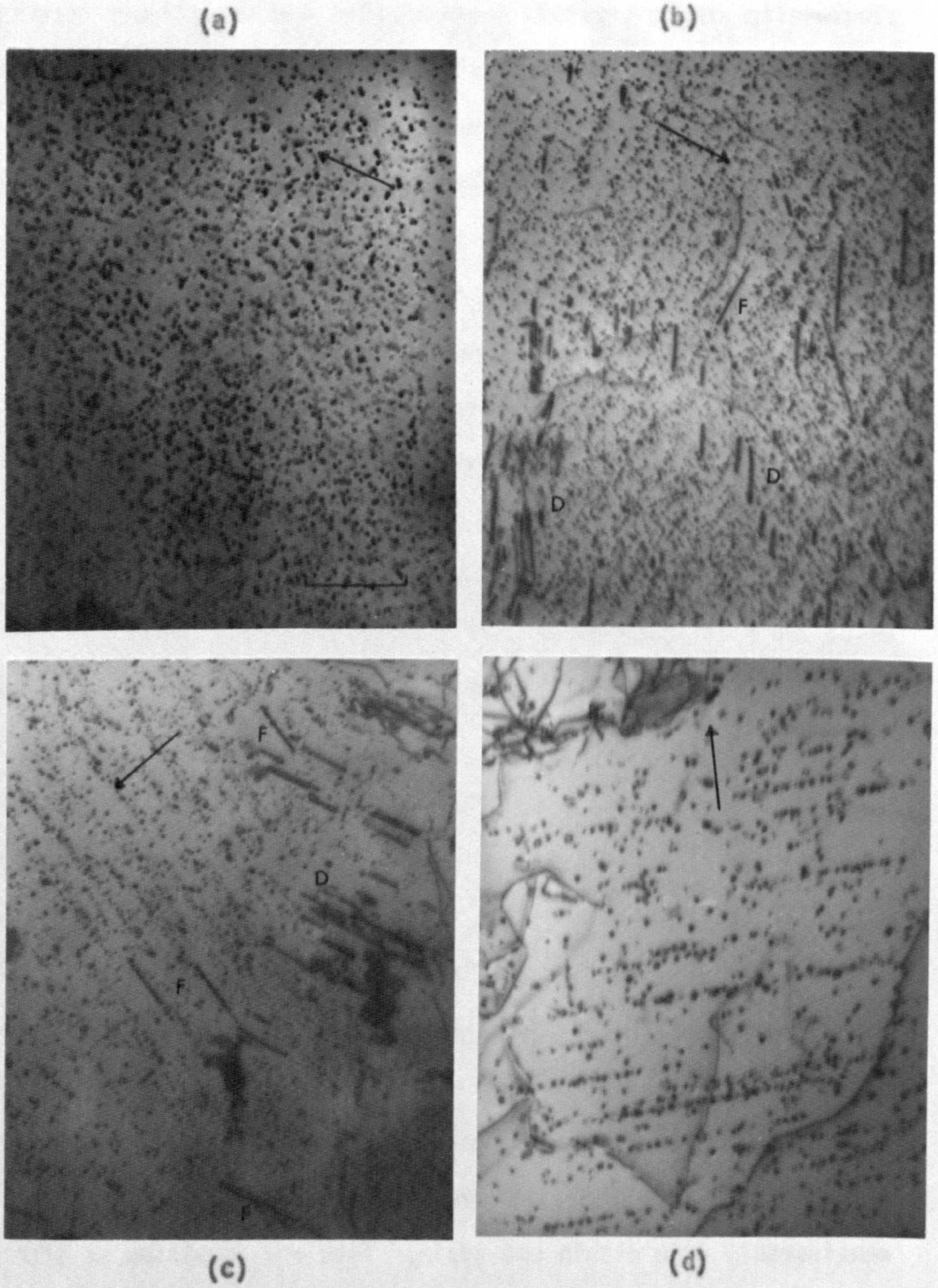

Figure 4.3. Micrographs showing areas from specimens given the standard quenching treatment but deformed different amounts at -195°C.

(a) Zero deformation. Beam direction : [103]; $\underline{g}$: 020; 100 kV.

(b) 2-3% deformation. Beam direction : [001]; $\underline{g}$: 020; 200 kV.

(c) 3-4% deformation. Beam direction : [001]; $\underline{g}$: 020; 100 kV.

(d) 4-5% deformation. Beam direction : [001]; $\underline{g}$: 020; 100 kV.

All the specimens quenched in air atmosphere except that shown in (d) which was quenched in a forming gas atmosphere.

the standard quenching treatment but deformed different amounts after the quench. Figure 4.3(a) is a representative area from a nominally undeformed specimen which shows no dipoles or rows of loops. The size of the loops is comparatively larger and their density smaller. Figure (b) is from a specimen strained 2-3% showing a high density of small loops. A high density of <211> dipoles D can also be seen while a faulted dipole is observed at F. An area containing a high density of faulted dipoles F in a specimen deformed 3-4% is shown in Figure (c). <211> dipoles still exist in a high density at D while the loops appear to be arranged in form of rows along the same <110> direction as the faulted dipoles. Well-defined rows of loops along <110> are illustrated in Figure (d) for a deformation of 4-5%. The density of background loops is low and no dipoles are observed.

A comparison may also be drawn between the sizes and the mean densities of the main defects of interest, namely, <211> dipoles, <110> dipoles, and rows of loops, in conditions where they occur in maximum number. In general, the rows of loops are longer than the <110> dipoles, which are longer than the <211> dipoles. The density of the rows of loops is higher than that of the <211> dipoles, which is higher than that of the <110> dipoles. These results, with defect densities and lengths at the strains, ε_m, at -195°C where each defect is present in maximum density after a quench from 550°C, are given in Table 4.2. Again in small localized areas, 10 μm x 10 μm in extent, these defect densities may be two or three orders of magnitude higher.

4.2.3. Experiments on single crystals. The general characteristics of the rows of loops and the faulted dipoles, such as the direction along which they lie and their Burgers vector, were described in the previous chapter. This analysis was based upon the results obtained from experiments on polycrystalline foils. More specific observations can be made from experiments on single crystal specimens regarding the direction of the rows of loops and the dipoles,

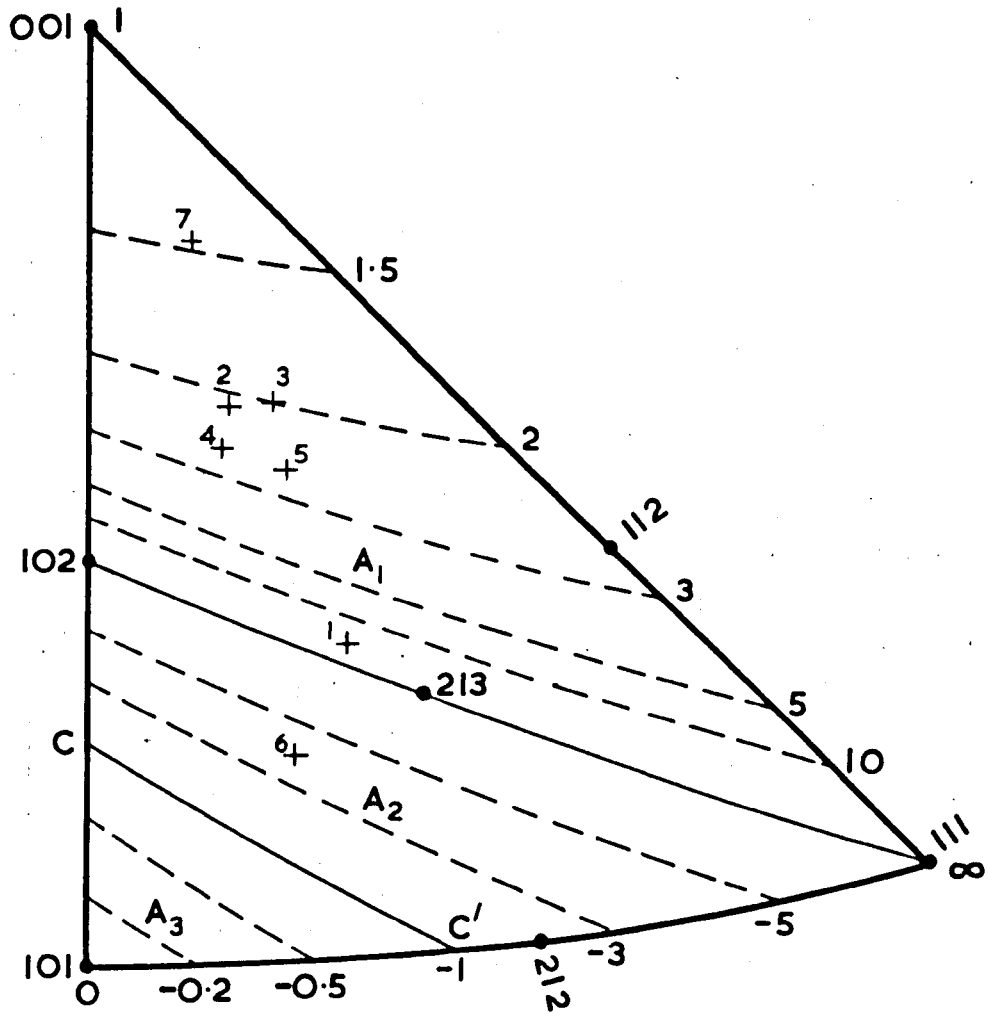

Figure 4.4. Plot of the [001][101][111] stereographic triangle showing the orientations, 1 to 7, of the single crystals studied. Contours are drawn corresponding to the ratio R of the stress on the ($\bar{1}11$) [211] and (111) [$\bar{2}11$] systems.

Table 4.2. Summary of the Observations on Dipoles and Rows

	<211> Dipoles	<110> Dipoles	Rows of Loops
Percentage tensile deformation, ϵ_m, for maximum defect density	2 - 4	3 - 4	4 - 5
Mean defect density at ϵ_m, cm^{-3}	10^8	10^7	10^{10}
Mean defect length at ϵ_m, μ_m	0.3	0.4	1
Dipole width, or loop diameter at ϵ_m, Å	300	100	200

and their Burgers vector, in relation to various slip systems. It is this correlation which is most significant for an understanding of the mechanism of formation of faulted dipoles and rows of loops. The following analysis, which lays greater emphasis on faulted dipoles, is equally applicable to the rows of loops, which, as mentioned earlier, are along the same direction and have the same relation of the Burgers vector to the direction along which they lie.

The experiments consisted of quenching large grained Al 6N thin sheet specimens in the standard manner, deforming them 3 to 4% at -195°C, and giving them the usual ageing treatment. The total number of single-slip single crystals studied in this way was seven. Single slip was ensured by using only those grains which had their tensile axis at least 10° away from the corners of the stereographic triangle, chosen to be [001][101][111], and 5° away from the symmetry axes. Single slip was also confirmed by the fact that most of the edge dipoles observed during electron microscope observation of these crystals had the primary Burgers vector. The orientations studied ranged over a large part of the stereographic triangle and are shown plotted 1 to 7 in Figure 4.4

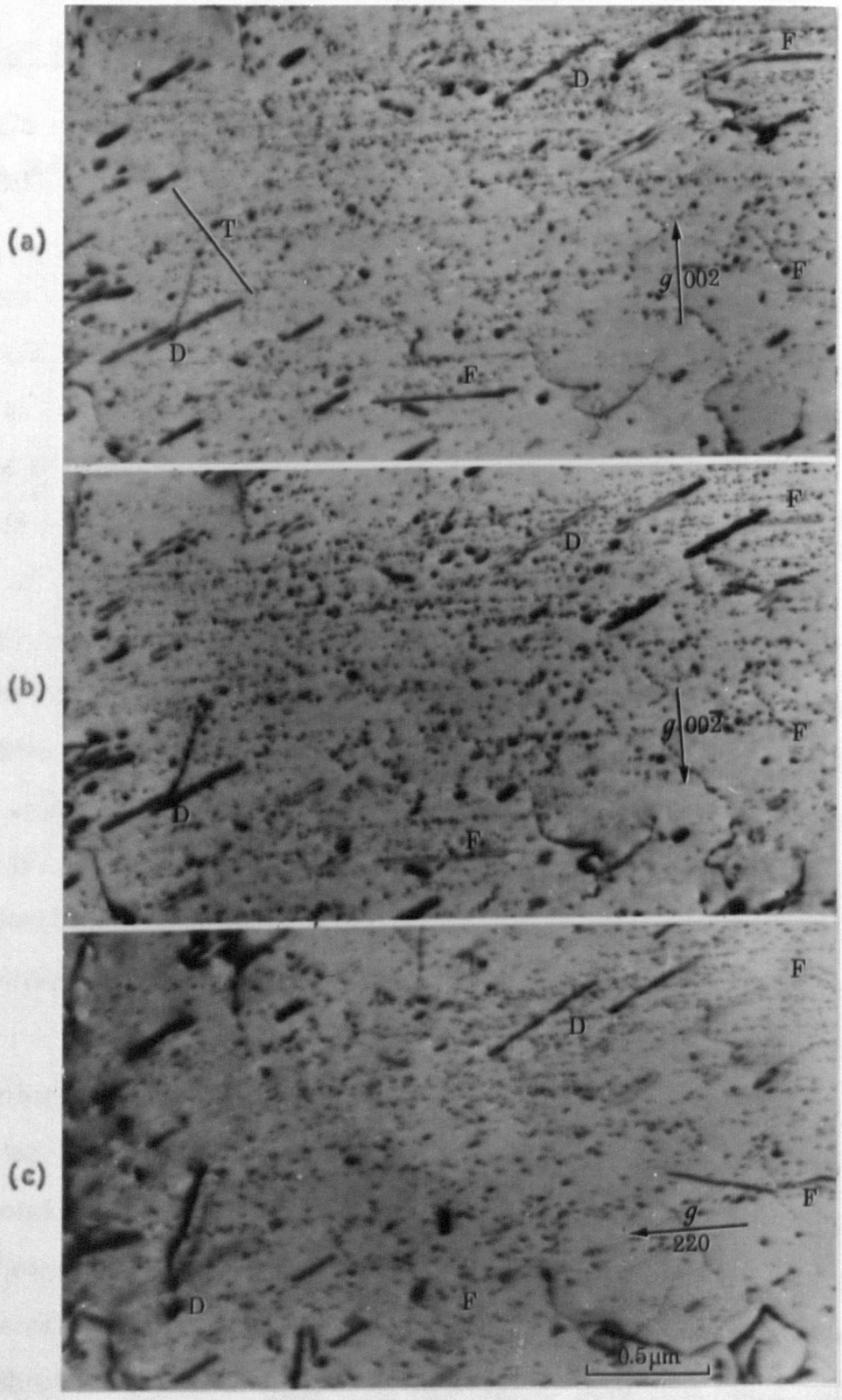

Figure 4.5. Burgers vector analysis for [110] dipoles F in an Al 6N single crystal given the standard quenching treatment and deformed 3% at -195°C. Unfaulted $[\bar{2}\bar{1}1]$ dipoles are seen at D and many loops seem to be aligned in rows along [110]. The projection of the [213] tensile axis in the plane of the micrograph is shown at T.

Foil normal : near $[\bar{3}21]$; Beam direction : $[\bar{1}10]$; 200 kV.

(the stress-ratio contours correspond to a later discussion and may be ignored at present). None of the tensile axes examined lay in the area A_3 of the triangle due to crystal growth difficulties. The significance of this point with regard to the direction along which the faulted dipoles and rows of loops lie will emerge later.

The single crystal specimens given the quenching and deformation treatment described above showed a high density of faulted dipoles, and some rows of loops which lay along the same <110> direction as the dipoles. The direction of these dipoles, their Burgers vector and its sense, were determined uniquely with respect to the tensile axis, using the standard methods described in the previous chapter. The choice of the particular stereographic triangle, [001][101][111], means that the crystals have the primary slip plane $(1\bar{1}1)$ and the primary Burgers vector $\frac{a}{2}[011]$. All the observed faulted dipoles lay along one particular <110> direction in these crystals, the [110] direction. For the tensile axes investigated no faulted dipoles or rows of loops were observed along $[\bar{1}01]$, the other <110> direction, apart from the Burgers vector direction, available in the primary slip plane. The Burgers vector of these dipoles was always found to be $\pm \frac{a}{3}[\bar{1}11]$, and the sense was such that the Burgers vector made an acute angle with the upward drawn foil normal. Thus, according to the convention defined in Section 3.4.1., all the dipoles were of vacancy type.

An analysis of the Burgers vector of dipoles F along [110] in an Al 6N specimen (crystal 1 in Figure 4.4), given the standard quenching and deformation treatment, is shown in Figures 4.5(a)-(c). The tensile axis is approximately 4^{o} from [213], its projection being marked T in the micrographs, and the foil normal is near $[\bar{3}21]$. Figure 4.5(a), where $\underline{g} = 002$ and the dipoles are in contrast, together with 4.5(b) where the dipoles are out of contrast in $\underline{g} = 00\bar{2}$, illustrates the faulted nature of the dipoles. Invisibility of the dipoles in Figure

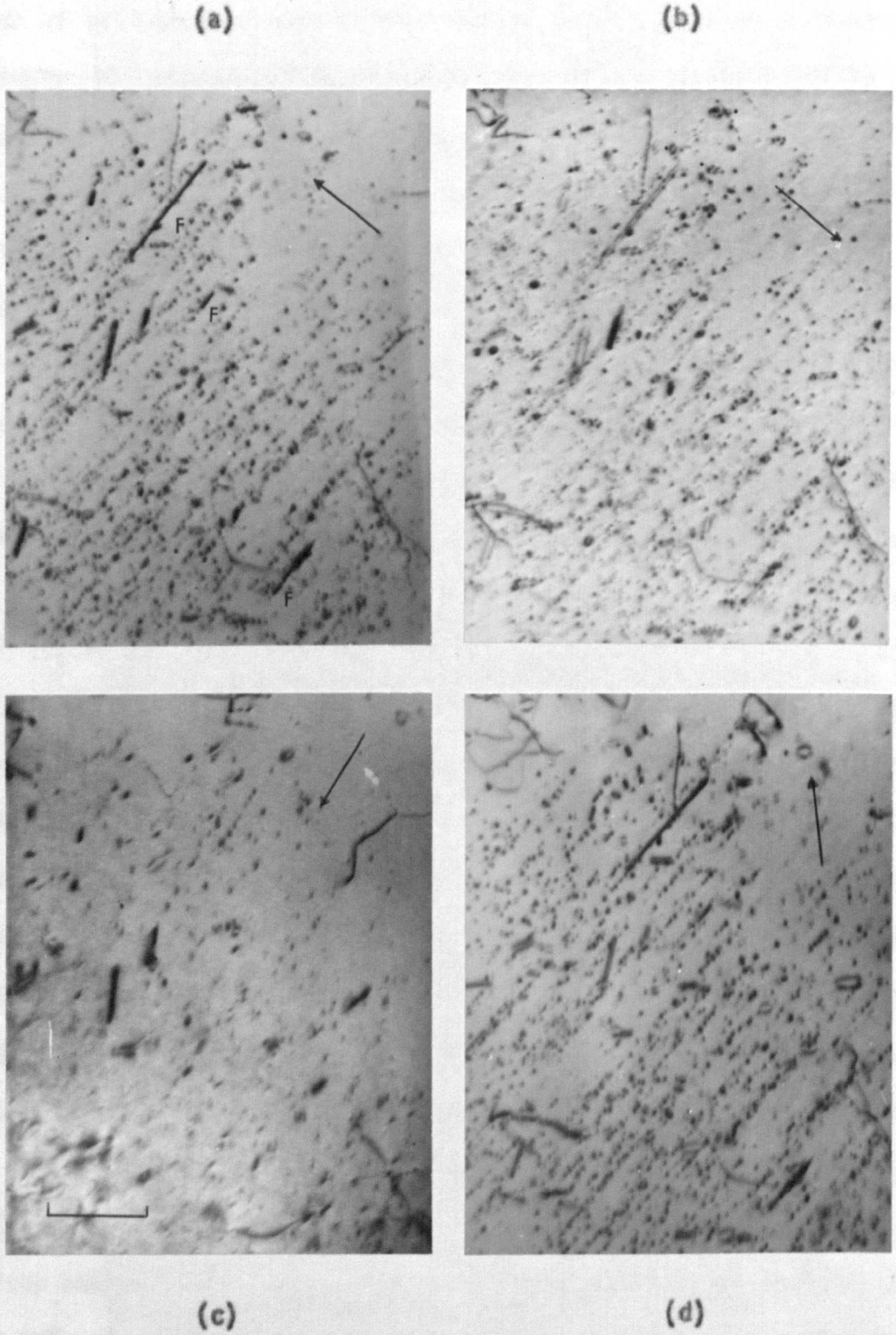

Figure 4.6. Complete Burgers vector analysis for [110] dipoles F in Al 6N given the same treatment as in Figure 4.5. The specimen is a single crystal with a [5 2 15] tensile axis. The same area is pictured in four different reflections, g : (a) $00\bar{2}$, (b) 002, (c) 220 and (d) $0\bar{2}\bar{2}$.

Foil normal : $[7\bar{3}\bar{2}]$; Beam direction : [100] in (a), (b) and (d), and $[1\bar{1}0]$ in (c); 200 kV.

4.5(c), in the 220 reflection, shows that their Burgers vector is perpendicular to [110]. A detailed Burgers vector analysis of the dipoles gives $\underline{b}$ as $\frac{a}{3}[\bar{1}11]$. The unfaulted <211> dipoles, shown at D, are along the $[\bar{2}\bar{1}1]$ direction and have the primary Burgers vector $\frac{a}{2}[011]$.

A complete analysis for [110] dipoles F is shown in Figures 4.6(a)-(d) in a specimen with [5 2 15] tensile axis (crystal 2) and $[7\bar{3}\bar{2}]$ foil normal. As before, Figures 4.6(a), with the dipoles in contrast in $\underline{g} = 00\bar{2}$, and 4.6(b), with the dipoles out of contrast in $\underline{g} = 002$, illustrate the faulted nature of the dipoles. The invisibility of the dipoles in $\underline{g} = 220$ in Figure 4.6(c) shows that the Burgers vector is perpendicular to their [110] axis, while the visibility of these dipoles in $\underline{g} = 0\bar{2}\bar{2}$ in 4.6(d) uniquely identifies their Burgers vector as $\frac{a}{3}[1\bar{1}\bar{1}]$. The vacancy nature of the dipoles is again established from the Burgers vector being at an acute angle to the foil normal. Most of the loops in the observed closely spaced rows along [110] also exhibit the same visibility as the dipoles F and hence have $\frac{a}{3}[1\bar{1}\bar{1}]$ Burgers vector.

Table 4.3 summarizes these results for a number of single crystal foils given the standard quenching and ageing treatment and deformed 3 to 4% at -195°C after the quench. The last column on stress ratio R pertains to a later discussion in Section 4.3.

Table 4.3. Analysis of <110> Dipoles in Single Crystal Experiments

Crystal (Fig.4.4)	Tensile Axis	Foil Normal	Direction of the dipole	Burgers vector	Nature of the dipole	Stress-ratio 'R'
1	near [213]	$[\bar{3}21]$	[110]	$\frac{a}{3}[\bar{1}11]$	vacancy	10
2	[5 2 15]	$[7\bar{3}\bar{2}]$	[110]	$\frac{a}{3}[1\bar{1}\bar{1}]$	vacancy	2.1
3	[216]	$[\bar{1}8\bar{1}]$	[110]	$\frac{a}{3}[\bar{1}11]$	vacancy	2.0
4	[318]	near $[16\bar{1}]$	[110]	$\frac{a}{3}[\bar{1}11]$	vacancy	2.5

Extensive investigation of the rows of loops observed in the above specimens was not made. As the overlap of conditions of high row density and of high dipole density is small, the rows of loops observed in these specimens were not well marked. However a brief analysis showed that all the observations made with regard to the faulted dipoles can be extended to the rows of loops. The rows in these crystals lay along [110] direction only, and consisted of loops with Burgers vector $\pm \frac{a}{3}[\bar{1}11]$ or $\pm \frac{a}{3}[1\bar{1}1]$, the sense again being such as to make the loops intrinsic.

4.3. The Origin of Faulted Dipoles and Rows of Loops

4.3.1. The dipole configuration. Dislocation dipoles along the directions normal to the primary Burgers vector are a commonly observed feature of plastically deformed crystals (Dash 1958; Johnston and Gilman 1960; Washburn et al 1960; Fourie and Wilsdorf 1960; Price 1960, 1961b; Low and Turkalo 1962; Fourie and Murphy 1962; Fourie 1964). In deformed f.c.c. metals these are usually found in high densities towards the end of Stage I (Nabarro et al 1964; Basinski 1964). There are essentially two different mechanisms proposed for the formation of these dipoles. In the first mechanism (Johnston and Gilman 1960), the dipole forms when a screw dislocation containing a sessile composite jog moves under stress. The advancing screw dislocation pulls out an edge dipole perpendicular to itself which can be terminated to form a closed loop. Due to the improbability of cross-slip (which is assumed to form the sessile jog), specially of extended screws, in the easy glide region, a second mechanism was proposed by Tetelman (1962). This considers the formation of a dipole by the interaction of two edge dislocations on parallel slip planes. It has been suggested that the dipoles formed in Stage I in copper arise in this way from edge dislocation trapping (Steeds 1966; Nabarro 1967c). This latter mechanism is also favoured by Steeds (1967a) to account for the bent faulted dipoles observed sometimes in deformed low stacking-fault energy metals.

In addition to the pure edge dipoles described above, narrow faulted dipoles have also been observed in metals and alloys with low stacking-fault energy, and a comprehensive report of these observations has already been given in Chapter 1. The formation of these dipoles by the motion of screw dislocations containing extended 60^0 jogs has been considered by Hirsch and Steeds (1963). The jog is dissociated on the conjugate or the critical plane on which it lies into a Frank and a Shockley partial. As the screw dislocation moves in the primary plane the Shockley glides along with it, extending the fault on the inclined {111} plane, and forming a dipole bounded by this Shockley on one short side and by Frank partials on the other three. The dipole thus lies along one of the two <110> directions in the primary slip plane other than the primary Burgers vector direction.

Seeger (1964), Seeger and Wobser (1966) and Steeds (1966, 1967a) have suggested an alternative process for the formation of faulted dipoles by the dissociation of unfaulted 60^0 dipoles (i.e. Burgers vector at 60^0 to the dislocation line) lying along <110>. Each of the two dislocations in this dipole dissociates into a Frank and a Shockley partial on the inclined {111} plane along whose intersection with the primary plane the dipole lies. The two Shockley dislocations then glide together and annihilate, while the Frank dislocations dissociate on the primary planes into stair-rod and Shockley dislocations. The final configuration thus consists of stacking-faults on two parallel primary planes connected by a stacking-fault on an inclined {111} plane, with the stair-rod dislocations at the two bends in the faults and the Shockley dislocations at the extremities of the faults. Depending on the angle between the inclined faults either an S or a Z shaped dipole can result. A Z-dipole with all the faults intrinsic is expected to be of the lowest energy.

The detailed mechanism for the formation of faulted dipoles in

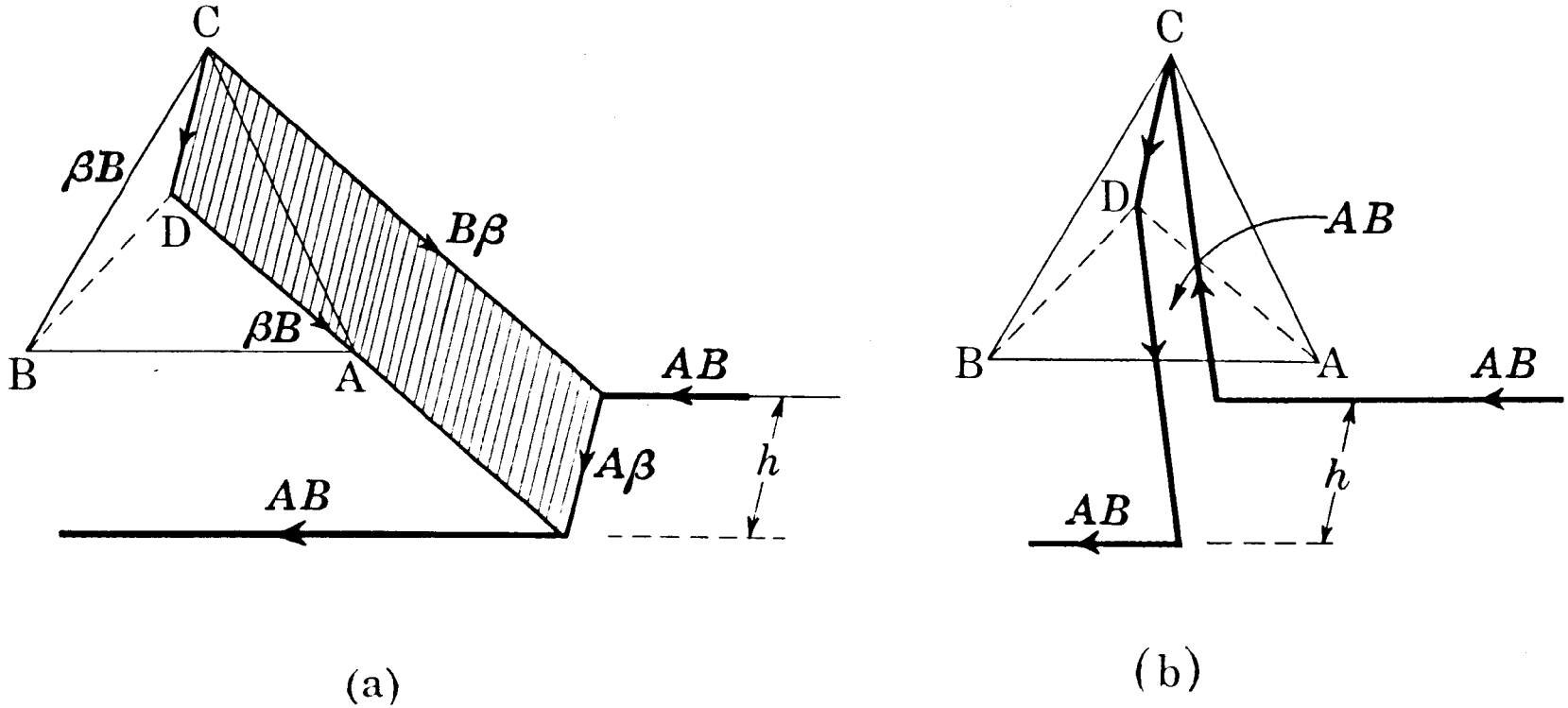

Figure 4.7. The formation of dislocation dipoles from a screw dislocation AB on $\bar{c}$ containing a 90° jog CD of height h.

(a) The formation of a faulted dipole along DA on the conjugate plane b.

(b) The formation of an unfaulted dipole which lies perpendicular to the screw AB.

aluminium as a consequence of deformation will now be described and the configuration of these dipoles given. A treatment similar to that of Johnston and Gilman (1960) will be adopted for the formation of these dipoles by considering the motion of a primary screw dislocation containing a sessile jog. The sessile jog could have formed in two ways. Due to the high stacking-fault energy of aluminium, the dissociation of screw dislocations is likely to be small, and hence these can cross-slip easily to form jogs. The alternative origin of the jogs, more appropriate to the case of quenched aluminium, is likely to be by the interaction of quenched-in vacancies with the screw dislocations. In the following discussion a jog in a dislocation will be regarded as a macroscopic segment of the dislocation along a <110> direction (Hirsch 1962). The height of the jog will however be restricted to be smaller than that above which the two segments of the parent dislocation near the jog behave independently of each other (Gilman and Johnston 1962).

The formation of the faulted dipole by the motion of a screw dislocation AB is shown schematically in Figure 4.7(a), while that of an unfaulted <211> dipole is illustrated in Figure 4.7(b). If $(1\bar{1}1)$ $[011]$, i.e. AB on $\bar{c}$, is chosen as the primary slip system, then the primary screw dislocation AB can have jogs along $[\bar{1}0\bar{1}]$, i.e. CA, $[\bar{1}10]$, i.e. CB and $[01\bar{1}]$, i.e. CD. Due to the high stacking-fault energy of aluminium it can be assumed that the 60° jogs along CA and CB do not dissociate and hence are glissile on the cross-slip plane. During the stress induced motion of the parent dislocation these jogs are likely to glide laterally along the dislocation and annihilate with the jogs of opposite sign. Due to this fact, a dissociation under stress of the 60° jogs, as proposed below for the 90° jog, is not envisaged. The only sessile jog on the dislocation AB is thus the 90° jog along $[01\bar{1}]$, CD.

When the dislocation AB moves, three distinct things might happen depending on the relative height of the sessile jog. In a situation similar to that described by Johnston and Gilman (1960), the dislocation

might pull out an edge dipole perpendicular to itself, i.e. along the $[\bar{2}\bar{1}1]$ direction. This is illustrated in Figure 4.7(b). Alternatively, if it is energetically favourable, the sessile jog may dissociate on either the conjugate plane b or on the critical plane a into a Frank and a Shockley partial. The Shockley can then glide under stress on either plane b or plane a to give, respectively, a faulted dipole along $[\bar{1}\bar{1}0]$, DA (as shown in Figure 4.7(a)) or along $[\bar{1}01]$, DB (unillustrated). Finally, for small jog height, the jog along CD may climb as the dislocation AB moves, leaving behind a platelet of vacancies along one of the two directions DA or DB. In all the three cases it is anticipated that the dislocation will eventually cross-slip to leave a closed dipole or a finite platelet of vacancies (Washburn 1963; Li and Swann 1964).

The formation of the faulted dipole will be considered in more detail now. The discussion will be based upon the configuration of the faulted dipole as illustrated in Figure 4.7(a). Due to the high stacking-fault energy of aluminium, it is not expected that the Frank partial bounding the fault would be further dissociated. Thus it is assumed that the S or Z configurations of the faulted dipole, as described by Seeger and Wobser (1966) and Steeds (1966, 1967a) for low stacking-fault energy metals, do not arise.

The two possible dissociations of the 90° jog along CD in dislocation AB are given by :

$$\frac{a}{2}[011] \rightarrow \frac{a}{6}[211] + \frac{a}{3}[\bar{1}11]$$

(i.e. $\underline{AB} \rightarrow \underline{A\beta} + \underline{\beta B}$ on plane b)

and

$$\frac{a}{2}[011] \rightarrow \frac{a}{3}[111] + \frac{a}{6}[\bar{2}11]$$

(i.e. $\underline{AB} \rightarrow \underline{A\alpha} + \underline{\alpha B}$ on plane a)

The resolved shear stresses in the [211] direction on the $(\bar{1}11)$ plane, and in the $[\bar{2}11]$ direction on the (111) plane can then be calculated for all the tensile axes [hkℓ] in the [001][101][111] triangle corresponding

to the $(1\bar{1}1)$ [011] primary system. The resolved shear stress τ is given by the expression

$$\tau = \sigma \cos\phi \cos\lambda$$

where σ is the tensile stress, and ϕ and λ respectively the angles which the tensile axis makes with the slip plane normal and the glide direction. Thus for the resolved shear stresses on the $(\bar{1}11)$ [211] and (111) $[\bar{2}11]$ systems we get ,

$$\tau_{(\bar{1}11)\ [211]} = K\{[hk\ell].[\bar{1}11]\}\{[hk\ell].[211]\}$$

and $$\tau_{(111)\ [\bar{2}11]} = K\{[hk\ell].[111]\}\{[hk\ell].[\bar{2}11]\}$$

where $$K = \sigma/\sqrt{18}\ (h^2 + k^2 + \ell^2)$$

The ratio R of these two stresses is given by

$$R = \tau_{(\bar{1}11)\ [211]} / \tau_{(111)\ [\bar{2}11]}$$

$$= \frac{(-h + k + \ell)(2h + k + \ell)}{(h + k + \ell)(-2h + k + \ell)}$$

Contours for the stress-ratio R have been plotted for the tensile axes in the [001][101][111] stereographic triangle in Figure 4.4. The stress on the $(\bar{1}11)$ [211] system remains positive in the whole triangle. In case of the (111) $[\bar{2}11]$ system the stress is positive in area A_1 and negative in areas A_2 and A_3 of the triangle (Figure 4.4), i.e. the direction of the stress reverses on crossing the $(\bar{2}11)$ zone. This switching of sign makes the stress-ratio R negative in areas A_2 and A_3. It can be seen from Figure 4.4. that there is in fact only a small region near [001] where the stresses on the two systems are nearly equal, and another small region for $h = (k + \ell)/\sqrt{2}$, corresponding to the contour CC', where the stresses are nearly equal, but in opposite directions. Elsewhere either one or the other system dominates. The stress on the

$(\bar{1}11)$ [211] system remains greater than that on the other over most of the triangle except in the small region A_3 where (111) $[2\bar{1}\bar{1}]$ system has higher stress.

If the faulted dipoles are formed in the way outlined above, and if it is legitimate to consider only the macroscopic resolved shear stress, then this stress analysis enables one to postulate the particular <110> direction along which the dipoles would lie for any tensile axis. Thus for all the tensile axes lying in areas A_1 and A_2 of the stereographic triangle, the faulted dipoles should lie along the intersection of $(1\bar{1}1)$ and $(\bar{1}11)$, i.e. along [110], and their Burgers vector should be $\frac{a}{3}[\bar{1}11]$. Similarly for the tensile axes in the area A_3 the dipoles should be along the intersection of $(1\bar{1}1)$ and (111), i.e. along $[\bar{1}01]$, with their Burgers vector as $\frac{a}{3}[111]$. It is assumed in the above that both vacancy and interstitial dipoles are produced. However, the same jog will not form a dipole of the same nature on the two stress systems. The jog running down along CD in the dislocation AB (Figure 4.7(a)), which pulls out an intrinsic dipole on the $(\bar{1}11)$ [211] system, will produce an extrinsic dipole when the (111) $[2\bar{1}\bar{1}]$ system is operative. The jog which produces an intrinsic dipole in this latter system has to run up along DC in the dislocation AB, and this jog will form an extrinsic dipole on the $(\bar{1}11)$ [211] system.

The agreement of this analysis with the experimental observations is excellent. The details, including the tensile axes and the stress-ratios R, for some of the single crystals investigated have been summarized in Table 4.3. All the crystals examined had their tensile axis in the part of the stereographic triangle above the contour CC' i.e. in areas A_1 and A_2. Thus on the basis of the account given above, the stress was always greater on the $(\bar{1}11)$ [211] system. The direction along which the faulted dipoles lay in all these crystals was [110]. Their Burgers vector was $\pm\frac{a}{3}[\bar{1}11]$, the sense being such that it made an acute angle with the upward drawn foil normal, thus making the fault

intrinsic (the extrinsic dipoles formed during deformation are, of course, annihilated in the supersaturation of quenched-in vacancies). The observed direction of the dipoles, and their Burgers vector, is therefore consistent with the calculations of glide stress on the Shockleys as described above. Observations conforming to the formation of faulted dipoles on (111) [2$\bar{1}\bar{1}$] system are expected for the tensile axes in the region A_3 of the stereographic triangle. However, experimental confirmation for this stress system could not be made, as single crystals with the appropriate tensile axis could not be obtained with the strain-anneal method used for crystal growing.

4.3.2. Energy considerations. Static energy calculations have previously been reported for the critical width where a faulted <110> dipole becomes energetically favourable over an unfaulted 60^0 dipole along the same direction (Seeger and Wobser 1966; Steeds 1967a). The cases of both isotropic and anisotropic elasticity, and of S and Z configurations of the faulted dipole, were considered by these authors.

Approximate static energy calculations were also done in case of the present work in order to decide whether a faulted <110> dipole or an unfaulted <211> dipole is likely to form for a jog of given height h (defined as the length of the jog measured along the jog direction, as illustrated in Figure 4.7). A comparison was made between the energy of an unfaulted dipole along <211> and a faulted dipole along <110> formed for the same jog height and the same dislocation motion. Critical jog height below which the faulted dipole was energetically favourable was subsequently derived. The dipole energies were calculated using the formula due to Cottrell (1953a), giving the dipole energy per unit length as

$$E = \frac{Gb^2}{2\pi(1-\nu)} \left[\ln \left(\frac{r}{r_0} \right) - \tfrac{1}{2} \cos 2\theta \right] + r\gamma,$$

where r is the width of the dipole in its plane,

γ the stacking-fault energy, the term involving γ being zero for the <211> dipole,

θ the angle the plane of the dipole makes with the slip plane of the dislocations,

ν Poisson ratio,

G the shear modulus,

r_0 the core radius,

and b the magnitude of the appropriate Burgers vector.

It was assumed that the unfaulted <211> dipole will rearrange itself by glide, to attain the minimum energy configuration corresponding to $\theta = \frac{\pi}{4}$ and a width of $r = h \times \sqrt{2} \times \sqrt{\frac{2}{3}}$. No such movement is possible for the faulted dipole where $\theta = \frac{\pi}{2}$ and $r = h \times \frac{\sqrt{3}}{2}$. In the comparison of energies for a given strain, that is unit movement of the main dislocation line, due allowance was made for the fact that the lengths of the potential <211> and <110> dipoles are in the ratio $1 : \frac{2}{\sqrt{3}}$. Taking $\frac{a}{3}\langle 111\rangle$ as the Burgers vector for the faulted dipole, the energy expressions, for unit dislocation motion, of the <211> and the <110> dipoles then become

$$E_{\langle 211\rangle} = \frac{Gb^2}{2\pi(1-\nu)} \ln\left(\frac{2}{\sqrt{3}} \cdot \frac{h}{r_0}\right)$$

$$E_{\langle 110\rangle} = \frac{2Gb^2}{3\sqrt{3}\pi(1-\nu)} \left[\ln\left(\frac{3}{2\sqrt{2}} \cdot \frac{h}{r_0}\right) + \tfrac{1}{2}\right] + Gb^2 \cdot \frac{h}{b} \cdot \frac{\gamma}{Gb},$$

where b now is the magnitude of the Burgers vector of a perfect dislocation, and r_0 is in units of b.

These equations were used to calculate the transitional jog height h below which the faulted dipole is favoured in aluminium. For comparison similar calculations were done for copper. The numerical values of the various constants used in these equations are given for both aluminium and copper in Table 4.4. The value of $\gamma_{Al} = 135$ erg cm^{-2} is taken from Dobson et al (1967). The use of the core cut-off radius r_0, with values $\frac{b}{3}$ and $\frac{b}{4}$, to include the core energy needs comment. Different values of

Table 4.4. Numerical Values of the Constants used in Energy Calculations

Metal	ν	γ erg cm^{-2}	G dyne cm^{-2}	b Å	$\frac{\gamma}{Gb}$
Al	0.34	135	2.70×10^{11}	2.86	17.48×10^{-3}
Cu	0.35	60	4.85×10^{11}	2.56	4.83×10^{-3}

this parameter, from b to $\frac{b}{5}$, have variously been used (Kroupa and Brown 1961; Jossang et al 1965; Foreman 1967; Hirth and Lothe 1968b). No rigorous explanation for the choice of a particular value of the core radius is available. Incorporation of the core energy in the form of an effective core radius in the logarithmic term has itself been criticized (Crocker and Bacon 1967). However, approximations are also involved in the calculations of the elastic energy, which usually assume large defect dimensions as compared to the core and semi-infinite length of the dislocations, and disregard any contribution from the corners. These assumptions, and the uncertainty in the available expressions for the core energy (e.g. those of Foreman (1955) and Friedel (1964b)) make a more sophisticated approach unjustified in the present application.

The values of the critical jog height, below which the faulted dipoles are energetically favourable, as calculated from the given equations, are tabulated for aluminium and copper in Table 4.5.† The results for $r_o = \frac{b}{4}$ will now be considered, as the faulted dipole is found to be unstable in aluminium for $r_o = \frac{b}{3}$. It is seen that faulted dipoles have a lower energy than the corresponding <211> dipoles below jog heights h of 6b and 46b, respectively, in aluminium and copper. The maximum widths of the faulted dipoles in aluminium and copper, according to these

† The values of critical jog height and energy per atom plane given in a previous publication (Shoaib and Segall 1969) are slightly smaller than those given here. This was due to a minor algebraic error in computation. However, this makes no difference in any of the arguments or conclusions as other approximations in the calculation outweigh this small error and as the results of this calculation have been used to make qualitative deductions only.

Table 4.5. Critical Jog Height below which Faulted Dipole is Favoured

Metal	Core radius r_o in units of b	Critical jog height h in units of b	Å	Faulted dipole width r = (h√3)/2 in units of b	Å	Dipole energy per atom plane eV
Al	1/3	Faulted Dipole unfavourable			-	-
	1/4	6	17	5.2	15	2.7
Cu	1/3	41	105	36	91	5.3
	1/4	46	118	40	102	5.8

calculations are then 5.2b (15 Å) and 40b (102 Å) respectively.

Direct comparison of the above results with the more detailed calculations of Seeger and Wobser (1966) and Steeds (1967a) is not possible as they have calculated for the transition from an unfaulted 60° dipole to a faulted dipole of equal length. Their original assumption of unfaulted 60° dipoles is difficult to understand, as no such dipoles have been observed experimentally, and no mechanism has been postulated for their formation. However, for the sake of reference, their calculated values of critical slip plane separation, H/b, are given in Table 4.6. The values are taken for a Z-dipole consisting of intrinsic faults on two parallel primary planes, separated by distance H/b, connected by an intrinsic fault on an inclinad {111} plane. Results for isotropic elasticity only are quoted, and from the values of H/b, the calculated width, r, of the fault on the inclined plane is also given. Due to the assumption of equal lengths of unfaulted and faulted dipoles, the results of Seeger and Wobser (1966) and Steeds (1967a) should give somewhat larger transitional widths than those calculated in the present work, and this is indeed found to be the case.

The approximations involved in the present calculations have been enumerated earlier on in this section. The errors arising out of these

Table 4.6. Maximum Width of Faulted Dipoles from the Calculations of Seeger and Wobser (1966) and Steeds (1967a)

Metal	$\frac{\gamma}{Gb}$	Critical slip plane separation, H/b	Dipole width r = 1.06 x H/b	Reference
Al	0.017	8	8	Seeger and Wobser
		8	8	Steeds
Cu	0.005	45	48	Seeger and Wobser
		35	37	Steeds

are further aggravated by the fact that the dipole width in aluminium turns out to be so small that even the use of continuum theory might be questionable. Though the quantitative results of these calculations must be treated with caution, some useful qualitative conclusions can be drawn if the final defect energy is assumed to be the only criterion. It is thus obvious from these calculations that above some jog height $h = h_1$ unfaulted <211> dipoles will be formed, while below this critical height two possibilities exist. There may be another jog height h_2 such that in the region $h_2 < h < h_1$ faulted dipoles are formed, while for $h < h_2$ narrow platelets of vacancies are produced. Alternatively, for all jog heights $h < h_1$, platelets of vacancies may form (which collapse during growth in the vacancy supersaturation to give the observed faulted dipoles). In the latter case however, the energy per atom plane of the faulted dipole of equal width should be kept in mind. Corresponding to a jog spanning six atomic planes in aluminium, the dipole energy per atom plane, from Table 4.5., is 2.7 eV. Using the vacancy formation energy of 0.77 eV (Balluffi et al 1963), the comparable energy of isolated vacancies would be 4.6 eV and the energy of a vacancy platelet somewhat less than this value. If these calculations are taken at their face value, the faulted dipole would be favoured over a platelet of vacancies for $h_1 = 6$, and there would be a smaller value $h = h_2$ below

which the vacancy platelet would have lower energy. However, due to the approximate nature of the calculations, and the unknown value of the binding energy of a vacancy in a vacancy platelet, the numerical value of h_2 remains speculative. It is however clear that, whichever way the faulted dipoles form, they are submicroscopic, and to become observable they have to grow in the suitable conditions of decoration described in Chapter 3.

All the discussion until now has been restricted to intrinsic faults only. In his analysis of jog dissociation Hirsch (1962) has assumed that no extrinsic faults are produced, and experimentally as well only intrinsic stacking-faults are observed in f.c.c. metals and alloys (Howie and Valdre 1963). However, as pointed out by Fourie (Nabarro 1967b), extrinsic faults may be formed in the region of high stress associated with a dragging jog. In this case as well, the above arguments would still apply to the formation of faulted dipoles with different values of h_1 and h_2, though these values would be smaller due to higher stacking-fault energy (Kritzinger et al 1969). Such defects, however, will not survive in the present experiments due to the existence of a high concentration of quenched-in vacancies.

4.3.3. Origin of the rows of loops. The creation of rows of loops in aluminium was discussed briefly in the last chapter, and evidence was presented for their formation from the debris left behind sessile jogs on moving screw dislocations. This mechanism will now be examined in greater detail in view of the analysis, given in the previous subsection, of defect formation from sessile jogs of different heights h. It was shown for a 90^0 jog on a screw dislocation that, below a certain jog height h_1, the motion of the dislocation could produce a platelet of vacancies along <110>. The existence of another critical jog height h_2 was also considered such that for $h_2 < h < h_1$ faulted dipoles along <110> were produced, while for $h < h_2$ narrow platelets of vacancies were formed.

Rows of loops in aluminium can result from the break-up of sub-microscopic faulted dipoles, formed in this way, into a string of loops. These loops can then grow to a visible size by vacancy condensation under suitable conditions of decoration. However, the loops in the rows forming from the break-up of dipoles are all expected to have the same Burgers vector. Though a predominance of loops with the same Burgers vector has often been found in the rows, no rows were observed which had all the loops of the same Burgers vector. Thus the formation of rows of loops in this way, if it occurs, is not very frequent.

The formation of rows of loops from the break-up of vacancy platelets, produced by climb of the sessile jogs, appears to be the prevalent mechanism. In this case the loops may well form most frequently on the two {111} planes containing the platelet direction. The original vacancy platelet, extended along a <110> direction and lying on one of the inclined {111} planes, breaks up into a number of smaller vacancy clusters. Only a small amount of rearrangement is now necessary for some of these smaller platelets to rotate about the row direction onto the primary plane, which also contains this <110> direction. In the vacancy supersaturation these clusters grow to a visible size, collapsing to Frank loops sometime during this process. The formation of the majority of rows in this way is confirmed by the observation that the rows generally consist of faulted loops having one or the other of the two $\frac{a}{3}$<111> Burgers vectors perpendicular to the row direction.

4.4. Some Observations on the Effect of Deformation

The formation of narrow faulted dipoles and rows of loops along <110> due to deformation has been adequately described in the last section. However, the detailed experimental observations given in Section 4.2. on the effects of deformation require some further explanation. The points that need clarification are :

(1) The occurrence in high density of various defects, viz. random loops, <211> dipoles, <110> dipoles, and rows of loops, at different levels of strain.

(2) The relative size of these defects.

(3) The relative densities of these defects.

(4) Effect of the temperature at which the specimen is deformed.

An attempt is made in the following to account for these features. However, it may be pointed out that some of this discussion is necessarily speculative in nature. Also, while each of the above features will be accounted for individually, there is no obvious general explanation which could lead naturally to all these results.

It was seen in Section 4.2. that the density of the observed rows of loops and dipoles depends in a complicated manner on the degree of deformation. The complications arise due to the fact that, with increasing deformation, there must be an interaction between various factors such as the growth of jogs, the reduction in the vacancy concentration due to the sweeping up of vacancies by moving dislocations, and the effect of increasing stress on jog mobility. The significant features of the effect of the amount of deformation on defect characteristics were summarized in Table 4.2. These are discussed below in terms of the tensile strain, ϵ_m, where the density of a particular defects is a maximum.

At low values of deformation, i.e. $\leq$ 2%, the random loops are found in a much higher density than in undeformed specimens. This observation can be explained on the assumption that in the early stages of deformation the dislocations mainly have small jogs which move only short distances before being annihilated with the jogs of opposite sign. Thus the resulting distribution of submicroscopic vacancy platelets and/or dipoles consists of a large number of extremely short and narrow defects. Since the vacancy supersaturation is high at this stage most of these defects would be decorated giving the appearance of loops

nucleated at random. A similar increase in the density of loops in quenched aluminium, and of tetrahedra in quenched gold, deformed about 2% at room temperature, was reported by Kiritani et al (1966a, 1968). They attributed this increase in the density of random defects to nucleation on the vacancies produced by the motion of jogged dislocations.

The occurrence of unfaulted <211> dipoles for tensile deformation = 2% (i.e. shear strain of about 4%) is not unusual, as these are a regular feature in most (unquenched) metals deformed at the end of Stage I (see e.g. Nabarro et al 1964). What is surprising is that very few faulted dipoles or rows of loops are observed for this value of strain. The latter is perhaps due to the existence of a very high density of loops at this stage which make indistinguishable any rows that may be present. The scarcity of faulted dipoles is however difficult to explain.

As the deformation is increased above 2% it is likely that the jogs, which are now higher and more stable, move greater distances and produce wider and longer dipoles and vacancy platelets along <110>, which grow in the favourable condition of reduced vacancy supersaturation. The highest density of <110> dipoles is observed for ε_m value of 3 to 4%. For strains above this value the density of both unfaulted and faulted dipoles decreases rapidly. There have been observations of <211> dipoles being cut into smaller loops (Nabarro et al 1964), and of dislocation loops being swept away (Vandervoort and Washburn 1960; Segall et al 1961), by moving dislocations. The submicroscopic faulted dipoles might also be removed by these mechanisms after unfaulting due to the stress fields of the interacting dislocations.

A maximum in the density of rows of loops is attained at ε_m = 5%. At this stage the density of random loops is quite low and the rows of loops are easily distinguishable. A continuing increase in deformation results in a gradual decrease in the density of the random loops, as well

as that of the rows, because the vacancy supersaturation falls below the level necessary for defect growth. The particular value of ϵ_m for the maximum density of rows is presumably determined by a compromise between the formation of a large number of stable nuclei and the presence of an adequate supersaturation of vacancies for decoration. One notable feature of the rows of loops in deformed single slip specimens is that they are all along the same <110> direction. In contrast the rows observed in specimens not deliberately deformed often lie along several <110> directions. This is probably the result of the complex nature of the accidental deformation responsible for the formation of rows in the latter case.

It is also seen from Table 4.2. that generally the rows of loops are longer than the faulted dipoles which are longer than the <211> dipoles. Two reasons can be given for this observation. One is the simple geometric fact that for the same dislocation motion the <211> dipoles are $\sqrt{3}/2$ times shorter than the corresponding faulted dipoles or rows of loops along <110>. The second reason can be understood on the basis of the relative jog heights which form these defects. If the pure edge dipoles, faulted dipoles and rows of loops are initially produced from jogs of height h_e, h_f and h_r, respectively, then, as discussed in the last section, $h_r < h_f < h_e$. The trails formed due to the motion of the parent dislocation would thus be correspondingly wider, and their energy per unit length higher, for larger jog heights. Thus the wider defects will produce a larger dragging stress on the dislocation, restraining its motion to a shorter distance. On this basis, for the same external stress, the rows of loops will be longer than the faulted dipoles, which will again be longer than the unfaulted dipoles.

The relative densities of various defects can also be explained on the basis of the height of the jogs forming these defects. The density of shorter jogs is expected to be higher, so that the defects

formed from smaller jogs would be greater in number. Thus, as observed, the density of the rows of loops is higher than that of the faulted dipoles and the <211> dipoles.

It is not easy to interpret explicitly the effect of the temperature of deformation and to correlate it with previously reported investigations. The complication arises because the Stage I hardening is also sensitive to other factors, such as purity, orientation and size of the crystal (Honeycombe 1961). The reported observations show that, in general, a single-slip single crystal of aluminium, given a shear strain of 8% (the value commonly used in the present experiments), is in Stage I if it is deformed at -195°C, while it is in Stage III if deformed at room temperature (Garstone et al 1956; Staubwasser 1959). However, these results have been obtained for bulk crystals, and a considerable extension of Stage I is known to occur as the crystal diameter is reduced (Garstone et al 1956; Suzuki et al 1956). In the present set of experiments thin sheet specimens, 0.2 mm thick, were used and for these an 8% shear strain probably corresponds to Stage I deformation for all temperatures between -195°C and 20°C. It has also been reported (Noggle and Koehler 1957; Andrade and Aboav 1957) that, apart from the extent of the easy-glide region, temperature has only a small effect on the early portion of the stress-strain curve. It is however known (Garstone et al 1956; Staubwasser 1959) that the stress required to produce the same strain is larger at a lower temperature even in the easy-glide region of single crystals, and this will be more marked in polycrystals.

In view of the brief discussion given above, it would be expected in the present work that, for a given strain, more defects will be produced in specimens deformed at a lower temperature. This, in general, conforms with the experimental observations. If it is assumed however, that this effect is not too large between -195°C and -90°C, say, then

the observation that many more rows of loops are seen at the former temperature of deformation can be used to give information about the stability of the submicroscopic vacancy defects. If these defects are to be decorated they must be stable long enough, at a temperature where there is some vacancy mobility, for growth to occur. It was not possible to make a reliable estimate of the binding energy of a vacancy to a narrow vacancy platelet but the above observation suggests that it is small. In principle, further experiments of this type, where quantitative measurements are made of the density of rows of loops formed at different temperatures above -195°C, could give an estimate of the binding energy. However, in view of the expected spread in the width of the vacancy platelets laid down initially and the considerable scatter in the measurements, this point was not pursued.

4.5. Comments on Reported Observations

Some of the previously reported work on rows of loops and faulted dipoles will now be discussed in context of the results obtained in the present series of experiments. The current observations on the rows of loops in aluminium can be compared with the observations reported previously on quenched and deformed aluminium and gold (Kiritani *et al* 1966a, 1968). Kiritani *et al* (1966a) observed only a few, short and not very straight rows of loops in quenched aluminium, deformed 2.5% in tension at 30°C. This was presumably due to the fact that their deformation was too low, and, more importantly, at too high a temperature. This is indicated by their observation of a higher density of rows when the specimen was deformed at -90°C in bending (Kiritani *et al* 1968). It has indeed been shown conclusively in the present work that the formation of an appreciable density of rows of loops in quenched aluminium requires a much lower temperature of deformation (-195°C) and a much higher amount of deformation (≈ 4%).

The failure of Kiritani *et al* (1968) to observe rows of tetrahedra

in quenched gold when they deformed it 2.5% in tension could again be attributed to too low a strain. The temperature of deformation, 20°C, is high as well, as the vacancy mobility at 20°C in gold corresponds to that at -60°C in aluminium. If the present results on aluminium could be carried over directly to gold, then only a low density of rows of tetrahedra would be expected for deformation at 20°C. The processes, adopted by these authors, of deforming the specimen in bending, and by quenching and up-quenching the specimen between -195°C and 20°C a number of times, however did yield rows. This difference, which they ascribe to the mode of deformation, might be due to the fact that these processes cause more deformation, and moreover in the cyclic quenching experiment some deformation takes place at low temperature. The present author used the quenching conditions of Kiritani et al (1968) in gold, and by deforming 5 - 6% in tension did obtain a relatively high density of rows of tetrahedra. This experiment was also in confirmation of the results of Seidman and Balluffi (1964) who had used similar conditions. This observation, together with the detailed results for aluminium, shows that the production of visible rows of defects, and faulted dipoles, along <110> depends primarily on the thermal treatment and the amount of deformation, rather than on the mode of deformation. This is in contrast to the conclusions of Kiritani et al (1968).

Due to the possible interaction between the quenched-in vacancies and the dislocations it is necessary to be cautious in extrapolating the results obtained in the present work to the case of deformation in unquenched specimens (Hirsch 1968). For example, the 90° jog, discussed in connection with the dipole geometry, probably forms during the process of sweeping up of point defects by a moving screw dislocation. Nevertheless, it is of interest to discuss the relevance of the present results to the formation of the faulted dipoles observed in unidirectionally

deformed f.c.c. metals of low stacking-fault energy. The narrow faulted dipoles in these metals are often bent with their arms along the two <110> directions in the primary slip plane other than the primary Burgers vector direction (see e.g. Haussermann and Wilkens 1966). The formation of such dipoles by the dissociation of 60° jogs and the subsequent glide of the Shockleys, as described by Hirsch and Steeds (1963) for straight faulted dipoles, is of course not possible. This is because a 60° jog along CB in screw dislocation AB on $\bar{c}$ can form a faulted dipole along BD only, while the jog CA can produce the dipole along AD only. However, contrary to the assumption of Steeds (1967a) who favours an edge trapping mechanism, the observed bent dipole along the two <110> directions could in fact be produced by the 90° jog. The jog along CD in dislocation AB can first dissociate in plane b to give a faulted dipole along DA. Under local stress variations the plane on which the fault is being dragged out can change to a, changing the orientation of the dipole to DB. It may be pointed out that by this mechanism only bent dipoles with the two arms at obtuse angle (120°) to each other can be formed, as an acute angle (60°) configuration corresponds to one arm being vacancy type and the other interstitial type. Experimentally as well only bent dipoles with segments at obtuse angle are observed.

The calculations of Seeger and Wobser (1966) and Steeds (1967a) for the transition width below which faulted dipoles are energetically favourable also require comment. These authors have assumed the formation of the faulted dipoles along <110> from unfaulted 60° dipoles of equal length and along the same direction. Such an assumption, however, does not appear well founded. Li and Swann (1964) have shown that long dipoles, misoriented even a small amount from pure edge configuration, are under considerable stress. Thus all terminated dipoles would be expected to be near pure edge orientation. Observations of terminated dipoles in pure aluminium and copper do indicate that their deviation

from edge orientation is very small indeed (Fourie and Wilsdorf 1960; Fourie and Murphy 1962; Li and Swann 1964). This is also confirmed by the observations of Steeds (1967b) in silver and that of the present author in aluminium (Chapter 3), where faulted dipoles were seen to convert upon unfaulting into a near edge orientation. The assumption of Seeger and Wobser (1966) and Steeds (1967a) is even more improbable for bent faulted dipoles as it is highly unlikely that a bent unfaulted dipole with arms along two <110> directions can exist without at least one of the arms reverting to edge orientation. Thus the calculations based on equal lengths of unfaulted and faulted dipoles would give a larger value of the stacking-fault energy for the observed transition width, i.e. an overestimate of the stacking-fault energy. On the basis of the mechanism of formation of faulted dipoles proposed in this thesis it is also likely that stress is important, and hence static energy considerations alone are not adequate to determine the stacking-fault energy from the widest faulted dipole observed. In other words, it might be necessary to take account of the stress in a precise calculation of the jog height h where there is a transition from an unfaulted dipole to a faulted dipole.

4.6. Conclusions

The role of deformation in the formation of faulted dipoles and rows of loops along <110> in quenched aluminium has been investigated in detail. Experimental observations show that these two defects form in high density in specimens deformed at very low temperature (-195°C). The density of the faulted dipoles and the rows of loops shows a complicated dependence on the amount of deformation. The highest density of the faulted dipoles, for standard quenching conditions, is found to occur at strains of 3 - 4%, and that of the rows of loops at strains of 4 - 5%. Experiments on single-slip single crystals have shown that, for the tensile axes examined, the dipoles and the rows of loops lay along one

particular <110> direction, and that all these dipoles had the same Burgers vector.

The formation of faulted dipoles has been examined in terms of the motion of a screw dislocation containing sessile 90° jogs. A configuration of the dipole is proposed on the basis of the dissociation of the sessile jog under stress, and the subsequent glide of the Shockley on the conjugate or the critical plane, thus forming the faulted dipole along one of the two <110> directions in the primary slip plane other than the primary Burgers vector direction. The experimentally observed direction of the faulted dipoles, for given tensile axes, has been found to coincide with that predicted from the calculated stress on the jog.

The transitional jog height below which the faulted <110> dipoles are favoured, as compared to pure edge <211> dipoles, has also been determined from static energy calculations. It is then suggested that the observed rows of loops are formed either from the break-up of these submicroscopic dipoles at an early stage, and/or from the break-up of vacancy platelets formed along <110> by the same mechanism, but without the intermediate stage of dipole formation.

CHAPTER FIVE

SEGMENTED HELICES IN ALUMINIUM AND ALUMINIUM ALLOYS

5.1. Introduction

Previous chapters were devoted to pure aluminium quenched to, and then deformed at, very low temperatures. A new phenomenon was revealed when the investigations were carried over to aluminium quenched to temperatures a little above room temperature and deformed at high temperature during the quench. This was the observation, in such specimens, of segmented helices in the strict sense, i.e. 'helices' consisting of straight segments which make a constant angle with the generator of the prism on which they lie.

Though helices are abundant in many quenched aluminium alloys they are not normally found in quenched aluminium or other pure metals. There is no convincing explanation for this fact though a number of authors have suggested various possibilities. Thomas and Washburn (1963) report that helical dislocations in pure aluminium are unstable under observation in thin foils. They attribute the stability of the helices in the alloys to the association of solute elements with the dislocation line, thus helping to prevent the glide of dislocation segments which can lead to the degeneration of the helix. Smallman *et al* (1959-60) assume that helices 'straighten out' in pure aluminium due to the absence of any impurity pinning, while Amelinckx (1964) suggests that, for the same reason, helices in pure metals readily transform into rows of loops. A more likely explanation for the rarity of helical dislocations in pure metals seems to be that the screw dislocations can cross-slip and annihilate each other easily, especially in a metal of high stacking-fault energy such as aluminium where the dislocations are not extended. The observation of a high density of helices in zone-refined aluminium

in the present experiments goes part-way in confirmation of the last hypothesis.

Section 5.2. deals with the observation of angular helices in aluminium alloys during some subsidiary experiments done for comparison with the results in aluminium. The conditions of quenching and deformation necessary for the formation of segmented helices in pure aluminium are described in Section 5.3. Section 5.4. gives a detailed description of the geometry of these helices in terms of the surface on which they lie and the orientation of the segments. These results are discussed in Section 5.5., and the specific conditions under which helices are formed in pure aluminium gives information about the cross-slip behaviour of screw dislocations. Conclusions are also drawn about the dislocation core energy from the experimental observation that the segmented helices are formed in a very pure and almost elastically isotropic material. Though these last two sections are described entirely in terms of the segmented helices in aluminium, the observations are general and are applicable to the alloys as well.

The orientations of various segments of the helices were determined from four or more micrographs of the same area taken with widely separated electron beam directions. In many cases three or more of these beam directions were non-coplanar. The actual orientations of the segments were then worked out from the stereographic plot of the projected directions in the micrographs. The segment orientations define the pitch to diameter ratio of a helix, which for generality will be described as the angle, θ , between the tangent vector to the helix at any point and a vector parallel to the helix axis.

5.2. Segmented Helices in Aluminium Alloys

The ordinary circular helices, as observed by Thomas and Whelan (1959), can readily be produced in aluminium alloys simply by quenching from temperatures above that of solute solubility. To look for segmented

helices in these alloys thin sheet specimens of Al - Cu and Al - Mg were quenched from 550°C to water at 20°C. Some of these quenches were performed by furnace dropping and some after direct resistance heating as described in detail in Chapter 2.

The specimens were thinned using the methods given in Chapter 2 and were then examined in the 100 kV or the 200 kV electron microscope. Apart from the density of defects being a little higher in the specimens quenched after direct resistance heating the results were essentially the same for the two methods of quenching. In confirmation of previously reported work (e.g. Thomas and Whelan 1959; Embury et al 1962; Eikum and Thomas 1963) a high density of circular helices, varying from specimen to specimen, was observed. However, contrary to the observations of these authors a high density of dislocation loops was often observed in many large areas. Such areas of course contained few helices.

The alloys investigated were :

(i) Al - 4wt.% Cu : Quenched after a short solution treatment for 30 min. at 550°C in air.

(ii) Al - 7wt.% Mg : Quenched after a 15 min. solution treatment at 550°C in air. The magnesium content even after this brief solution treatment is however less than that quoted as considerable magnesium loss is known to occur during this process (Lorimer and Nicholson 1969).

(iii) Al - 0.5wt.% Mg : This was an Al - 7% Mg specimen which had been given a 14 hour solution treatment at 540°C. It was quenched after solution treatment by dropping into water at 20°C. The exact composition of the alloy was determined by electron probe analysis after the solution treatment.

The observation of segmented helices in Al - 4% Cu was very rare. Though the mean density of the circular helices was about 10^{11} cm^{-3} it is not possible to quote the mean density of angular helices as only a few

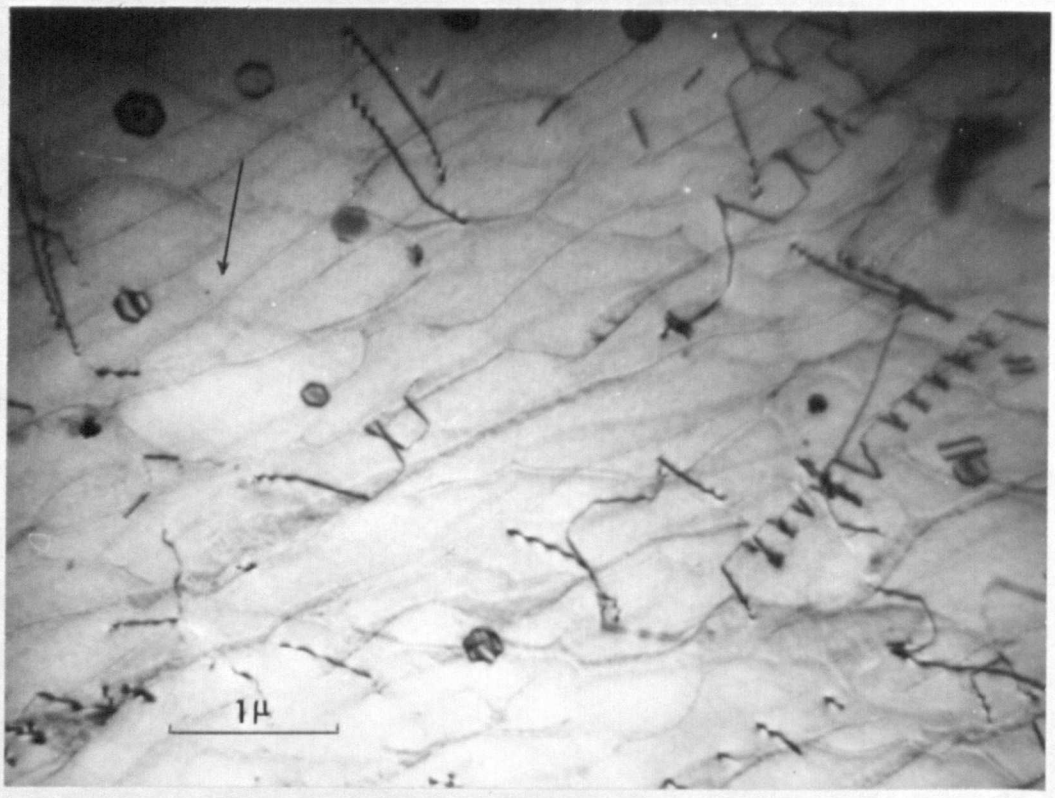

Figure 5.3. Angular helices in a high density area in quenched Aℓ - 0.5% Mg.
Beam direction : [0$\bar{1}$1]; $\underline{g}$: 200; 100 kV.

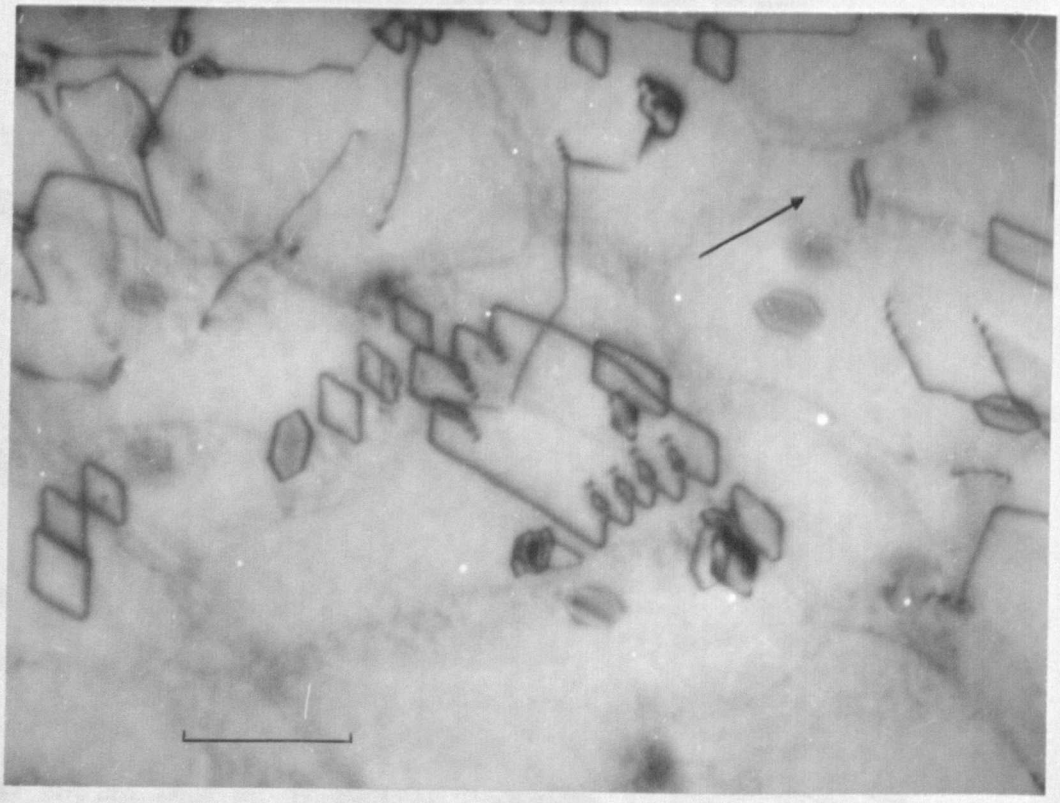

Figure 5.4. Glide loop in Aℓ - 0.5% Mg showing the climb of screw segments into angular helices.
Foil normal : [210]; Beam direction : [100]; $\underline{g}$: 002; 200 kV.
(Micrograph taken by Dr. R.L. Segall).

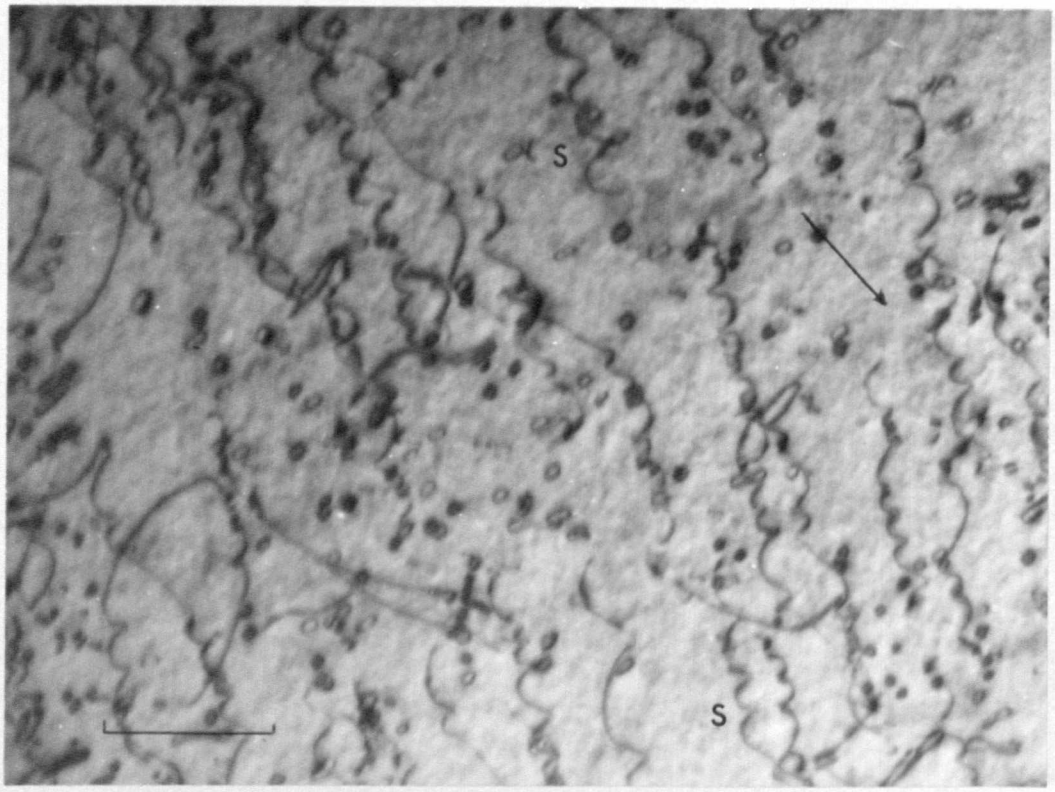

Figure 5.1. An area showing ill-defined segmented helices in Aℓ - 4% Cu. Beam direction : $[0\bar{1}1]$; $\underline{g}$: 200; 200 kV.

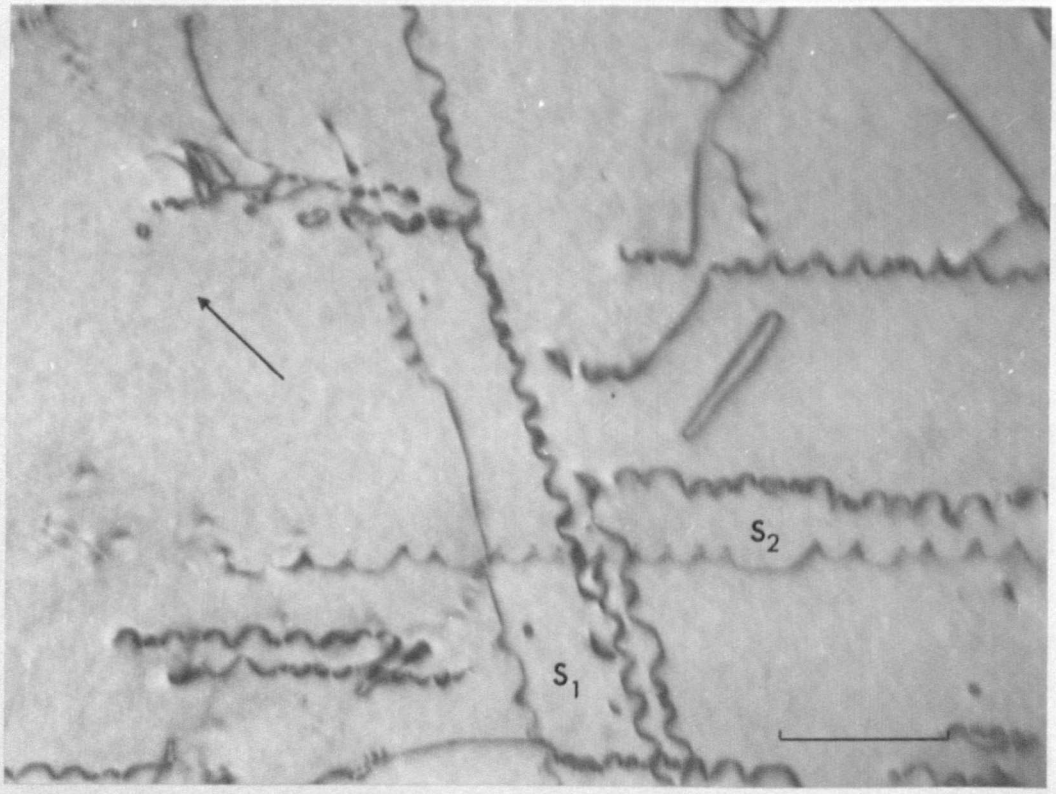

Figure 5.2. An area of Aℓ - 7% Mg containing a high density of angular helices. Helices along $[\bar{1}01]$ and $[101]$ are seen at S_1 and S_2 respectively. Foil normal : near $[0\bar{1}3]$; Beam direction : $[0\bar{1}1]$; $\underline{g}$: 200; 200 kV.

were found in scattered areas, such as that shown in Figure 5.1. The helices at S in the figure appear to be segmented. Al - 7% Mg had a comparatively higher number of seemingly segmented helices. Out of a total density of $\approx 10^{12}$ cm^{-3} helices in these specimens about one-tenth appeared to be segmented. The proportion of such helices may be still higher, because their angular nature is obvious only on careful examination, as the segments, apart from being short, are not always straight. Figure 5.2. illustrates an area of this alloy containing a high density of angular helices. Helices along two perpendicular directions, $[\bar{1}01]$ and $[101]$, are seen at S_1 and S_2 respectively. These observations of angular helices in magnesium rich aluminium alloys corroborate those of Eikum and Thomas (1963) and Embury (1963). These authors observed the angular helices in specimens given either prolonged anneals at 100-120°C or short anneals at 160-180°C. However, the highest temperature at which the specimens in the present work were aged was 90°C for 5 to 10 min. during chemical polishing in the preparation of electron microscope specimens.

Al - 0.5% Mg provided the most detailed observations of well-defined angular helices in the alloys. The density of helices in this alloy was much lower ($\approx 10^{10}$ cm^{-3}) than that in the alloys with a higher solute content. However, contrary to the observations in rich alloys, all the helices in this case were composed of straight segments. These helices consisted of a smaller number of turns of larger radius, and the radius was often not uniform all along the length of the helix. The pitch and the radius of these helices was also quite large and of the order of 2000 Å. An area of Al - 0.5% Mg containing a high density of helices is shown in Figure 5.3. Note the large pitch and diameter of these helices as compared to that of angular helices in Al - 4% Cu and Al - 7% Mg (Figures 5.1. and 5.2.).

Figure 5.4., which is a micrograph taken by Dr. R.L. Segall, shows another area of high helix density in Al - 0.5% Mg, and also

illustrates an interesting feature not commonly observed. The two sides of a large loop which were of screw orientation have climbed to become helices composed of straight segments. Detailed analysis showed that the original loop, from which the defect shown was formed, was a glide loop, i.e. it lay on a {111} plane containing the Burgers vector. The helical parts of this loop are tightly wound, as the segments, which are of approximately equal length (1200 Å), have $\theta \approx 70^{\circ}$. In this respect these two helices are not typical of the segmented helices observed in general in pure aluminium or its alloys.

The mean densities of circular helices, and the mean densities and the maximum densities (in a 10 μm x 10 μm area) of segmented helices in aluminium alloys and pure aluminium are given in Table 5.1.

Table 5.1. Density of Helices in Al Alloys and Pure Al

Metal or Alloy	Mean density of circular helices cm^{-3}	Mean density of segmented helices cm^{-3}	Maximum density, in 10 μm x 10 μm area, of segmented helices, cm^{-3}
Al - 4wt.% Cu	10^{11}	-	2×10^{10}
Al - 7wt.% Mg	10^{12}	10^{11}	5×10^{11}
Al - 0.5wt.% Mg	-	10^{10}	5×10^{11}
Al 6N	-	10^{9}	2×10^{11}

5.3. Formation of Helices in Pure Aluminium

The formation of helices in pure aluminium required much more stringent conditions than those for the alloys. Zone-refined, polycrystalline Al sheet specimens, about 75 μm thick, were held between the movable grips of the quenching jig described in Chapter 2 and direct resistance heated to approximately $630^{\circ}C$. The slack produced in the specimens due to thermal expansion was then removed by moving the grips apart before quenching into saturated brine at various temperatures. This resulted in a continuous deformation of the

(a)

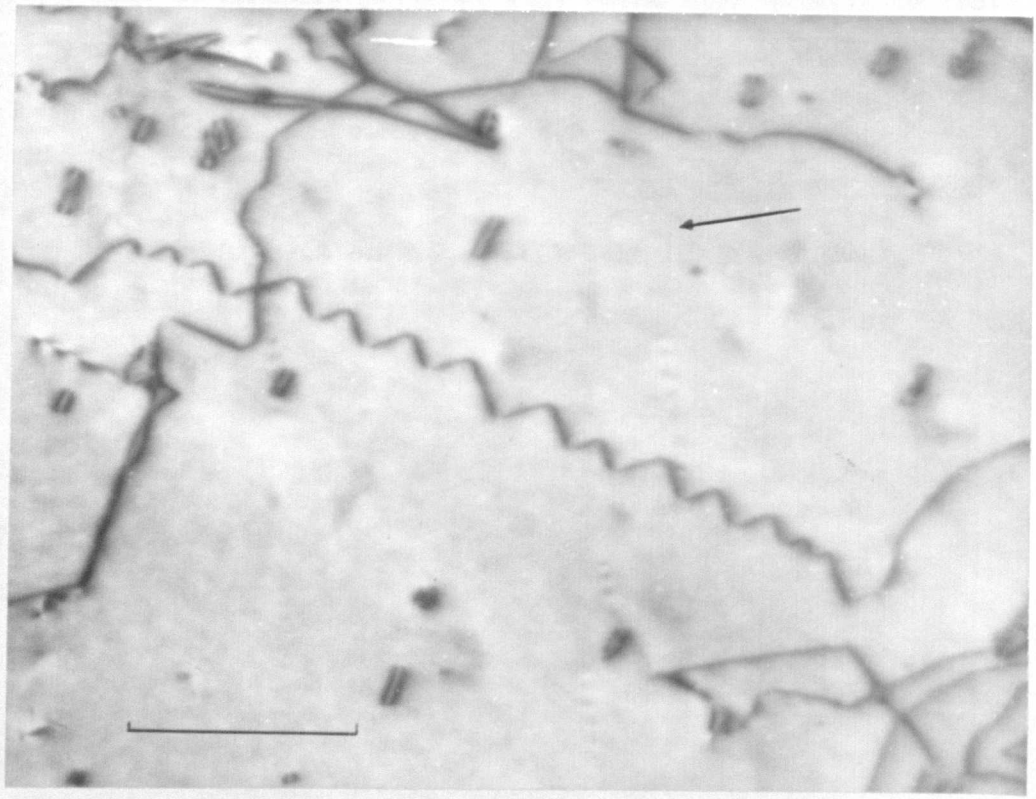

(b)

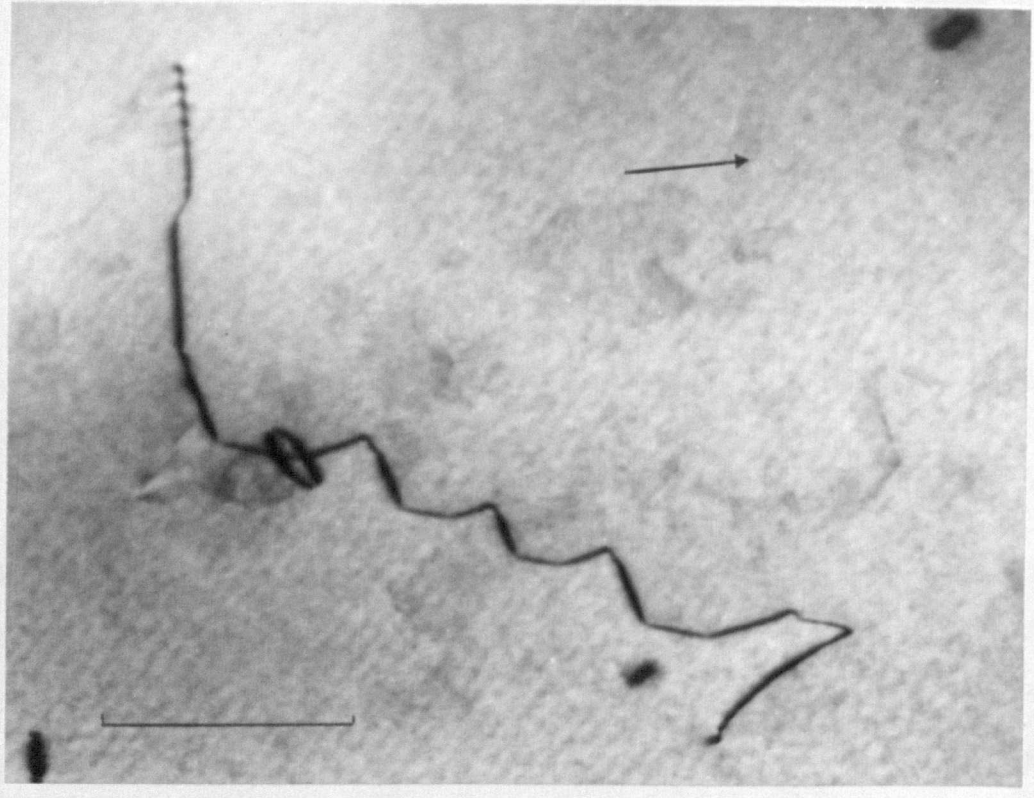

Figure 5.5. Helices in Al 6N quenched down to (a) 20°C in water, and (b) 85°C in brine.

(a) Foil normal : near [213]; Beam direction : [101]; $\underline{g}$: $\bar{1}\bar{1}1$; 200 kV.
(b) Foil normal : near [101]; Beam direction : [123]; $\underline{g}$: $\bar{1}\bar{1}1$; 200 kV.

specimen during the quench. The specimens were aged for about 20 min. at the temperature of the quenching bath and subsequently for 100 hour at 20°C. Appropriately thinned specimens were then examined in the JEM200 electron microscope. The average foil thickness in the areas examined was about 0.5 μm but most of the detailed studies of helices were made in areas about 1 μm thick as the observed length of the helices is greater in such foils.

The observation of the helices was found to be dependent upon two variables - deformation during the quench and the temperature of the quenching bath. Deformation was found to be essential for the production of the helices, and a tensile strain of about 2%, the maximum possible with the method of deformation, was used. The temperature of the quenching bath was found to be a critical parameter for obtaining a high density of helices. Low density of helices, of segmented form, was observed for quenches down to temperatures as low as 20°C and as high as 85°C. The helices for such quenches are shown respectively in Figures 5.5(a) and (b). However, a sharp maximum in the overall density of the helices was obtained for specimens quenched to 70°C.

The observed helices in pure aluminium were found to be always segmented and, in contrast with the results of Thomas and Washburn (1963), were very stable in the thin foils. This difference is not due to the fact that thicker foils were observed at 200 kV in the present work since the helices were found to be quite stable even in the thin regions of the foils.

Angular helices have been reported by Eikum and Thomas (1963) in quenched Al - 5% Mg specimens given a prolonged anneal at 100°C or a short anneal at 183°C. They attribute this observation of the angular helices to a transformation from the circular form during the anneal. Annealing experiments were done by Dr. R.L. Segall to investigate the

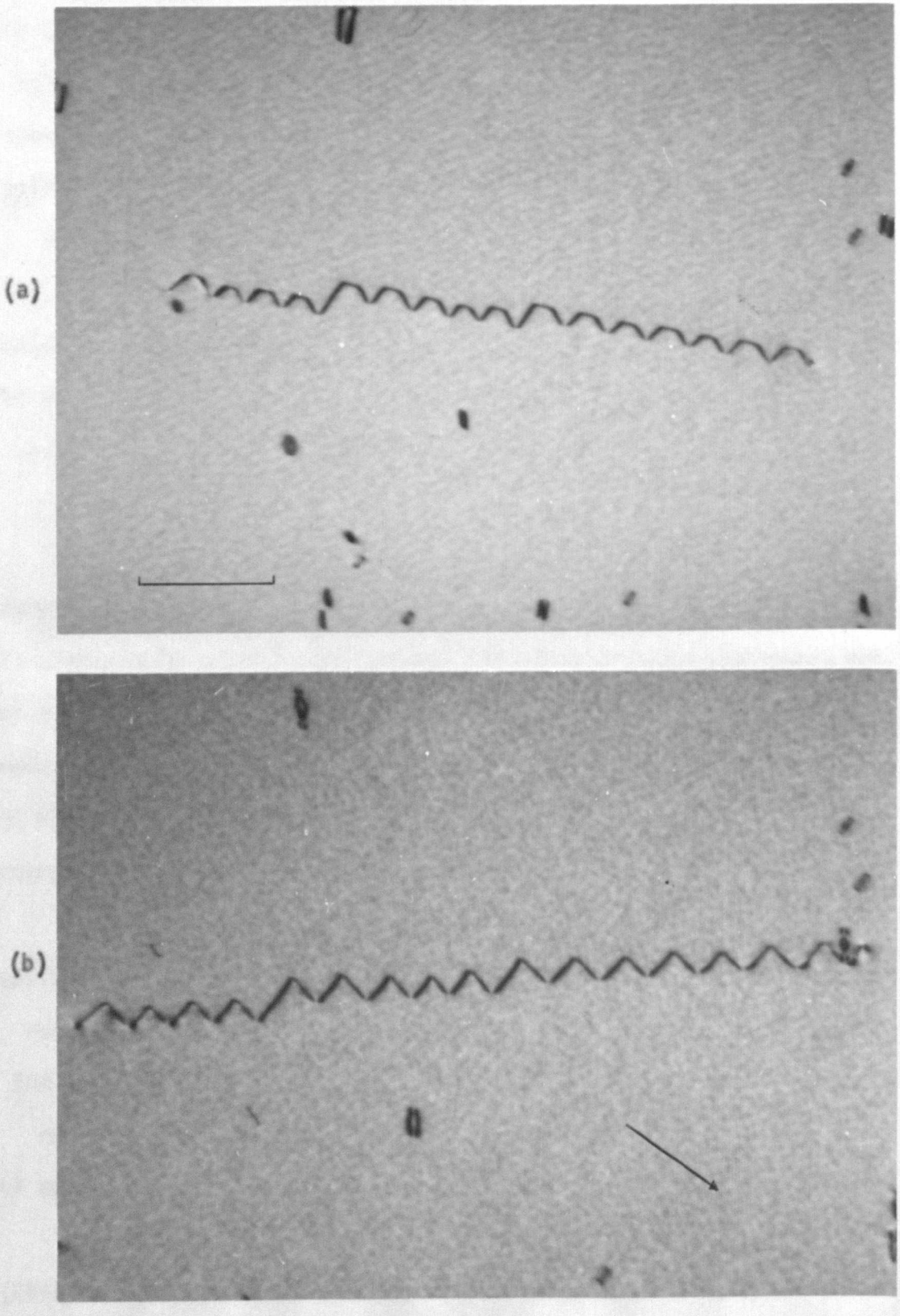

Figure 5.7. A 3 μm long, 16 turn, segmented helix in aluminium quenched to 70°C. Note the characteristic appearance of the helix in the two projections shown - (a) Beam direction : $[0\bar{1}1]$, and (b) Beam direction : $[101]$.

Foil normal : near $[1\bar{1}2]$; g : $1\bar{1}\bar{1}$; 200 kV.

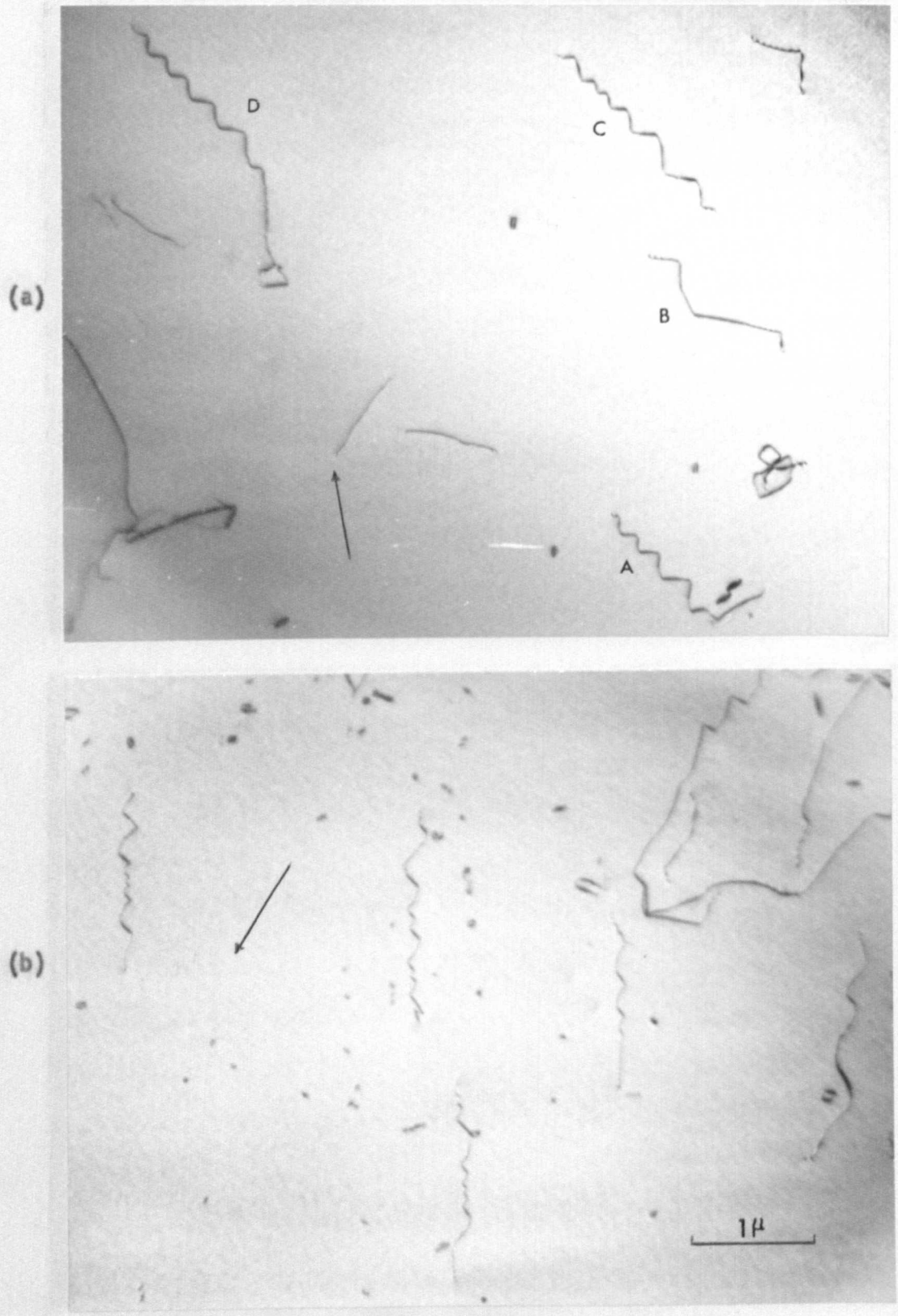

Figure 5.6. Two areas, (a) and (b), of high density of segmented helices along [$\bar{1}01$] in Al 6N quenched down to 70°C.

Foil normal and beam direction : near [$1\bar{1}2$]; $\underline{g}$: $\bar{1}11$; 200 kV.

stability of the segmented helices in aluminium. Thin foil specimens which had been examined in the electron microscope, and a thin sheet specimen known to contain helices, were annealed for 10 min. at 170°C. Electron microscope examination showed that, though the turns intersecting the surface in the thin foils tended to straighten out, the helices in both the thin foils and the sheet specimen retained the segmented form. Thus, as might be expected from the conditions under which they are formed, the angular helices seem to be a minimum energy configuration. Further discussion of this last point is deferred until a later section.

The distribution of the segmented helices in aluminium specimens was quite non-uniform, and there was a tendency for them to occur in groups. The estimated mean density of the helices in a specimen quenched under optimum conditions was 10^9 cm^{-3}, but in some areas of up to 10 μm x 10 μm in extent the density was as high as 2×10^{11} cm^{-3}. Two such areas are shown in Figures 5.6(a) and (b). The observed lengths of the helices were, in general, limited by the foil thickness so no estimate of the mean length can be given. In suitable foil normals helices up to 3 μm long, and containing more than ten turns were observed. One such example of a sixteen turn helix along $[\bar{1}01]$ in a 1 μm thick $(1\bar{1}2)$ foil is shown in Figure 5.7. An upper limit on the observed radius is also imposed by the foil thickness. However helices of 2000 Å radius have been observed as well as helices with a radius as small as 200 Å. In Figure 5.6(a) one turn of a helix of large radius can be seen at B, while the rest of the helix has intersected the surface and is lost. In comparison a number of turns of smaller radii can be seen in this figure in the helices A, C and D, which are along the same direction as B.

One noticeable feature of the observations in aluminium is the large pitch to diameter ratio, i.e. smaller θ, of the helices compared with that of the normal (circular) helices observed in the rich alloys

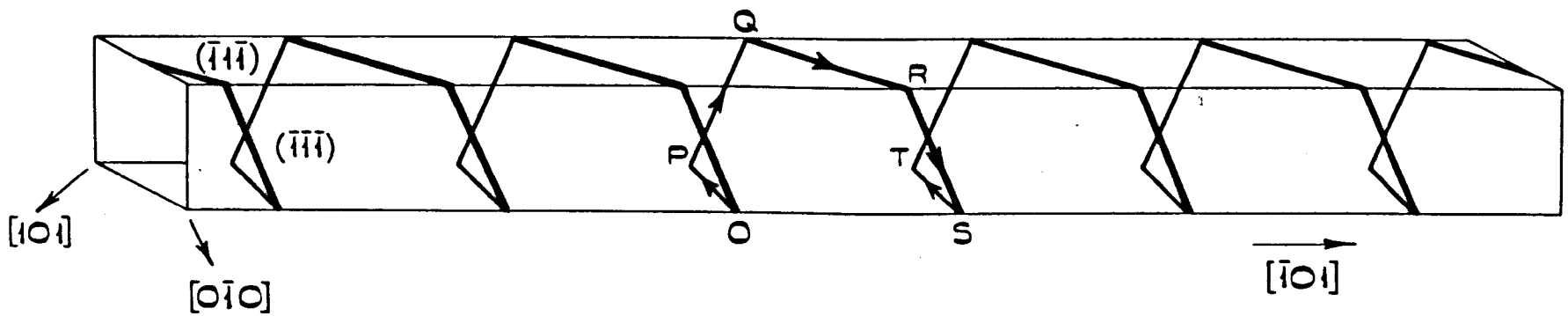

Figure 5.8. Schematic diagram of a segmented helix lying on a prism composed of (111) and $(1\bar{1}1)$ planes.

which are more tightly wound. Pitch to diameter ratios of the helices in pure aluminium were measured to obtain θ, and in the majority of cases this angle was found to be between 40 and 50 degrees, although values of θ as small as 25° and up to 60° were observed. These results are in agreement with the results obtained, in a smaller sample by the direct method of determining the segment directions. The values of θ for a number of helices with their axes along $[\bar{1}01]$ are given in Table 5.2.

5.4. Geometrical Features of Segmented Helices

The geometry of the helices observed in aluminium will now be described in some detail. It will be shown that :

(i) the helices are generally segmented helices in the strict sense defined previously, or are very near to this configuration ; and

(ii) these helices lie on a particular well-defined prism.

More specifically, it will be shown that the observed helices have the configuration illustrated in the line diagram, Figure 5.8. Each turn of this helix consists of four segments and the repetition of each turn is very faithful, i.e. segment OP is strictly parallel to segment ST and so on. The segments of the helix make the same angle with the helix axis, which is also the Burgers vector, and lie on the {111} prism containing this direction. The direction of the helix axis is taken here, and in the rest of this chapter, to be $|\bar{1}01|$, so the helix lies on the prism formed by (111) and $(1\bar{1}1)$.

The above statements were easily verified for several helices from the micrographs of each helix taken in different orientations (and in different reflections for Burgers vector determination). Figures 5.9(a) - (d), together with Figure 5.6(a), show one such set of pictures taken in widely different electron beam directions :

(c)

(d)

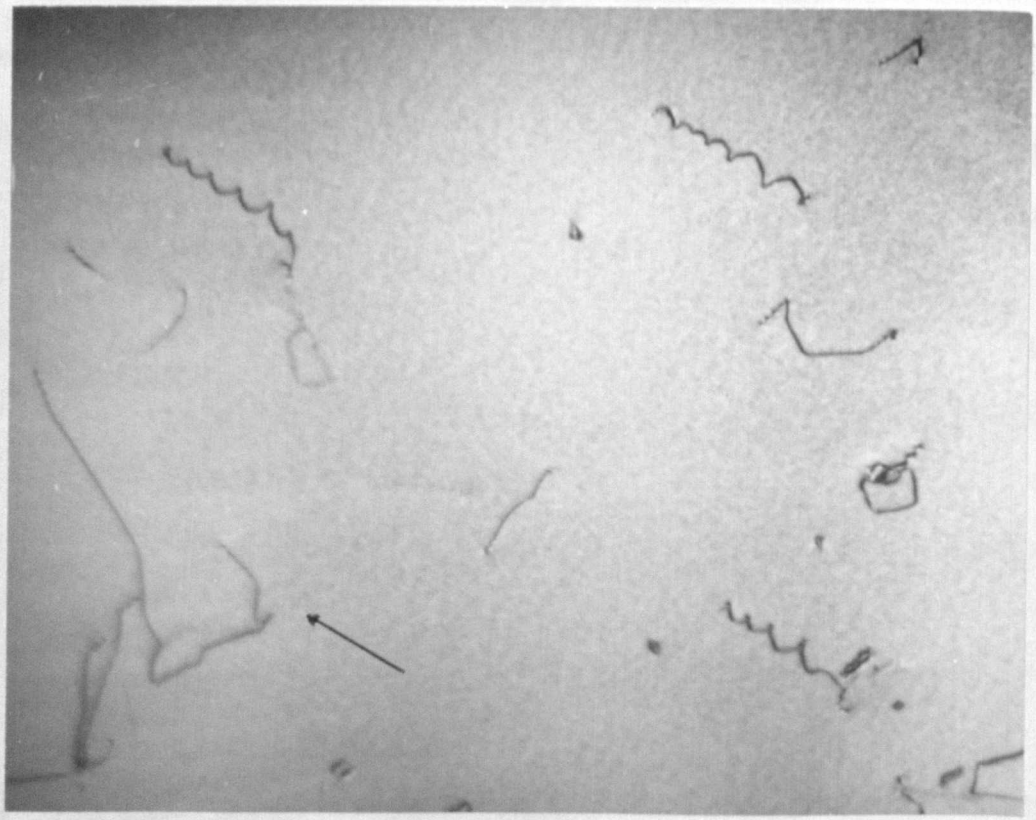

Figure 5.9. (continued)

(c) Beam direction : $[1\bar{1}1]$; $\underline{g}$: $0\bar{2}\bar{2}$

(d) Beam direction : $[001]$; $\underline{g}$: $\bar{2}00$

Foil normal : near $[1\bar{1}2]$; 200 kV.

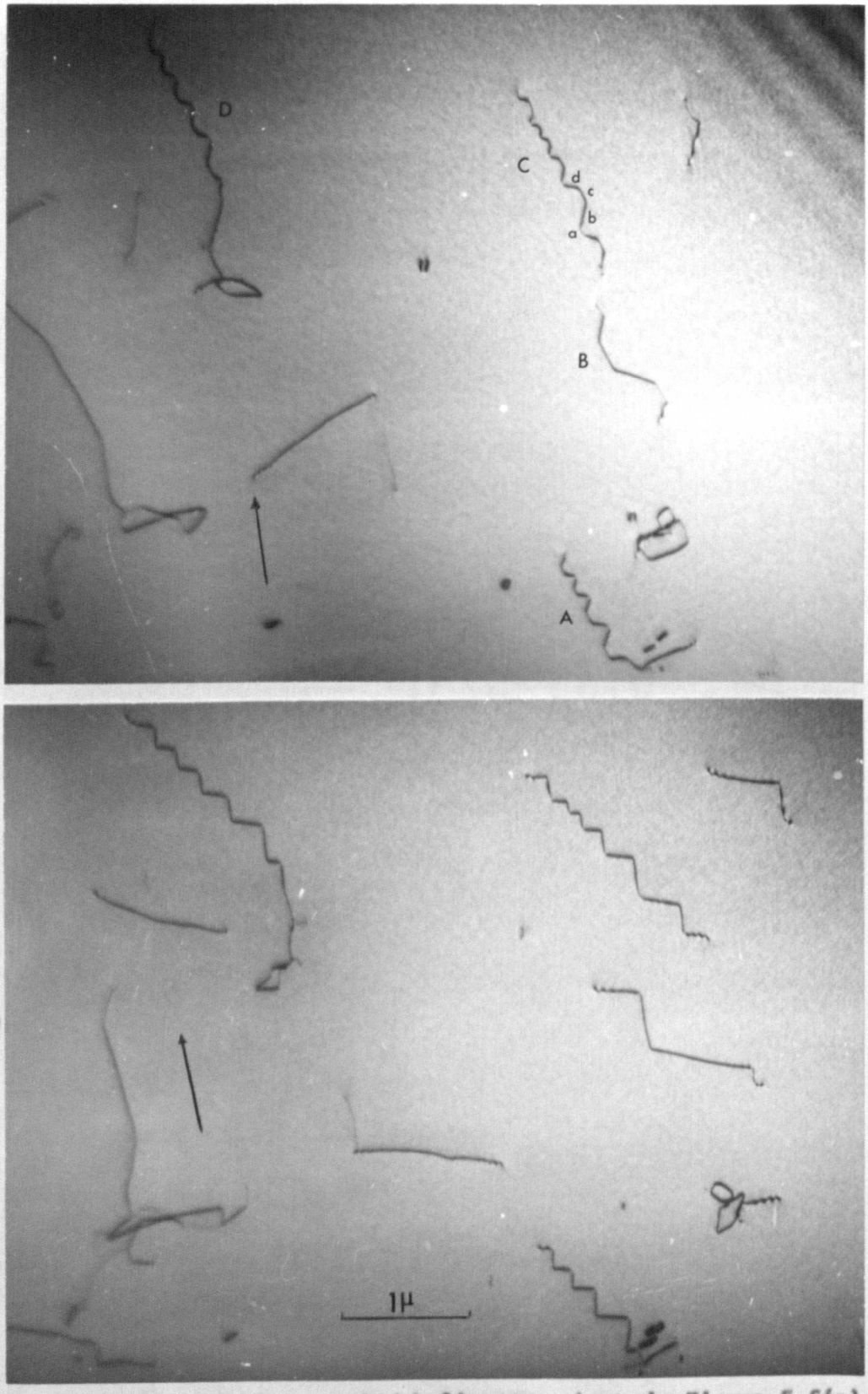

Figure 5.9. The same set of segmented helices as shown in Figure 5.6(a) pictured in four widely separated beam directions :

(a) Beam direction : $[0\bar{1}1]$; $\underline{g}$: $\bar{1}11$

(b) Beam direction : $[101]$; $\underline{g}$: $\bar{1}11$

(continued)

$[0\bar{1}1]$, $[101]$, $[1\bar{1}1]$, $[001]$ and $[1\bar{1}2]$ respectively. While the significance of the particular projection of the helices in Figures 5.9(a) and (b) is discussed below, Figure 5.9(c) is also of special interest as one is looking down on the $(1\bar{1}1)$ plane which contains segments b and d, of helix C say, and forms one set of faces of the prism on which the helices lie. The actual orientations of the segments, and hence the plane on which they lie and the angle they make with the helix axis, was worked out by plotting the projections on a stereographic net. The data obtained from such sets of micrographs is tabulated in Table 5.2. for a number of helices, giving the segment orientations, the planes on which they lie, and the angle, θ, they make with the helix axis or the Burgers vector. The general pattern that emerges from this table is that the segments of the helices make nearly the same angle with the helix axis, and also lie alternately on, or nearly on, (111) and $(1\bar{1}1)$ planes. Micrographs taken in different reflections show that the direction of the Burgers vector of the helices is along their axis. Thus the observed helices have been found to conform to the configuration proposed earlier on in this section.

The method of analysis described above, i.e. finding the actual orientation of the segments in each case, has its drawbacks. The process of measuring angles between various projected directions and plotting them stereographically is time consuming. In addition, the short lengths (generally < 2,000 Å) of the segments make accurate orientation determination very difficult. This is particularly marked because the segments do not lie along any low index direction in general; indeed the segments of different helices do not have a particular crystallographic direction, however irrational, in common. This was found to be true for most of the ten helices examined in detail by this method and can be verified easily from Table 5.2. Figure 5.10 shows the stereographic plot, for five different orientations, of helix C in Figures 5.6(a) and 5.9(a) - (d) and illustrates the scatter in the various projections.

The verification of the two essential properties of the helices in aluminium, that is they lie on a (111) $(1\bar{1}1)$ prism and that they are

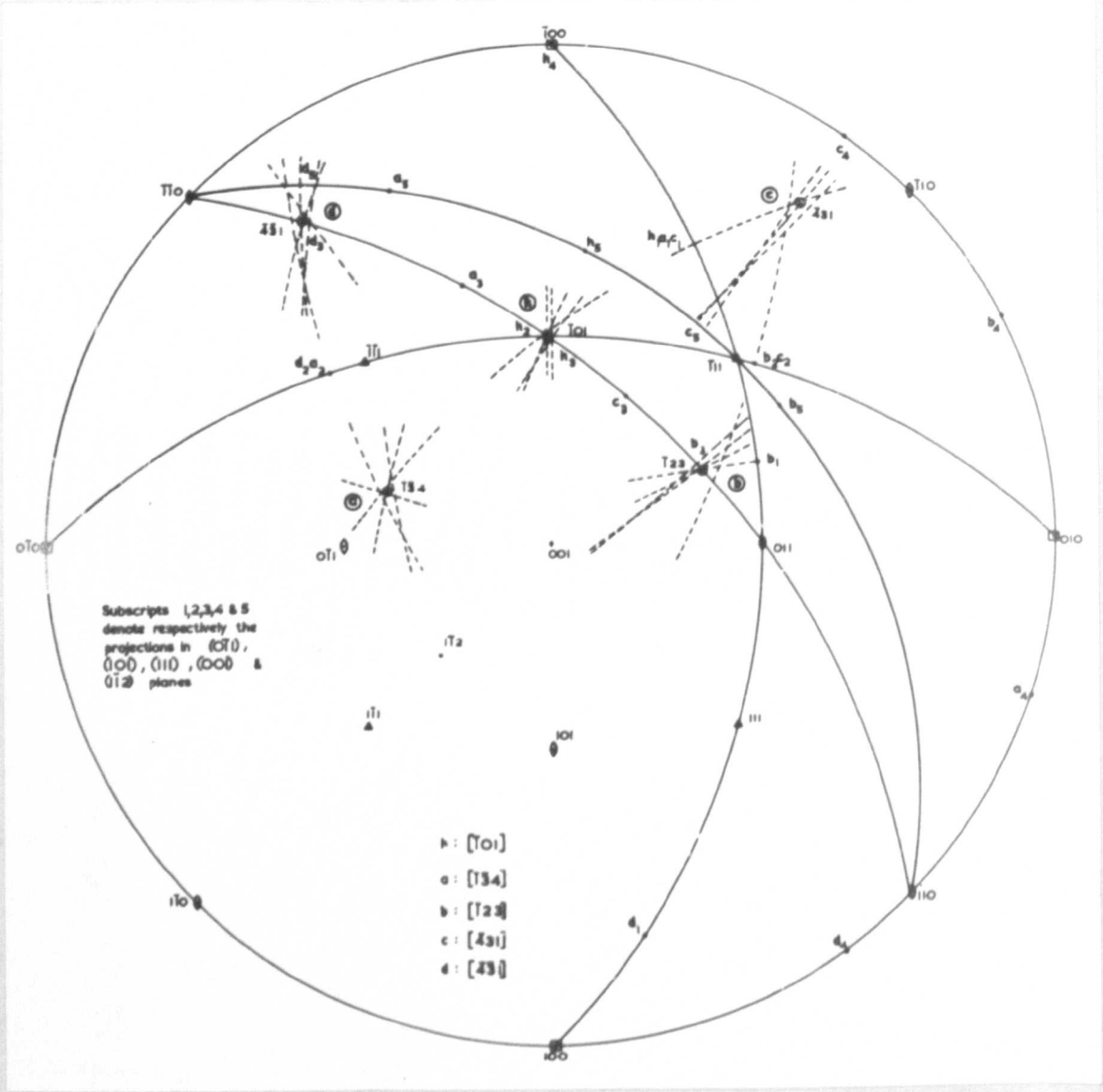

Figure 5.10. An example of the analysis of segment orientations, by plotting stereographic projections, for the helix C in Figures 5.6(a) and 5.9. h is the direction of the helix and a, b, c, d that of the segments as marked in Figure 5.9.

Table 5.2. Segment Orientations of the Helices in Aluminium

(The axis of the helices is taken to be along $[\bar{1}01]$.)

Figure	Helix	Orientation of the segments	Angle between the segment directions and the helix axis, θ	Glide plane of the segments
5.6(a)		$[\bar{1}\bar{2}3]$	41^0	(111)
and	B	$[\bar{1}23]$	41^0	$(1\bar{1}1)$
5.9		near $[\bar{5}32]$	38^0	(111)
		$[5\bar{3}2]$	37^0	$(1\bar{1}1)$
5.6(a)		$[\bar{1}\bar{3}4]$	46^0	(111)
and	C	$[\bar{1}23]$	41^0	$(1\bar{1}1)$
5.9		$[\bar{4}31]$	46^0	(111)
		$[\bar{4}\bar{3}1]$	46^0	$(1\bar{1}1)$
		near $[0\bar{1}1]$	55^0	(111)
5.7	-	$[\bar{1}44]$	52^0	-
		near $[\bar{5}41]$	51^0	(111)
		near $[\bar{1}\bar{1}0]$	55^0	$(1\bar{1}1)$
		$[\bar{1}\bar{4}5]$	50^0	(111)
5.11	A	$[\bar{1}45]$	50^0	$(1\bar{1}1)$
		$[\bar{1}10]$	60^0	(111)
		near $[\bar{1}\bar{1}0]$	57^0	$(1\bar{1}1)$
		$[\bar{1}\bar{3}4]$	46^0	(111)
-	-	$[\bar{2}45]$	42^0	-
		$[\bar{7}52]$	44^0	(111)
		$[\bar{4}\bar{3}1]$	46^0	$(1\bar{1}1)$
		near $[\bar{1}\bar{1}2]$	29^0	(111)
-	-	$[\bar{1}12]$	30^0	$(1\bar{1}1)$
		near $[\bar{2}11]$	32^0	(111)
		$[\bar{6}\bar{2}3]$	25^0	-

Figure 5.11. Segmented helices, A and B, along $[\bar{1}01]$ in pure aluminium viewed along two characteristic directions. Note the particular appearance of the helices in the two projections : (a) Beam direction : $[\bar{1}\bar{1}0]$, and (b) Beam direction : $[0\bar{1}0]$. Foil normal : near $[\bar{1}\bar{3}1]$; $\underline{g}$: 002; 200 kV.

geodesics on this prism, does not in fact require the determination of the orientation of various segments. The two facts are readily proved by a different approach, described below, where accurate qualitative information is obtained.

To demonstrate that the helices lie on the proposed prism is not difficult, for if this is the case then the helix axis and any two alternate segments lie in (111) or (1$\bar{1}$1). Thus if the helix is viewed along a direction contained in either of these planes, the projection consists of four segments, with two alternate segments parallel to one another and to the projection of the helix axis. (For a helix lying at a shallow angle in the foil one of these latter projected segments may be very short). Typical projections of this type are shown in Figures 5.7(a), 5.9(a) and 5.11(a). The direction of the helix axis in these cases is [$\bar{1}$01] while the beam direction is along [0$\bar{1}$1] in the first two figures and along [$\bar{1}\bar{1}$0] in the last. The segments a and c in the helix C in Figure 5.9(a), say, which are along [$\bar{1}$34] and [$\bar{4}$31] appear parallel to the projected helix axis. This is because the beam direction, the helix axis and the segments a and c all lie in (111). Similarly, if this helix were viewed in a direction in the (1$\bar{1}$1) plane, the helix axis and segments b and d, which are along [$\bar{1}$23] and [$\bar{4}$31] respectively, would project parallel to each other. These observations can be extended to other helices in this figure and in Figures 5.7(a) and 5.11(a).

The proof, along the same lines, that the dislocation segments lie on geodesics on the prism is not quite as obvious. Electron microscope observations have to be considered together with a simple vectorial derivation based on the helix geometry. It will be proved that if a geodesic on a rhombus based right prism is viewed along either of the perpendicular bisectors of the angle between the faces the projection consists of only two distinct directions.

Consider two vectors on the adjacent faces a right prism with

a rhombus cross-section, e.g. $\underline{OP}$ and $\underline{PQ}$ in Figure 5.8. Further, these vectors are equal in magnitude and make equal angles with the generator, $\underline{b}$, of the prism, that is :

$$OP = PQ \qquad \ldots\ldots (5.1)$$

and, $$\underline{b} \cdot \underline{OP} = \underline{b} \cdot \underline{PQ} \qquad \ldots\ldots (5.2)$$

It will simply be shown that the vectors $\underline{OP}$ and $\underline{PQ}$ and the perpendicular bisector of the angle between the planes on which they lie are coplanar.

A vector along the perpendicular bisector of the planes containing $\underline{OP}$ and $\underline{PQ}$ is :

$$\underline{n} = (\underline{OP} \times \underline{b}) + (\underline{PQ} \times \underline{b})$$

Hence it must be shown that :

$$\underline{n} \cdot \underline{OP} \times \underline{PQ} = 0$$

Now, $$\underline{n} \cdot \underline{OP} \times \underline{PQ} = (\underline{OP} \times \underline{b}) \cdot (\underline{OP} \times \underline{PQ}) + (\underline{PQ} \times \underline{b}) \cdot (\underline{OP} \times \underline{PQ})$$

$$= (\underline{b} \cdot \underline{PQ})(\underline{OP})^2 - (\underline{b} \cdot \underline{OP})(\underline{OP} \cdot \underline{PQ})$$

$$+ (\underline{b} \cdot \underline{PQ})(\underline{OP} \cdot \underline{PQ}) - (\underline{b} \cdot \underline{OP})(\underline{PQ})^2$$

$$= 0$$

from equations (5.1) and (5.2).

The particular prism used in the present description is made up of (111) and ($1\bar{1}1$) planes which have [101] and [010] as the perpendicular bisectors. Thus if the observed helices are geodesics on this prism and are viewed along either of these directions there should be only two distinct directions of projection of the segments. That this is so is illustrated in Figures 5.7(b) and 5.9(b), where the beam direction is [101], and in Figure 5.11(b), where the beam direction is [$0\bar{1}0$].

It has been shown above that the helices in aluminium are geodesics on the prism formed by the (111) planes containing the Burgers vector direction. However it should be emphasized that there are departures

from these generalizations. As can be seen from Table 5.2, the segments do not always lie precisely on {111}, nor are all segments always equally inclined to the helix axis. Changes in pitch and radius also occur sometimes along the length of one helix, i.e. though the successive turns remain truly parallel the size of the prism changes. This can be seen for helix C in Figure 5.6(a) and for the helices in Figure 5.6(b). Both these deviations from the ideal geometry indicate that in these cases either there were local variations in the vacancy supersaturation due to competing sinks, or perhaps the helices 'froze' in the process of attaining a local equilibrium.

Finally it is convenient here to complete the description of the experimental observations by briefly discussing the geometry of the helices observed by Forty (1960, 1961) in lead iodide. Forty describes zig-zag dislocations whose projection in the basal plane is along the $\langle 1\bar{2}10\rangle$ directions. The crystals studied were basal plane platelets and could be viewed only in the [0001] direction. The zig-zag, i.e. two-segment, appearance of the helices has been ascribed (Forty 1961) to the existence of long segments in the basal plane alternating with short segments in a pyramidal plane. This non-symmetric shape of the helices was attributed to the anisotropy of glide and climb processes in the basal and pyramidal planes. However, due to the observation of exactly similar zig-zag appearance of helices of equal-length segments in aluminium when viewed along certain directions, this explanation is now difficult to sustain. A more likely explanation is that the helices in lead iodide are geodesics on a rhombus based right prism made up from $(10\bar{1}n)$ pyramidal planes, with the helix axis along $\langle 1\bar{2}10\rangle$, which is a probable direction for the Burgers vector. The [0001] direction is of course a diagonal of this rhombus, and hence, as discussed above, a projection in this direction consists of only two segments. The observations of the cusps and chains of loops at the corners of the helices in lead iodide are however still not amenable to a satisfactory

explanation, though, like Forty (1961), interaction between adjacent segments could again be invoked. The observation of the segmented helices in lead iodide is of interest here for two reasons. Firstly, it refers to a non-cubic structure, and secondly, the helices were actually seen to develop in the electron microscope.

5.5. Origin of Segmented Helices

The experimental conditions for the formation of helices suggest that they are produced only when there are few other vacancy sinks available to compete with the screw dislocations. In many of the aluminium alloys, for example, self-sink nucleation is inhibited by vacancy trapping and the helices are a major vacancy sink, becoming tightly wound. Thus in normal quenches of pure aluminium to room temperature or below few helices are observed due to the presence of a high density of loops and/or voids. It has been shown in Section 5.3. that helices are formed reproducibly in aluminium only when it is quenched to a higher temperature (≈ 70°C). In such a quench few self-sinks are nucleated as can be seen from the fact that few loops are observed. The critical value of this temperature for maximum helix density presumably arises from a balance, as the quench temperature is raised, between the decreasing probability of self-sink nucleation and the increasing vacancy loss to infinite sinks.

Another factor favouring helix formation in the conditions where the specimen is quenched to a temperature somewhat above room temperature is that the screw dislocations are rapidly converted into helices before they can cross-slip and annihilate one another during deformation. This rapid conversion of the screws into helices in the presence of quenched-in vacancies occurs partly because of the absence of competing sinks but also partly because of the increased mobility of the vacancies at the higher temperature (e.g. the mobility of vacancies in aluminium at 70°C is about 180 times that at 0°C, assuming a vacancy migration energy of

0.60 eV (Doyama and Koehler 1964)). The fact that helices are observed only when the screw dislocations are produced simultaneously with the vacancy supersaturation which can immobilize them in the form of helices provides direct evidence of the annihilation of screws in aluminium deformed at room temperature and above.

There are two factors which could account for the non-occurrence of helices in aluminium quenched conventionally. One is that in such quenches the specimens are generally deformed after the quench and considerable nucleation of self-sinks could already have taken place before the screw dislocations are generated (e.g. the nucleation time in Al at 30°C : for loops = 1 sec., for voids = 0.1 sec. (Kiritani et al 1966b)). The second, and the more important, reason is that these specimens are usually quenched down to room temperature or below, while it is known (Kiritani 1965) that nucleation of self-sinks rapidly increases with a decrease in this temperature. The helices observed under the most favourable quenching conditions, described in Section 5.3., have small values of θ, i.e. a large pitch to diameter ratio. The effect of the competing sinks will be to make θ even smaller in the helices which do form in quenches to low temperatures. Helices of very large pitch to diameter ratio are not readily recognized as such in thin foils. Thus the sharpness of the maximum in the curve of measured helix density versus temperature of the quenching bath will be enhanced by this effect.

Comparison of density, pitch and radius between the circular helices in rich aluminium alloys and the segmented helices in Al - 0.5% Mg and zone-refined aluminium shows that considerably less vacancies are annihilated at helices in the latter case. This is of course due to the fact that in this case helices are not the only sinks for vacancies. Thus angular helices are observed when the flux of vacancies to the helices is comparatively small, and hence segmented helices could presumably be associated with low climb force. This hypothesis is

consistent with the electron microscope observation of angular helices in PbI_2 by Forty (1960, 1961). These were observed in the early stages of disintegration of the crystal in the electron beam and are attributed to the climb of dislocations caused by the vacancies generated thermally due to beam heating. Thus the flux of vacancies, though continuous in time, is expected to be low.

Helices have previously been observed in X-ray topographs of well annealed, slowly furnace cooled, crystals of high purity aluminium (Lang and Meyrick 1959; Authier et al 1965; Nøst et al 1967) and molybdenum (Becker and Pegel 1969). This observation is in accord with the present suggestions about the conditions for helix formation since the supersaturation in these experiments is low and consequently no competing sinks will be nucleated and the surface, the major infinite sink, is very remote. It is not possible to see from the published X-ray topographs of aluminium whether the helices are segmented or not. However on the basis of low vacancy flux argument given above these helices could be predicted to be segmented. In fact one of the helices shown in Figure 3 of Becker and Pegel (1969) does seem to be somewhat angular.

Strudel and Washburn (1964) have observed the formation, in the electron microscope, of few turns of an angular helix in quenched Al specimen by the interaction of a moving screw dislocation with faulted loops not on either of its glide planes. However, only a few turns of the helix can be formed in this way, as after this the motion of the dislocation is arrested, and these few turns are going to be irregular due to the non-uniform distribution of the loops. Furthermore, all the segments of such a helix would not lie on a glide prism. It is thus clear from the observation of the great length, the large number of turns, the regularity of the helices which are on the glide prism, and from the sparseness of dislocation loops, that the helices in the present case were formed by the direct addition of vacancies to screw dislocations.

and not by the interaction of screw dislocations with the existing loops.

The significance of the geometrical form of the helices in aluminium will now be considered in detail. General expressions for the energy of circular helices have been derived by de Wit (1959, 1960) which can be simplified in the limiting cases of tight winding or loose winding. Grilhe (1964, 1966) has computed these energies over a continuous range of pitch. These computations of a particular helix of ten turns showed a minimum in the energy at $\theta = \cot^{-1} 0.45$, i.e. $\theta = 66^{\circ}$. This is, as pointed out by de Wit (1959), of course the result of a compromise between the dislocation line energy and the interaction energy between different turns of the helix. The increase in energy at larger values of θ (i.e. smaller pitch to diameter ratio) corresponds to an increase in the repulsive energy between successive turns, while that at smaller values of θ is due to an increase in line length and consequently the dislocation line energy.

Approximate line energy calculations were done for a segmented helix of pitch θ on a (111) prism, using the expression (Cottrell 1953b)

$$E = \frac{Gb^2}{4\pi(1-\nu)} (1 - \nu \cos^2\theta) \ln \frac{r}{r_0}$$

where E is the energy per unit line length,

θ the angle between the Burgers vector and the dislocation line,

r the outer cut-off radius, taken as half-pitch,

and G, ν, b and r_0 have the usual meaning.

For comparison with the results of Grilhe for the circular helix, the segmented helix was constrained to a prism with the same projected area perpendicular to $\underline{b}$ as the glide cylinder of the circular helix. This comparison is however only approximate, as the computations of Grilhe include the interaction between the turns at small pitch to diameter ratio which the present calculations do not. As expected,

the energy per turn of the segmented helix shows a continuous increase with decreasing θ (i.e. increasing pitch to diameter ratio). An increase in energy at large θ (i.e. small pitch to diameter ratio) is also expected to occur if additional terms for interaction between the turns could be incorporated. In any case, the energy per turn of the segmented helix exceeds that of the circular helix for θ smaller than $\cot^{-1} 0.3$, i.e. for $\theta < 73^{\circ}$. This is due to the fact that, for a given number of absorbed vacancies and a given pitch, the circular helix has lesser line length than any segmented helix. Experimental observations have on the other hand shown a large number of helices in aluminium with θ as small as $\cot^{-1} 0.9$ (i.e. between 45 and 50 degrees). Thus, in general, on line energy grounds, the energy of the segmented helices is considerably higher than that of the circular helices formed to eliminate the same vacancy supersaturation.

A number of reasons could account for the preferential formation of segmented helices even though their line energy is higher. It could be that the segmented helices observed in the present work form as a direct consequence of the difficulty of jog nucleation. This argument is tenable on the grounds of low climb force resulting from the particular quenching conditions, and a somewhat similar argument has been used by Bontinck (1957) to explain the polygonized features of some of his helices. A circular helix has to be highly jogged (like the circular loop of Silcox and Whelan 1960) and thus requires a higher climb force for formation, while a segmented helix lying on a prism of {111} planes containing the Burgers vector need only be kinked. However evidence contrary to this hypothesis is provided by the fact that the helices invariably retain their segmented configuration during high temperature annealing where the opportunity exists for reversion to a lower energy form, if there is one.

There are two likely explanations for the occurrence of the observed segmented helices on the more reasonable assumption that this is a minimum

energy configuration with respect to other possible dislocation configurations, such as the circular helix. One possibility is that the interaction energy between different parts of the helix may be diminished in the segmented form. Alternatively, the core energy contribution of each turn of the helix may be significantly reduced when it is segmented in a way that the segments lie on the {111} planes containing the Burgers vector. It is also likely that both these factors jointly determine the exact helix geometry.

Bullough and Foreman (1964) and Bacon and Crocker (1966) have calculated the energy of rhombus shaped loops on a {111} glide prism to explain their observation in pure aluminium and Al - 1% Mg (Makin and Hudson 1963; Hudson and Makin 1965). They have shown that, due to the interaction between straight segments (Bacon 1966), such loops have a low energy position near a particular orientation away from pure edge orientation. If similar arguments could be made for a segmented helix on a {111} prism, minimum interaction energy configuration may be possible for a particular value of θ. However, difficulty immediately arises from the fact that stable segmented helices are observed for values of θ spread over a large range. A comparison of the energies of rhombus shaped loops, calculated by Bacon and Crocker (1966), and of circular loops, calculated by Bacon (1966), can also be made. This comparison for minimum energy loops on a {111} prism and on a cylinder of equal cross-sectional area shows that, except at extremely small radii, the latter have a lower energy. Of course the calculations for dislocation loops cannot directly be extended to helices, but they do suggest that if interaction energy were the only criterion, the circular helix would be favoured. Furthermore, the computations of Grilhe (1964, 1966), and also the general analysis of de Wit (1959, 1960), show that the interaction energy term is predominant only at small pitch, i.e. for $\theta \geq \cot^{-1} 0.4$. The observed helices are found to have a large pitch, around $\theta = \cot^{-1} 0.9$, and hence the influence of interaction between different turns in such cases is

expected to be very small.

With the above reservations about the interaction energy, the most plausible explanation for the occurrence of segmented helices lies in the lower core energy of this configuration, as the segments lie in the {111} planes containing the Burgers vector. This is consistent with the fact that these helices form under conditions of low climb force and are thus likely to be a lower energy form. The only way this could be possible despite the larger line length, in comparison with that of a circular helix, is by a reduction in the core energy of the dislocation line. Indeed the calculations of core energy have been made on the tacit assumption that it is lowest in the glide plane. It is then logical that the helices should be geodesics on the observed prism since for a given pitch this will be the minimum line length configuration. The growth of the helices presumably takes place by the nucleation of jogs at the corners, where it is easy to do so (Silcox and Whelan 1960), which then propagate along the straight segments.

If this hypothesis is correct then the observation that circular helices are often observed in aluminium alloys requires explanation. As revealed by the comparatively tight winding of these helices they result as a consequence of the absorption of a large number of vacancies. Thus the high vacancy flux in this case may mean that the climb force is sufficient to overcome the constraint arising from the lowering of the core energy on the {111} planes containing $\underline{b}$, i.e. on the glide planes. An alternative description of the same phenomenon may be given on the basis of jog nucleation. When the supersaturation is sufficient jogs can be nucleated anywhere along the length of the dislocation line rather than only at the corners. To accommodate a large number of vacancies in the shortest possible time, the climb of all these jogs may take place giving a circular helix.

If the core energy criterion is solely responsible for the segmented configuration of the helices observed in aluminium, it provides a means

for estimating the reduction in the core energy when a dislocation lies in its (111) glide plane. Now for a helix with a given θ, the line length per turn of the segmented helix is $(3\sqrt{2}/\pi)^{\frac{1}{2}}$ times that of the circular helix which has absorbed an equal number of vacancies, i.e. the segmented helix is 16% longer. Thus a reduction in the core energy in case of the segmented helix must account for the increase in line energy due to the increased length. There are no reliable calculations of core energy but it is generally assumed to be between 10 and 20% of the elastic energy of a straight dislocation (Weertman and Weertman 1964b). A 16% difference in total energy per unit length is a large difference to attribute to the change in core energy between a dislocation either lying in its glide plane or not. However, the fraction of the total energy per unit length contributed by the core will be greater in a helical dislocation than in a straight screw, as the elastic energy per unit length of the helix will be less due to interaction between successive turns (de Wit 1959). The ratio, r, of the core energies for a dislocation when it is not on its glide plane and when it is on it can be easily calculated from the fact that the segmented helix is 1.16 times as long as the equivalent circular helix. It will be assumed that the interaction energy per turn is the same for the segmented and circular helices and that the segmented form is only marginally favoured. Then, if E is the elastic energy per unit line length of a helical dislocation, and f the fraction of E that the core contributes per unit length in the case of a dislocation on its glide plane,

$$(1 + rf)E = 1.16\,(1 + f)E$$

$$\text{or} \qquad r = 1.16 + \frac{0.16}{f}$$

The ratios r can be evaluated for various values of f and some of the results are given in Table 5.3. On the basis of the discussion given above, the core energy of a segmented helical dislocation probably lies

Table 5.3. The ratio r of core energies for a dislocation, when it is off or on its glide plane, for varying fractional core contribution f to the elastic energy

Core contribution f	Ratio of core energies r
0.10	2.76
0.15	2.23
0.20	1.96
0.30	1.69
0.40	1.56
0.50	1.48

between 40% and 15% of the elastic energy. These limits lead to the values of r respectively between 1.6 and 2.2. It is of course possible that r may be greater than 2.2 since the segmented helix could have appreciably lower energy than the circular form, rather than having just marginally lower energy.

5.6. Conclusions

The experimental conditions favourable to the formation of helices in zone-refined aluminium have been described. These were a fast quench from near the melting point to a temperature ≈ 70°C with the specimen being deformed during the quench. The former condition ensures that only a minimal number of competing self-sinks are nucleated while maintaining an adequate supersaturation for the climb of screw dislocations. The latter prevents the mutual annihilation by cross-slip of the screws during plastic deformation, by making them climb into helices immediately after formation.

The geometrical features of the helices observed in pure aluminium

and Al - 0.5wt.% Mg have been described in detail. These helices were composed of straight segments lying on the prism formed by the {111} planes containing the helix axis, which was along the Burgers vector direction. In most cases the segments were of nearly equal length and made nearly the same angle with the helix axis, i.e. the helices were geodesics on the {111} prism. These segments however did not in general lie along any particular low index direction.

The preferential formation of segmented helices as compared to circular helices was attributed to their being a lower energy form. This minimum energy configuration of the segmented helices, despite their comparatively longer line length, was ascribed to the reduction in the core energy of a dislocation line when it lies in the {111} plane containing its Burgers vector. The ratio, r, of the core energy of a dislocation when it is off its glide plane and when it is on it was then derived to be $1.6 \leq r \leq 2.2$.

CHAPTER SIX

RADIATION DAMAGE IN THE 200 kV ELECTRON MICROSCOPE

6.1. Introduction

The scattering of incident electrons in an electron microscope can for many purposes be treated as elastic but considerable inelastic scattering occurs when the electron imparts some of its energy to the specimen. This energy transfer occurs in a metal primarily by the interaction of the incident electron with phonons, plasmons and single electrons. Another mode of energy transfer, which is of little importance in the conventional 100 kV electron microscopes, is the direct collision of the atoms of the specimen with the impinging electron. This process is of considerable interest during high voltage microscopy where such a collision can result in the atoms of the specimen being knocked out of the normal lattice positions. Due to the high electron flux attainable in an electron microscope ($\simeq 10^{19}$ electrons cm^{-2} sec^{-1}), which is over three orders of magnitude higher than in a conventional accelerator, the damage so produced can be large. Indeed, 100 kV (Venables and Lye 1969) and 600 kV (Makin 1968a, 1968b; Ipohorski and Spring 1969) electron microscopes have been used to produce and observe radiation damage.

Irradiation effects in solids have been reviewed by a number of authors (Seitz and Koehler 1956; Corbett 1966; Thompson 1969). Electron irradiation damage is easier to investigate than that due to heavier particles as the energy transfer is low and thus conditions can be controlled so that no more than a single displacement per collision is produced. Low temperature electron irradiation of aluminium has been reported by Iseler *et al* (1966), Neely and Bauer (1966), and Simpson and Chaplin (1969), and resistivity measurements have determined the value of the displacement threshold energy as 16 eV. Thus, in principle, it is possible to produce damage in aluminium with electrons of 166 keV

energy, though the damage would be difficult to detect due to the low cross-section.

Interaction of the incident electrons with the specimen under observation in an electron microscope is treated according to the dynamical theory of electron diffraction (Howie and Whelan 1961). To incorporate both the elastic and the inelastic scattering a complex lattice potential is assumed (Yoshioka 1957). In the two beam approximation of the dynamical theory the wave function of the electron is represented by a linear combination of two Bloch waves. One of these waves, conventionally type 1, has its nodes, while the second, type 2, has its antinodes, at the atomic positions (Hashimoto et al 1962). It is thus expected that wave 2, having its maxima at the atomic positions, would have larger interaction with the atomic potential. This is confirmed by an increase in certain forms of inelastic scattering when the electrons are incident such that $w = s\xi_g < 0$, i.e. when mainly type 2 wave is excited. In such a case the specimen exhibits greater absorption and an increased production of X-rays (Hirsch et al 1962; Duncumb 1962, Hall 1966). It has been suggested (Howie 1969) that displacement damage in the specimen might be similarly enhanced.

The present chapter reports some preliminary experiments done to investigate the comparative damage rate in the 200 kV electron microscope in aluminium specimens oriented either for anomalous absorption or anomalous transmission. Section 6.2. describes the technique used for the detection of damage by the annihilation of small dislocation loops introduced by prior quenching, while Section 6.3. describes and discusses the experimental results.

6.2. The Detection of Damage

The technique used to detect the radiation induced damage was based on the annihilation of pre-existing vacancy loops by the interstitials produced. The disappearance of quenched-in stacking-fault

tetrahedra in gold has been reported by Cotterill and Jones (1964) during α-irradiation and by Cotterill (1966) during neutron irradiation. Annihilation of vacancy loops in aluminium during irradiation with 50 keV Ar ions has also been observed (Henriksen et al 1968). On the other hand, Makin (1968b) failed to observe any such effect after prolonged irradiation of quenched aluminium specimens in a 600 kV electron microscope.

The interstitials produced during irradiation, in the electron microscope, of thin aluminium specimens containing vacancy loops can disappear in a number of ways. They can recombine with the vacancies produced simultaneously, migrate to the specimen surface, form interstitial-impurity complexes, or go to the nearest vacancy loop. On the assumptions that the shrinkage of a vacancy loop of radius r is proportional to its perimeter, that other vacancy loops are not competing sinks, and that there is a constant flux of interstitials to the loop, it can easily be shown that dr/dt is constant. Since the ease of detection depends on the fractional change of the loop radius the sensitivity of this method depends inversely on the loop radius. Thus a specimen containing large vacancy loops is not suitable for the sensitive detection of radiation damage, and probably this was the major reason for the negative result obtained by Makin (1968b).

The specimens generally used in the present work contained a high density ($\approx 10^{15}$ cm^{-3}) of very small loops with diameter $\lesssim$ 100 Å. Such a fine distribution of dislocation loops was obtained by quenching thin sheet Al 6N specimens from 630°C to liquid nitrogen through brine at 0°C and then deforming 2% at -195°C, as described in detail in Chapters 3 and 4. During irradiation normal operating conditions, the same as those during observation, i.e. a current of 30 μamp (leakage current as read on the panel), a 200 μm condenser aperture and a 5 μm diameter spot size, were used. The actual electron current was estimated to be about 0.1 μamp, corresponding to a flux of approximately 10^{18} electrons cm^{-2} sec^{-1}. The electron current could be roughly monitored by reading on a Keithley

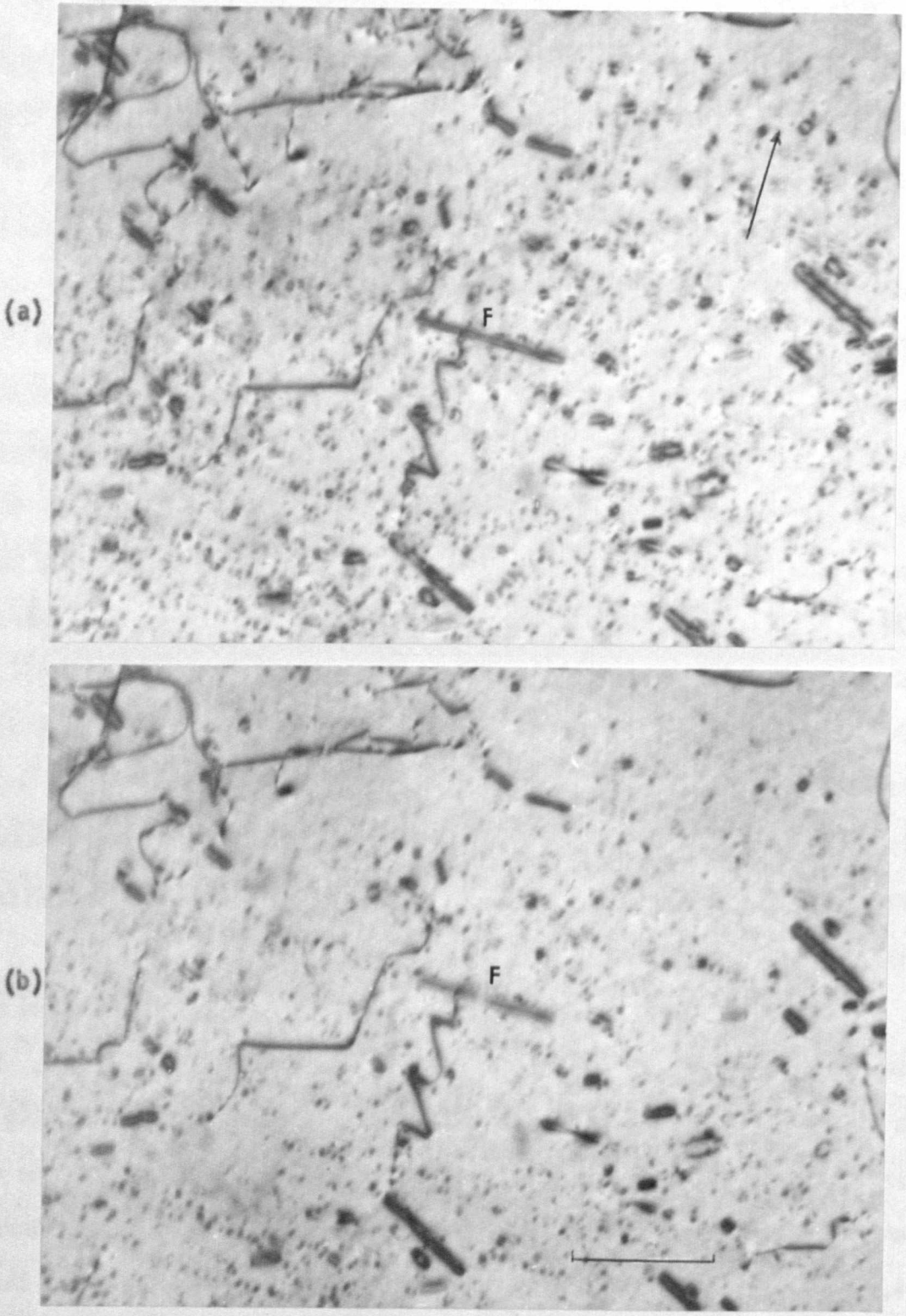

Figure 6.1. An area from quenched and deformed Al 6N showing vacancy loops and a faulted dipole F. Figure (a) is a micrograph taken at the beginning of electron microscope observation, while (b) is taken after 60 min. irradiation in the electron beam with $w > 0$.

Foil normal : $[7\bar{3}\bar{2}]$; Beam direction : $[1\bar{1}0]$; $\underline{g}$: $00\bar{2}$; 200 kV.

602 Electrometer the current intercepted by a small collector which could be swung into the beam path below the projector lens. The electron current was checked every 10 to 15 min. during irradiation and any slight adjustment, if necessary, was made to keep the current constant. Disappearance of dislocation loops during irradiation was taken as evidence of damage, and the damage rate was expressed as the ratio of the number of loops remaining after a certain irradiation time to the initial number.

Unequivocal evidence of radiation damage in aluminium with 200 keV electrons was obtained using this method. The method of detection proved to be quite sensitive and under normal operating conditions damage was detectable in less than 30 min. irradiation. The annihilation of loops during irradiation is clearly illustrated in Figures 6.1(a) and (b) which, respectively, show pictures of the same area taken before and after a 60 min. irradiation. The foil thickness was ≈ 7000 Å and the orientation during irradiation <101> with $w \gtrsim 1.0$. The density of loops in Figure (b) can be seen to be smaller than that in (a), and in fact 30% of the loops have disappeared during irradiation. A faulted dipole in the process of of annealing is also seen at F. Its contrast has grown markedly weaker in (b) and it has split into two.

To end this section it is appropriate to describe the factors which can be adjusted to attain maximum sensitivity, and to list some of the conditions which must be carefully controlled to keep the magnitude of possible errors to a minimum. Usually 111 or 200 type reflections are used during observation of specimens in the electron microscope. Where loop counting is concerned it is better to use a 111 type $\underline{g}$ as the vacancy loops are then either in good contrast or are almost invisible. If a 200 type $\underline{g}$ is used, then under normal observation conditions of large w, the (faulted) loops which have $\underline{g} \cdot \underline{b} = +\frac{2}{3}$ are in strong contrast while those with $\underline{g} \cdot \underline{b} = -\frac{2}{3}$ are in weak contrast. The latter, out of contrast loops, can introduce errors during the counting operation, as slight change

in w can make such loops appear strong or weak.

The procedure for the experiments described in the following section consists of a comparison of damage in two different areas. In order that the same number of interstitials be annihilated at each loop in the two areas, the loops in both these areas must have similar size distribution. This condition can however be easily satisfied as it is not difficult to find areas with loops roughly equal in size. Furthermore, areas containing a very high density, $> 10^{15}$ cm^{-3}, of loops are not suitable for this detection technique as counting is made difficult due to overlapping of the loop images.

To achieve maximum sensitivity irradiation must be performed on areas containing very small loops. Thus good visibility for small defects is a critical condition for the detection of damage. Thin areas are therefore required for these experiments as the definition of the image is much better in such areas. When comparing different micrographs of the same area, taken after different irradiation times, it is necessary to have the exposure nearly the same for all micrographs when taking pictures inside the microscope and during printing of the plates. However, what is most important, when such a comparison is being made, is that all the micrographs must have the same contrast. This is a difficult condition to meet over the whole area of the micrographs as the variation of contrast, specially in thin areas, is different in pictures taken at different times due to changes caused by slight contamination. This difficulty could be overcome by taking a number of pictures at each time with slightly different contrast conditions and subsequently matching areas with the same contrast but photographed at different irradiation times.

Contamination of the specimen is a factor which is not possible to control. Apart from degrading the quality of the micrographs and causing contrast variations, it raises serious worries with regard to

the nucleation of interstitial clusters (Thomas and Balluffi 1967). The temperature of the specimen is another unknown and uncontrolled factor in these experiments. However, due to the good thermal conductivity of aluminium, and the relatively low energy and low current of the electrons, the temperature of the specimen is not expected to be very much above room temperature.

6.3. Damage during Anomalous Absorption

The low transmission when a specimen is viewed in an electron microscope under negative w conditions has been attributed to increased phonon scattering in such a case. The calculations of Hall and Hirsch (1965) and Whelan (1965b) have shown the marked effect of thermal vibrations on Bloch wave 2. This occurs because phonon excitation is enhanced near atomic nuclei where wave 2 is predominant. The incident electrons so scattered result in 'anomalous' absorption mainly by being scattered out of the objective aperture. In contrast, plasmon scattering contributes very little to anomalous absorption as this process affects both waves 1 and 2 more or less equally (Howie 1963).

Another source of inelastic scattering of electrons incident on a specimen in a microscope is the excitation of inner shell electrons of the atoms (Whelan 1965a). This process is obviously expected to occur with greater probability in the vicinity of the atoms and would result in the production of X-rays. This effect should therefore be more pronounced when wave 2 is excited. The enhanced production of X-rays in such a case was first considered by Hirsch *et al* (1962) who calculated a maximum in emission for $w < 0$ and a minimum for $w > 0$ conditions, and the ratio of the maximum to the minimum of nearly 3 : 1. Experimental observation of this effect was made by Duncumb (1962) who detected increased emission of X-rays from dark absorption contours. A more elaborate experimental confirmation has been reported by Hall (1966). The ratio of maximum to minimum X-ray emission has been found to be much

smaller than that predicted theoretically due to diffuse scattering of electrons in the finite thickness of the specimen.

A brief account is given in the following of the experiments performed to detect any enhancement of displacement damage in aluminium specimens when exposed to an electron beam under $w < 0$ conditions in the 200 kV electron microscope. The method used for the observation of damage has been described in the previous section. An area of a specimen containing a uniform density of small loops was irradiated, with a constant electron current, for times up to 180 min. in conditions of maximum absorption. As there are indications that the displacement threshold is higher for electron beam directions near the corners of the stereographic triangle (Makin 1968b), orientations other than these were used for irradiation. Micrographs of the irradiated area were taken at the beginning of the operation and at suitable intervals of time, varying between 5 and 20 min., during the irradiation. Identical experiments were carried out on a similar area in conditions of maximum transmission. The number of dislocation loops was counted in each of the two cases and a comparison was made of the ratios of the number of loops that remained after a certain irradiation time to the initial number of loops.

To detect any difference between the damage rate in a specimen oriented either for anomalous transmission or for anomalous absorption two factors must be taken into account. It is expected that the difference between the two cases would be more marked in case of thin specimens. Hall (1966) has calculated the variation in the ratio of the maximum to minimum emission of X-rays with increasing thickness, for Ni and Ge specimens oriented respectively for maximum absorption or maximum transmission. Spring (1970) has computed the intensity of the incident 600 keV electrons at the atomic sites as a function of depth in Cu specimens. The respective curves in both these cases exhibit a sharp fall in the first few extinction distances and then a gradual decrease

with further increase in thickness. This smearing out of the difference between the effects of wave 1 and wave 2 is ascribed to the randomization of the two waves with increasing thickness, i.e. the scattering of one wave into the other.

The relative excitation of type 1 or type 2 waves is also dependent upon the reciprocal lattice vector $\underline{g}$. As $\underline{g}$ becomes larger the absorption of wave 1 increases and that of wave 2 decreases (Hall and Hirsch 1965). Thus to observe a more marked difference between the effects of the two waves as small a $\underline{g}$ as possible should be used.

The thickness of the areas examined in the present experiments is given in Table 6.1. The number of experiments on very thin areas were restricted due to the difficulty of finding such areas containing an adequate number of loops of the appropriate size. Most of the work was devoted to electron beam direction of <213> and $\bar{1}\bar{1}1$ $\underline{g}$ for irradiation and observation, though some inconclusive experiments were also done in <001>, <103> and <101> orientations. Also, apart from a few irradiations at 175 kV and 220 kV, most of the experiments were performed at an accelerating voltage of 200 kV. Three runs were made for irradiation at 200 kV in the <213> orientation. Each consisted of the irradiation of two different areas of comparable thickness, one under maximum absorption conditions and the other under maximum transmission conditions. Maximum absorption was observed near $w = -2.0$ and maximum transmission near $w = +1.5$.

In view of the possible sources of error enumerated in Section 6.2. and considerable scatter in the counts of the loops, the results of the present experiments are given with reservation. These results for the three runs, in form of ratios of the loop counts, are summarized in Table 6.1. The foil thickness given is the mean thickness of the area (= 4.5 μm x 3.5 μm) under observation. The fractions in the 'w negative' and 'w positive' columns indicate the ratio of the number of loops after a 20 min. irradiation, in anomalous absorption and anomalous transmission regions respectively, to the initial number of loops. The scatter in the readings is indicated as the standard error of the mean. As a check on

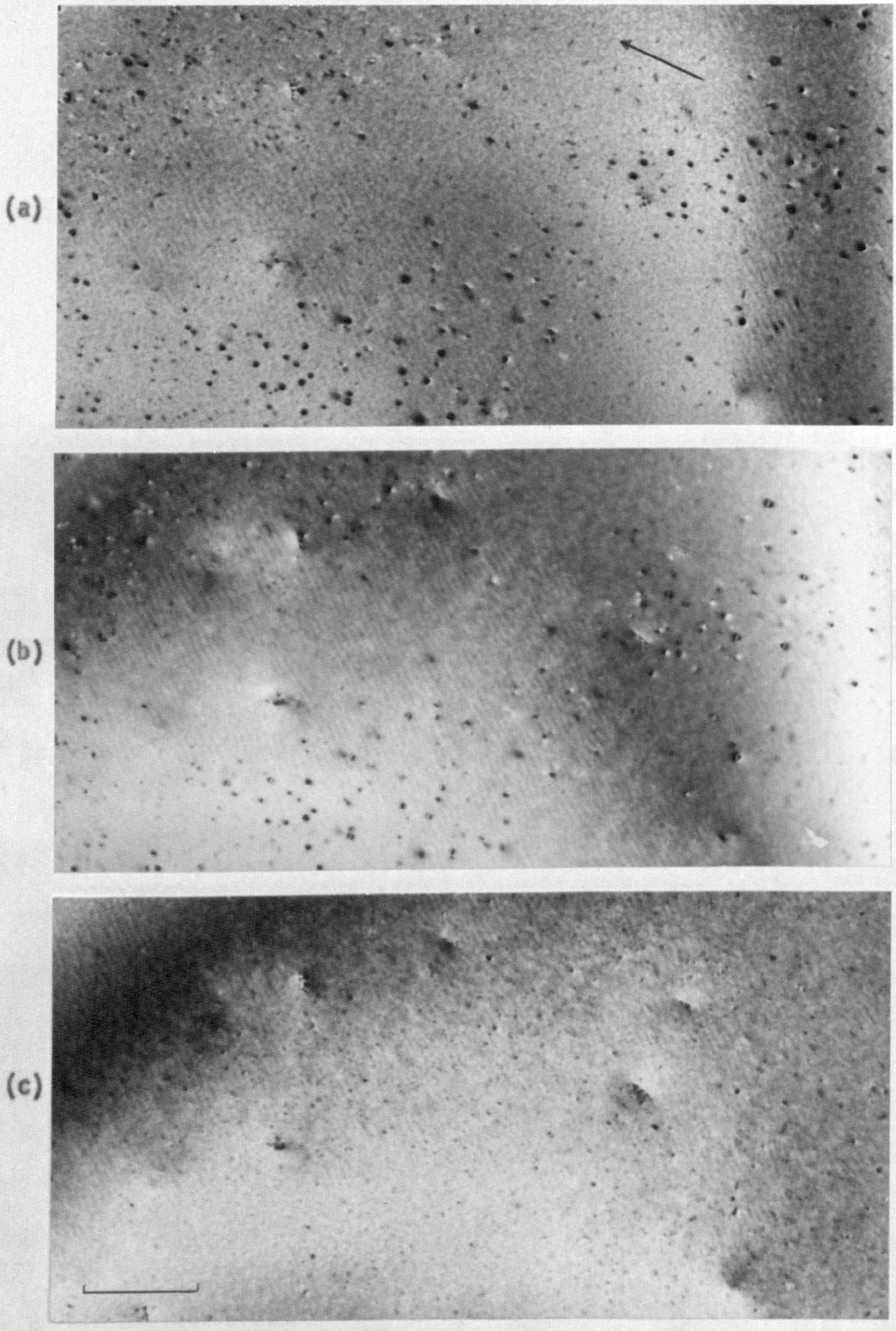

Figure 6.2. A thin area of Al 6N containing small vacancy loops. Micrographs taken at various times after irradiation under w < 0 conditions in the electron beam : (a) 0 min. (b) 20 min. (c) 100 min. Note the change in the density of the loops and the variation of contrast and exposure.

Foil normal and beam direction : $[2\bar{1}3]$; $\underline{g}$: $\bar{1}11$; 200 kV.

Table 6.1. Results for Irradiation under Anomalous Absorption and Anomalous Transmission Conditions

Run	Foil Thickness	w negative	w positive
1	2000 Å	0.71 ± 0.04	0.91 ± 0.01
2	3000 Å	0.87 ± 0.01	0.90 ± 0.02
3	5500 Å	0.83 ± 0.02	1.05 ± 0.05

the error due to different exposure during printing, and in personal error during counting, some counts of the loops were done on a number of prints made from the same plate, and by two independent observers. The results of these counts were found to be in reasonable agreement with each other.

The irradiation time of 20 min. was chosen arbitrarily as the damage was easily detectable in this time and as no complications due to the nucleation of clusters of the radiation induced defects arose in such a short time. Such a nucleation of new clusters was observed after prolonged irradiation in form of a large number of very small loops. Figures 6.2(a) - (c) show three micrographs of the same area (run 1, w negative) taken at irradiation times of 0 min., 20 min. and 100 min. The number of loops in Figure (b) has reduced to ≈ 0.7 of the initial number in (a). The appearance of numerous very small loops after long irradiation time can be seen in Figure (c) where the number of loops is two to three times higher than that in (a), while many of the original vacancy loops have disappeared. The variation of contrast and exposure in the three pictures also illustrates the remarks made earlier about the difficulty of keeping the same overall observation conditions.

It is very difficult, due to the large scatter in the experimental results, to draw any positive conclusions about the enhancement of

displacement damage during irradiation in anomalous absorption conditions. It is also not possible to say anything about the effect of specimen thickness on this phenomenon due to the small number of experiments. It seems however that the enhancement of displacement damage during anomalous absorption is not as large as the predicted increase of 3 : 1 over anomalous transmission when no account is taken of interband scattering. These preliminary results have been very useful in determining the exact experimental conditions which must be met to study this effect with greater accuracy. In particular, a large number of experimental runs, with careful control over the exact contrast and exposure during picture taking, are required to reduce the scatter and to make any quantitative deductions.

To summarize, the annihilation of quenched-in vacancy loops has been shown to be a sensitive method for the detection of damage in an electron microscope. This method has been used to present evidence of radiation damage in aluminium at 200 keV electron energy. Experiments done to detect the enhancement of displacement damage during irradiation under anomalous absorption conditions suggest that this effect, if present, is small.

CHAPTER SEVEN

CONCLUSIONS

A summary will now be given of the main results and the conclusions arrived at in previous chapters. Some aspects of the work which could not be explored in sufficient detail will be pointed out while some of the issues arising naturally out of this work will be examined and any useful experiments that suggest themselves will be considered. A cautionary remark may however be added regarding the essentially tentative nature of this chapter which makes it necessary that the proposals made be further examined carefully and critically before embarking on any suggested work.

It has been shown that a supersaturation of vacancies can be used to 'decorate' submicroscopic features under appropriate conditions. These conditions can be obtained by quenching very pure samples from moderate temperatures, ensuring thereby that the defects of interest are decorated rather than impurities and self-sinks. This technique is obviously applicable to only those materials which can be successfully quenched to produce a high supersaturation of vacancies. Moreover, the material should be obtainable in sufficiently high purity so that the impurity nucleation of clusters does not swamp out the effects under observation. These two conditions immediately limit the use of this method to a handful of metals such as aluminium, gold and silver, and to a certain extent nickel and copper.

In the present work this decoration technique has been used for the observation of submicroscopic defects produced by deformation. It can also be employed in the study of the effects of irradiation. For example, a specimen 'sensitized' by quenching may be irradiated to reveal any directionality in the damage, such as a channelling or

focussing effect in a particular direction. In this respect this method has two advantages over the conventional practice where clusters formed by the radiation induced defects are examined. Firstly, the proposed method is useful where prolonged irradiation is not possible so that not enough defects are introduced to grow into observable clusters by themselves. Secondly, the quenched-in vacancies would decorate the radiation induced vacancies or vacancy clusters which, due to their low mobility as compared to the interstitials, are likely to show any directionality in damage more markedly. The decoration technique may also be usable for recording in metals the tracks of energetic particles, such as fission fragments, heavy ions or protons, an observation hitherto restricted to some of the inorganic materials and plastics.

This method of observation, by the decoration phenomenon, suffers from one drawback, namely that the vacancy supersaturation can itself influence the observed behaviour. In the study of deformation as described in this thesis the nature and the character of the dislocations is altered by interaction with the quenched-in vacancies. Most of the observed rows of loops and faulted dipoles are perhaps produced from jogs formed due to this interaction. Further, any extrinsic dipoles produced during deformation cannot survive in the high supersaturation of vacancies. In an irradiation experiment of the type proposed, the formation of interstitial clusters is likely to be similarly suppressed due to their annihilation by the quenched-in vacancies.

The successful use of the decoration effect has been demonstrated in aluminium by the observation of rows of loops and faulted dipoles along <110>. The initial formation of these defects has been attributed to a mechanism based on the dragging of sessile 90^0 jogs on moving screw dislocations. Some of the less critical conditions in the formation of these two defects have not been fully analysed. The role of hydrogen atmosphere during the observation of the rows of loops in quenches from near the melting point needs greater clarification. The explanation

based on the nucleation of voids fits the known facts very well. The question that remains unanswered is why all the vacancies do not disappear at the voids. It may be that the voids are not as strong nuclei as the dislocation loops and that the observed high density of voids is only due to their earlier nucleation. The effect of the temperature of deformation on the formation of the rows of loops and the faulted dipoles could have been further investigated. There was a very marked difference in the density of these defects for the deformation temperatures of -195°C and -90°C. The temperature of deformation could be usefully investigated in smaller steps in the region -195°C to -90°C. In principle, it may thus be possible to evaluate the approximate binding energy of a vacancy in a vacancy platelet, by determining the temperature where a sharp decrease occurs in the density of the rows and the faulted dipoles.

The observations on the formation of rows of secondary defects and faulted dipoles may also be extended to gold. The role of decoration in this case could be unambiguously proved by comparing the widths of faulted dipoles formed under identical deformation conditions in quenched and unquenched samples. An increase in the density of the faulted dipoles in the quenched case would determine the contribution of the jogs produced by dislocation-vacancy interaction to the formation of these dipoles.

The observation of faulted dipoles in unidirectionally deformed aluminium would be of intrinsic interest. This investigation can be pursued with greater confidence after the computations reported in Chapter 3. According to these computations even the narrowest faulted dipole in aluminium should be visible under suitable contrast conditions. A systematic search for these dipoles could be carried out on single crystals subjected to the optimum deformation conditions as set out in Chapter 4. The Burgers vector can then be predicted from the tensile axis of the crystal, and electron microscope investigation carried out at small w (< 0.5) in the 311 reflection nearest to the Burgers vector

or in a 220 reflection in which the dipole is likely to be visible. As the dipole is expected to be very narrow it might easily anneal out at room temperature. Hence the specimen must be kept cold after the low temperature deformation, polished cold, and examined immediately in the electron microscope. Furthermore, the examination of these specimens should be restricted to the 100 kV or 150 kV microscopes as the annihilation of small loops and the annealing of relatively wide faulted dipoles has been observed at 200 kV.

A search for faulted dipoles in unquenched but appropriately deformed aluminium specimens may not necessarily be successful. Most of the 90^{0} jogs in quenched and deformed aluminium, which have been shown to form the faulted dipoles, are probably produced by the sweeping up of vacancies by the screw dislocations. It may be that during the normal deformation processes few 90^{0} jogs are produced, while the 60^{0} jogs, which, due to their dissociated nature, can form faulted dipoles in low stacking-fault energy metals, would be glissile in aluminium. Hence very few faulted dipoles may be produced in unquenched deformed aluminium. If the faulted dipoles are observed in such a case then the evaluation of stacking-fault energy from their width may not be as simple as previously implied in literature (Seeger and Wobser 1966; Steeds 1967a). On the analysis given in this thesis such an evaluation would require calculations of the transition width which take into account the stress on the 90^{0} jog that forms the dipole

The effective decoration phonomenon has been shown to reveal a different feature when aluminium is quenched down to temperatures $\approx 70^{0}C$ and deformed during the quench. This is the observation of a high density of segmented helices in such a case. Interaction of the vacancy supersaturation with the screw dislocations to form helices again illustrates the earlier remark about the conditions of decoration influencing the observed behaviour. The experimental conditions used in the production of helical dislocations in aluminium have not been exhaustively studied.

The density of the helices could perhaps be further increased by the optimization of these conditions. In particular, the amount of deformation given to the specimen was not varied in the experiments described in Chapter 5. A maximum in the density of helices might be obtained by a further adjustment of the amount of deformation and the temperature of the quenching bath. To further confirm that the observed segmented form of the helix is a lower energy configuration it would be in order to do careful X-ray topographical examination of the helices sometimes observed in slowly furnace cooled single crystals of aluminium. These would presumably be found to be segmented.

The helices, along $\langle\bar{1}10\rangle$, in aluminium (f.c.c. structure) have been found to be geodesics on the prism formed by the {111} glide planes. Observation and analysis of segmented helices in materials having different crystal structures would not be without interest as it would determine the particular glide planes that are active. Further experiments on lead iodide (h.c.p. based structure) of the type done by Forty (1960, 1961) are required with micrographs taken in different beam directions to enable the determination of the orientation of the segments and hence the planes on which they lie. These planes could again be revealed by the characteristic projection of the helix when viewed along a direction lying in these planes. As predicted earlier, the glide prism in lead iodide is expected to be made up of the $\{10\bar{1}n\}$ pyramidal planes containing the $\langle 1\bar{2}10\rangle$ helix direction. Amelinckx et al (1957b) have suggested a specific prism of {001}{110} planes, containing the $\langle\bar{1}10\rangle$ helix axis, as the glide surface of the angular helices observed by them in sodium chloride. The observation of these authors was only a preliminary one and needs further confirmation. The formation and analysis of angular helices would also be relevant in b.c.c. materials, such as molybdenum, to determine the planes on which slip takes place. Different glide planes might be observed

depending on the temperature of nucleation of the helix. If the slip planes are {110} then three different prisms might be expected for the <1$\bar{1}$1> helix axis as this direction is contained in three {110} planes. An alternative configuration of the segmented helix, lying on a hexagon based prism formed from the three {110} glide planes might very well be observed, as this would be of lower energy due to the shorter line length. These experiments could be used, in a manner similar to that described in Chapter 5, to estimate the reduction in core energy, in different structures, when a dislocation lies in its glide plane.

The technique for the sensitive detection of radiation damage by the annihilation of vacancy loops offers a number of possibilities. One simplification introduced by the observation of annihilation of existing loops rather than the appearance of radiation induced defect clusters is that a nucleation problem does not have to be considered. It is possible, using this method, to get conclusive results on the enhancement of displacement damage during anomalous absorption conditions by performing a large number of experiments, bearing in mind all the factors affecting the sensitivity and accuracy of detection that have been discussed in Chapter 6. In this regard the stringent requirements of uniform contrast and exposure cannot be overemphasized. Once the essential experimental conditions have been fully controlled it is very easy to investigate in the electron microscope the orientation dependence of radiation damage, and to determine the displacement threshold energy by irradiating at different electron energies.

APPENDIX A

DETERMINATION OF THE SENSE OF THE BURGERS VECTOR

The determination of the Burgers vector $\underline{b}$ depends on the visibility or otherwise of a defect in a particular reflection $\underline{g}$, and it can be evaluated from the $\underline{g} \cdot \underline{b}$ criteria as given in Chapter 3. Determination of the nature of a dislocation loop, i.e. whether it is of interstitial or vacancy type, requires the knowledge of the exact relation of the Burgers vector to the foil normal. According to the conventions for the Burgers vector and for the positive sense around the loop as described in Chapter 3, the Burgers vector of a vacancy loop makes an acute angle with the upward drawn normal to the foil (referred to as $\underline{n}$ hereafter) and that of an interstitial loop an obtuse angle. Thus to determine the nature of the loops one has to unambiguously fix $\underline{n}$ and determine $\underline{b}$ relative to the chosen $\underline{n}$.

The foil normal, and its sense, can be selected arbitrarily from the observed zero-tilt electron diffraction pattern or from an X-ray back-reflection Laue pattern. However, if a prior decision, such as that of the tensile axis, has been made this choice of foil normals is immediately restricted. The discussion will be made simpler if a hypothetical case is considered. Suppose the tensile axis is determined from the X-ray Laue pattern to be <532> type and the foil normal <1$\bar{3}$2> type. If the tensile axis is chosen to lie in the [001][101][111] stereographic triangle, as in the rest of this thesis, then the tensile axis becomes [325] and $\underline{n}$ can be either [$\bar{3}$21] or [3$\bar{2}$1]. The vector $\underline{n}$ can now be uniquely determined from the electron diffraction pattern (or from the X-ray Laue) as [$\bar{3}$21] or [3$\bar{2}$1] because the two patterns, being non-symmetrical, are distinguishable from each other, as shown in Figure A.1.

If the zero-tilt diffraction pattern contains a rotational symmetry

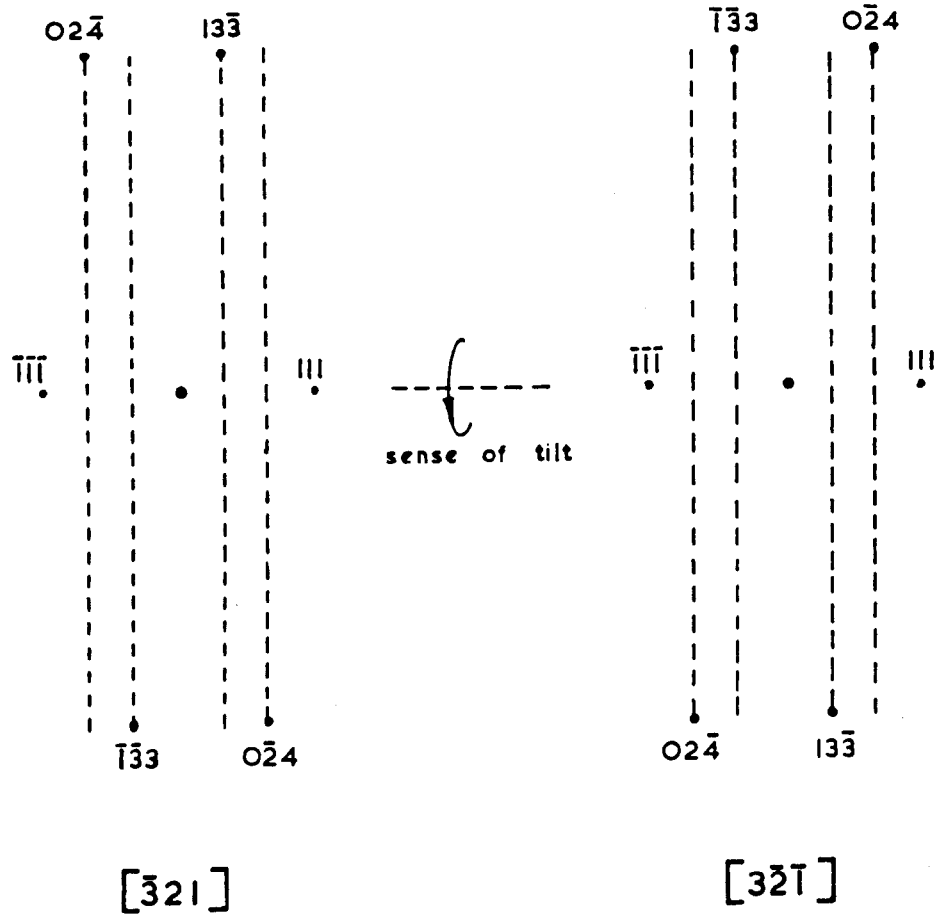
$02\bar{4}$
$13\bar{3}$
$\bar{1}\bar{1}\bar{1}$
111
$\bar{1}\bar{3}3$
$0\bar{2}4$
sense of tilt
$\bar{1}\bar{3}3$
$0\bar{2}4$
$\bar{1}\bar{1}\bar{1}$
111
$02\bar{4}$
$13\bar{3}$
$[\bar{3}21]$
$[3\bar{2}\bar{1}]$

Figure A.1

axis (i.e. the pattern has one or more of its indices zero, or two or more equal) then the case is slightly more complicated. In this case it becomes necessary to tilt to a nearby asymmetric pattern. The sense of $\underline{n}$ can then be found by determining the upward drawn normal of this asymmetric pattern.

To determine the sense of the Burgers vector from the $\underline{g} \cdot \underline{b}$ criteria one must know the sign of $\underline{g}$. This can be done easily after $\underline{n}$ has been determined. The method involves the tilting of the specimen in a known sense about the relevant $\underline{g}$ so that one diffraction pattern changes to another, and by noting the emergence of the new diffraction spots. Considering again the $[\bar{3}21]$ pattern in Figure A.1, the indexing of various spots is still uncertain with respect to sign and corresponds to a possible rotation of the reference coordinate frame by 180° about the $[\bar{3}21]$ axis, i.e. the spot labelled 111 may actually be $\bar{1}\bar{1}\bar{1}$, $13\bar{3}$ be $\bar{1}3\bar{3}$, and so on. Now suppose that after tilting in a particular direction through 19° the $[\bar{1}10]$ pattern comes up. The labelling of the spots as given will then be correct if the sense of tilt is as shown. The reasoning is as follows. The $[\bar{3}21]$, $[13\bar{3}]$ and $[02\bar{4}]$ directions make an acute angle with $[\bar{1}10]$. Thus the $[\bar{1}10]$ direction is coming out of the paper inclined towards the $13\bar{3}$ and $02\bar{4}$ side of the $\bar{1}\bar{1}\bar{1}$ - 111 axis. Hence to bring up the $[\bar{1}10]$ pattern, i.e. to make $[\bar{1}10]$ direction perpendicular to the plane of the paper, a tilt about $\bar{1}\bar{1}\bar{1}$ - 111 axis as shown is required. It can be similarly proved that if the actual sense of tilt required to bring up the $[\bar{1}10]$ pattern is opposite to that shown the labelling of the spots should be changed to the negative of what it is now.

The sense of tilt can be determined from the motion of the Kikuchi bands on the screen as the specimen is tilted. For example, if we consider the $[\bar{3}21]$ pattern in Figure A.1, then for the sense of tilt shown, the centre of the $[\bar{3}21]$ Kikuchi pattern will move towards

the top of the page. Thus the spots in this diffraction pattern are labelled correctly if after a 19^{0} tilt the [$\bar{1}$10] Kikuchi pattern moves up from the bottom of the page.

It may be noted that in all this discussion only the diffraction patterns have been considered. Micrographs have been consulted only to see if a particular defect was visible or not for the given reflection.

APPENDIX B

MEASUREMENT OF w AND THE SELECTION OF ANOMALOUS ABSORPTION COEFFICIENT

The dimensionless deviation parameter w is given by :

$$w = s\xi_g$$

where s is the deviation from the exact Bragg position and ξ_g is the extinction distance for the relevant reflection g.

The value of s in terms of g can be very simply measured from the position of the Kikuchi lines on the electron diffraction pattern. When the crystal is at the exact Bragg reflecting position g = hkℓ, then the Kikuchi lines corresponding to this spot pass through the centre spot 0 and the g spot, the lines corresponding to 2g pass midway between 0 and -g, and g and 2g, the lines corresponding to 3g pass through -g and 2g spots, and so on. At this position s, and hence w, is zero for the reflection g. When the crystal is tilted through the Bragg angle θ_B so that the 2g reflection is excited the whole Kikuchi pattern is shifted rigidly by ½g towards the 2g spot, and w is now zero for the 2g reflection. Thus when the crystal is tilted through θ_B the Kikuchi pattern moves by ½g and s for the reflection $g_{hk\ell}$ changes from 0 to $g\theta_B$. A parameter f can therefore be defined as the ratio of the displacement of the 1st order hkℓ Kikuchi line nearest the 000 spot to ½g. The displacement is positive if this line moves towards the hkℓ spot and negative otherwise.

Then
$$\begin{aligned} s &= f.g\theta_B \\ &= f.\tfrac{1}{2}g^2\lambda \qquad \text{since } \sin\theta = \theta \\ &= f(h^2 + k^2 + \ell^2).\ \lambda/2a^2 \end{aligned}$$

where λ is the incident electron wave length and a the lattice parameter.

$$\text{Hence } w = s\xi_g$$

$$= f(h^2 + k^2 + \ell^2).\ \lambda\xi_g/2a^2$$

In practice the third order Kikuchi line (corresponding to the 3g spot) was normally used to make the measurements of w. This makes no difference to the essentials of the method but gives a more accurate measurement.

The value of the anomalous absorption coefficient of 0.03 used for the computation of images in Chapter 3 is based on the calculations of Humphreys and Hirsch (1968). These authors have shown that the normally used value of the anomalous absorption coefficient $V_g'/V_g = 0.1$ (where V_g' and V_g are the Fourier coefficients of the imaginary and real parts of the complex lattice potential) derived by Hashimoto et al (1962) is not appropriate for light elements and for small values of g. In aluminium for $g = 200$ ($= 0.5$ Å^{-1} in magnitude) Humphreys and Hirsch calculate $V_g'/V_g = 0.027$ for 100 kV electrons. This is in agreement with the value of 0.035 found suitable for silicon (Humphreys et al 1967) which is expected to have an anomalous absorption coefficient only slightly different from that of aluminium.

As the value of V_g'/V_g varies inversely with the velocity of the electrons, the relevant value in aluminium at 200 kV decreases to 0.021. This however is calculated for zero aperture size. To include the effect of the finite objective aperture size of 20 μm, corresponding to an angular aperture $= 0.8\ \theta_B$, roughly extrapolated curves of Metherell and Whelan (1967) for aperture dependence were used. Thus, taking into account a total increase of 20% for finite aperture size and single electron scattering, the final value of the anomalous absorption coefficient in aluminium for 200 reflection and 200 kV electrons comes to ≥ 0.026.

REFERENCES

Amelinckx, S. 1964 "The direct observation of dislocations", p.379. London : Academic Press.

Amelinckx, S., Bontinck, W., Dekeyser, W. and Seitz, F. 1957a Phil. Mag. 2, 355.

Amelinckx, S., Bontinck, W. and Maenhout-Van der Vorst, W. 1957b Physica 23, 270.

Andrade, E.N. da C. and Aboav, D.A. 1957 Proc. Roy. Soc. Lond. A. 240, 304.

Authier, A., Rogers, C.B. and Lang, A. 1965 Phil. Mag. 12, 547.

Bacon, D.J. 1966 Phil. Mag. 14, 715.

Bacon, D.J. and Crocker, A.G. 1966 Phil. Mag. 13, 217.

Balluffi, R.W., Koehler, J.S. and Simmons, R.O. 1963 "Recovery and recrystallization of metals", p.1. New York : Interscience.

Barnes, R.S. and Mazey, D.J. 1963 Acta metall. 11, 281.

Barrett, C.S. and Massalski, T.B. 1966 "Structure of metals", p.211. New York : McGraw-Hill.

Basinski, Z.S. 1964 Disc. Faraday Soc. 38, 93.

Becker, C. and Pegel, B. 1969 Phys. Stat. Sol. 32, 443.

Bilby, B.A., Bullough, R. and Smith, E. 1955 Proc. Roy. Soc. Lond. A. 231, 263.

Bollmann, W. 1956 Phys. Rev. 103, 1588.

Bontinck, W. 1957 Phil. Mag. 2, 561.

Bontinck, W. and Amelinckx, S. 1957 Phil. Mag. 2, 94.

Broadway, M.J. 1969 Private communication.

Bullough, R. and Foreman, A.J.E. 1964 Phil. Mag. 9, 315.

Bullough, R. and Newman, R.C. 1960 Phil. Mag. 5, 921.

Carpenter, H.C.H. and Elam, C.F. 1921 Proc. Roy. Soc. Lond. A. 100, 329.

Cass, T.R. and Washburn, J. 1966 Proc. Br. Ceramic Soc. 6, 239.

Chen, K.Y. and Meshii, M. 1966 "Sixth Int. Congr. Electron Microscopy, Kyoto", Vol.1, p.319. Tokyo : Maruzen Co. Ltd.

Chik, K.-P. 1965a Phys. Stat. Sol. 10, 659.

Chik, K.-P. 1965b Phys. Stat. Sol. 10, 675.

Clarebrough, L.M., Humble, P. and Loretto, M.H. 1967 Acta metall. 15, 1007.

Clarebrough, L.M., Segall, R.L., Loretto, M.H. and Hargreaves, M.E. 1964 Phil. Mag. 9, 377.

Corbett, J.W. 1966 "Electron radiation damage in semiconductors and metals", London : Academic Press.

Cosslett, V.E. 1967 Sci. Prog., Oxf. 55, 15.

Cotterill, R.M.J. 1966 Appl. Phys. Letters 9, 29.

Cotterill, R.M.J. and Jones, M.W. 1964 Phil. Mag. 10, 535.

Cotterill, R.M.J. and Segall, R.L. 1963 Phil. Mag. 8, 1105.

Cottrell, A.H. 1953a "Dislocations and plastic flow in crystals", p.50. Oxford : University Press.

Cottrell, A.H. 1953b Ibid., p.51.

Crocker, A.G. and Bacon, D.J. 1967 Phil. Mag. 15, 1155.

Dash, W.C. 1958 J. appl. Phys. 29, 705.

Dash, W.C. 1960 J. appl. Phys. 31, 2275.

Davis, T.L. 1967 J. appl. Phys. 38, 3756.

Davis, T.L. and Hirth, J.P. 1966a J. appl. Phys. 37, 2112.

Davis, T.L. and Hirth, J.P. 1966b "Consultants symposium on the nature of small defect clusters", p.106. Harwell : U.K.A.E.A.

Davis, T.L. and Hirth, J.P. 1967 J. appl. Phys. 38, 2390.

Dawe, D.W. and Dewey, M.A.P. 1963 Aecn Laboratories Rep. No. 288.

de Jong, M. and Koehler, J.S. 1963 Phys. Rev. 129, 49.

de Wit, R. 1959 Phys. Rev. 116, 592.

de Wit, R. 1960 "Solid State Physics", Vol.10, p.249. London : Academic Press.

Dobson, P.S., Goodhew, P.J. and Smallman, R.E. 1967 Phil. Mag. 16, 9.

Doyama, M. 1965a "Lattice defects in quenched metals", p.163. New York : Academic Press.

Doyama, M. 1965b Ibid., p.185.

Doyama, M. and Koehler, J.S. 1964 Phys. Rev. 134, A522.

Duncumb, P. 1962 Phil. Mag. 7, 2101.

Edington, J.W. 1969 Private communication.

Eikum, A. and Thomas, G. 1963 J. Phys. Soc. Japan 18, Suppl. III, 98, (Proc. Int. Conf. Crystal Lattice Defects, 1962).

Embury, J.D. 1963 Ph.D. Thesis, Cambridge University.

Embury, J.D., Sargent, C.M. and Nicholson, R.B. 1962 Acta metall. 10, 1118.

Essmann, U. 1963 Phys. Stat. Sol. 3, 932.

Foreman, A.J.E. 1955 Acta metall. 3, 322.

Foreman, A.J.E. 1967 Phil. Mag. 15, 1011.

Forty, A.J. 1960 Phil. Mag. 5, 787.

Forty, A.J. 1961. Phil. Mag. 6, 587.

Fourie, J.T. 1964 Phil. Mag. 10, 1027.

Fourie, J.T. and Murphy, R.J. 1962 Phil. Mag. 7, 1617.

Fourie, J.T. and Wilsdorf, H.G.F. 1960 J. appl. Phys. 31, 2219.

Frank, F.C. 1949 Proc. Phys. Soc. A. 62, 202.

Frank, F.C. 1950 "Symp. Plastic Deformation Cryst. Solids", p.150. Pittsburgh : Carnegie Inst. Technol.

Frank, F.C. 1951 Phil. Mag. 42, 809.

Frenkel, J. 1926 Z. Physik 35, 652.

Friedel, J. 1964a "Dislocations", p.6. Oxford : Pergamon Press.

Friedel, J. 1964b Ibid., p.22.

Garstone, J., Honeycombe, R.W.K. and Greetham, G. 1956 Acta metall. 4, 485.

Gilman, J.J. and Johnston, W.G. 1962 "Solid State Physics", Vol.13, p.147. London : Academic Press.

Grilhé, J. 1964 Acta metall. 12, 1081.

Grilhé, J. 1966 Acta metall. 14, 931.

Groves, G.W. and Kelly, A. 1961 Phil. Mag. 6, 1527.

Groves, G.W. and Kelly, A. 1962 Phil. Mag. 7, 892.

Hall, C.R. 1966 Proc. Roy. Soc. Lond. A. 295, 140.

Hall, C.R. and Hirsch, P.B. 1965 Proc. Roy. Soc. Lond. A. 286, 158.

Hashimoto, H., Howie, A. and Whelan, M.J. 1962 Proc. Roy. Soc. Lond. A. 269, 80.

Häussermann, F. and Wilkens, M. 1966 Phys. Stat. Sol. 18, 609.

Head, A.K. 1967 Aust. J. Phys. 20, 557.

Heidenreich, R.D. 1949 J. appl. Phys. 20, 993,

Henriksen, L., Johansen, A., Koch, J., Andersen, H.H., Leffers, T. and Cotterill, R.M.J. 1968 Can. J. Phys. 46, 641.

Hirsch, P.B. 1962 Phil. Mag. 7, 67.

Hirsch, P.B. 1968 Private communication.

Hirsch, P.B., Horne, R.W. and Whelan, M.J. 1956 Phil. Mag. 1, 677.

Hirsch, P.B., Howie, A., Nicholson, R.B., Pashley, D.W. and Whelan, M.J. 1965a "Electron microscopy of thin crystals", p.263. London : Butterworths.

1965b Ibid., p.453.

1965c Ibid., p.496.

Hirsch, P.B., Howie, A. and Whelan, M.J. 1962 Phil. Mag. 7, 2095.

Hirsch, P.B., Silcox, J., Smallman, R.E. and Westmacott, K.H. 1958 Phil. Mag. 3, 897.

Hirsch, P.B. and Steeds, J.W. 1963 "The relation between structure and mechanical properties of metals", Vol.1, p.48. London : H.M.S.O.

Hirth, J.P. and Lothe, J. 1968a "Theory of dislocations", p.19. New York : McGraw-Hill.

Hirth, J.P. and Lothe, J. 1968b Ibid., p.209.

Hirth, J.P. and Pound, G.M. 1963 "Condensation and evaporation". Oxford : Pergamon Press.

Holwech, I. and Risnes, R. 1967 J. Crystal Growth 1, 249.

Honeycombe, R.W.K. 1959 Metall. Rev. 4, 1.

Honeycombe, R.W.K. 1961 "Progress in Materials Science" 9, 93.

Howie, A. 1963 Proc. Roy. Soc. Lond. A. 271, 268.

Howie, A. 1969 Private communication.

Howie, A. and Valdrè, U. 1963 Phil. Mag. 8, 1981.

Howie, A. and Whelan, M.J. 1961 Proc. Roy. Soc. Lond. A. 263, 217.

Howie, A. and Whelan, M.J. 1962 Proc. Roy. Soc. Lond. A. 267, 206.

Hudson, B. and Makin, M.J. 1965 Phil. Mag. 11, 423.

Humble, P. 1968 Aust. J. Phys. 21, 325.

Humble, P. 1969 Private Communication.

Humphreys, C.J. and Hirsch, P.B. 1968 Phil. Mag. 18, 115.

Humphreys, C.J., Howie, A. and Booker, G.R. 1967 Phil. Mag. 15, 507.

Huntington, H.B. 1942 Phys. Rev. 61, 325.

Huntington, H.B. and Seitz, F. 1942 Phys. Rev. 61, 315.

Imura, T. and Hashimoto, H. 1966 "Sixth Int. Congr. Electron Microscopy, Kyoto, "Vol.1, p.297. Tokyo : Maruzen Co. Ltd.

Ipohorski, M. and Spring, M.S. 1969 Phil. Mag. 20, 937.

Iseler, G.W., Dawson, H.I., Mehner, A.S. and Kauffman, J.W. 1966 Phys. Rev. 146, 468.

Jackson, J.J. 1965 "Lattice defects in quenched metals", p.479. New York : Academic Press.

Jacobs, M.H. 1969 Private communication.

Johnston, I.A., Dobson, P.S. and Smallman, R.E. 1968 "Proc. Int. Conf. on Vacancies and Interstitials in Metals", p.140. Jülich (Germany).

Johnston, W.G. and Gilman, J.J. 1960 J. appl. Phys. 31, 632.

Jones, D.A. and Mitchell, J.W. 1958 Phil. Mag. 3, 1.

Jøssang, T., Lothe, J. and Skylstad, K. 1965 Acta metall. 13, 271.

Kauffman, J.W. and Koehler, J.S. 1952 Phys. Rev. 88, 149.

Kiritani, M. 1964 J. Phys. Soc. Japan 19, 618.

Kiritani, M. 1965 J. Phys. Soc. Japan 20, 1834.

Kiritani, M., Nishikawa, T. and Yoshida, S. 1969 J. Phys. Soc. Japan 27, 67.

Kiritani, M., Sato, A., Sawai, K. and Yoshida, S. 1968 J. Phys. Soc. Japan 24, 461.

Kiritani, M., Sato, A. and Yoshida, S. 1966a J. Phys. Soc. Japan 21, 1955.

Kiritani, M., Sato, A. and Yoshida, S. 1966b J. Phys. Soc. Japan 21, 2291.

Kiritani, M. and Yoshida, S. 1963 J. Phys. Soc. Japan 18, 915.

Kritzinger, S., Smallman, R.E. and Dobson, P.S. 1969 Acta metall. 17, 49.

Kroupa, F. and Brown, L.M. 1961 Phil. Mag. 6, 1267.

Kuhlmann-Wilsdorf, D. 1958 Phil. Mag. 3, 125.

Lally, J.S. and Partridge, P.G. 1966 Phil. Mag. 13, 9.

Lang, A.R. and Meyrick, G. 1959 Phil. Mag. 4, 873.

Li, J.C.M. and Swann, P.R. 1964 Phil. Mag. 10, 617.

Loretto, M.H., Clarebrough, L.M. and Humble, P. 1966 Phil. Mag. 13, 953.

Lorimer, G.W. 1967 Ph.D. Thesis, Cambridge University.

Lorimer, G.W. and Nicholson, R.B. 1969 Private communication.

Low, J.R. and Turkalo, A.M. 1962 Acta metall. 10, 215.

Mader, S. 1963 "Electron microscopy and strength of crystals", p.183. New York : Interscience.

Makin, M.J. 1968a "Fourth European Regional Conf. Electron Microscopy, Rome", Vol.1, p.33. Rome : T.P. Vaticana.

Makin, M.J. 1968b Phil. Mag. 18, 637.

Makin, M.J. and Hudson, B. 1963 Phil. Mag. 8, 447.

Makin, M.J. and Sharp, J.V. 1968 J. Materials Science 3, 360.

Mazey, D.J., Barnes, R.S. and Howie, A. 1962 Phil. Mag. 7, 1861.

McComb, J.A. and Meshii, M. 1966 "Sixth Int. Congr. Electron Microscopy, Kyoto", Vol.1, p.347. Tokyo : Maruzen Co. Ltd.

McComb, J.A. and Meshii, M. 1967 J. appl. Phys. 38, 2368.

Meshii, M. 1965 "Lattice defects in quenched metals", p.387. New York : Academic Press.

Meshii, M., McComb, J.A., Chen, K.Y. and Mori, T.H. 1966 "Consultants symposium on the nature of small defect clusters", p.84. Harwell : U.K.A.E.A.

Metherell, A.J.F. and Whelan, M.J. 1967 Phil. Mag. 15, 755.

Mitchell, J.M. 1962 J. appl. Phys. 33, 406.

Mori, T. and Meshii, M. 1964 Acta metall. 12, 104.

Morozumi, S., Tsuno, N. and Koda, S. 1969 Trans. Japan Inst. Metals 10, 64.

Nabarro, F.R.N. 1948 "Rept. Conf. Strength Solids", p.75 London : The Physical Society.

Nabarro, F.R.N. 1967a "Theory of crystal dislocations", p.12, Oxford : University Press.

Nabarro, F.R.N. 1967b Ibid., p.252.

Nabarro, F.R.N. 1967c Ibid., p.384.

Nabarro, F.R.N., Basinski, Z.S. and Holt, D.B. 1964 Advanc. Phys. 13, 193.

Nankivell, J.F. 1962 Br. J. appl. Phys. 13, 126 and 129.

Neely, H.H. and Bauer, W. 1966 Phys. Rev. 149, 535.

Noggle, T.S. and Koehler, J.S. 1957 J. appl. Phys. 28, 53.

Nøst, B., Sørensen, G. and Nes, E. 1967 J. Crystal Growth 1, 149.

Nowick, A.S. 1951 Phys. Rev. 82, 551.

Price, P.B. 1960 Phil. Mag. 5, 873.

Price, P.B. 1961a Phil. Mag. 6, 449.

Price, P.B. 1961b J. appl. Phys. 32, 1750.

Quader, M.A. and Dodd, R.A. 1968 Phil. Mag. 17, 575.

Read Jr., W.T. 1953a "Dislocations in crystals", p.32. New York : McGraw-Hill.

Read Jr., W.T. 1953b Ibid., p.105.

Schottky, W. and Wagner, C. 1930 Z. Phys. Chem. 11B, 163.

Seeger, A. 1964 Disc. Faraday Soc. 38, 82.

Seeger, A. and Wobser, G. 1966 Phys. Stat. Sol. 18, 189.

Segall, R.L. and Clarebrough, L.M. 1964 Phil. Mag. 9, 365.

Segall, R.L. and Partridge, P.G. 1959 Phil. Mag. 4, 912.

Segall, R.L., Partridge, P.G. and Hirsch, P.B. 1961 Phil. Mag. 6, 1493.

Segall, R.L. and Shoaib, K.A. 1970 Phil. Mag. (in the press).

Seidman, D.N. and Balluffi, R.W. 1964 Phil. Mag. 10, 1067.

Seitz, F. 1950 Phys. Rev. 79, 890.

Seitz, F. 1952 Advanc. Phys. 1, 43.

Seitz, F. and Koehler, J.S. 1956 "Solid State Physics", Vol.2, p.305. London : Academic Press.

Shimomura, Y. and Yoshida, S. 1967 J. Phys. Soc. Japan 22, 319.

Shoaib, K.A. and Segall, R.L. 1968 "Fourth European Regional Conf. Electron Microscopy, Rome", Vol.1, p.433. Rome : T.P. Vaticana.

Shoaib, K.A. and Segall, R.L. 1969 Proc. Roy. Soc. Lond. A. 314, 129.

Siegel, R.W. 1966 Phil. Mag. 13, 337.

Silcock, J.M. and Tunstall, W.J. 1964 Phil. Mag. 10, 361.

Silcox, J. and Hirsch, P.B. 1959a Phil. Mag. 4, 72.

Silcox, J. and Hirsch, P.B. 1959b Phil. Mag. 4, 1356.

Silcox, J. and Whelan, M.J. 1960 Phil. Mag. 5, 1.

Simpson, H.M. and Chaplin, R.L. 1969 Phys. Rev. 185, 958.

Smallman, R.E., Westmacott, K.H. and Colley, J.H. 1959-60 J. Inst. Metals 88, 127.

Spring, M.S. 1970 Private communication.

Staubwasser, W. 1959 Acta metall. 7, 43.

Steeds, J.W. 1966 Proc. Roy. Soc. Lond. A. 292, 343.

Steeds, J.W. 1967a Phil. Mag. 16, 771.

Steeds, J.W. 1967b Phil. Mag. 16, 785.

Strudel, J.L. and Washburn, J. 1964 Phil. Mag. 9, 491.

Stubičar, M., Kunstelj, D. and Bonefačić, A. 1970 J. Inst. Metals 98, 64.

Suzuki, H., Ikeda, S. and Takeuchi, S. 1956 J. Phys. Soc. Japan 11, 382.

Takamura, J.-I. 1965 "Lattice defects in quenched metals", p.521 New York : Academic Press.

Tegart, W.J. McG. 1959 "The electrolytic and chemical polishing of metals" Oxford : Pergamon Press.

Tetelman, A.S. 1962 Acta metall. 10, 813.

Thomas, G. 1959 Phil. Mag. 4, 1213.

Thomas, G. and Washburn, J. 1963 Rev. Mod. Phys. 35, 992.

Thomas, G. and Whelan, M.J. 1959 Phil. Mag. 4, 511.

Thomas, L.E. and Balluffi, R.W. 1967 Phil. Mag. 15, 1117.

Thompson, M.W. 1969 "Defects and radiation damage in metals" Cambridge : University Press.

Thompson, N. 1953 Proc. Phys. Soc. B. 66, 431.

Thomson, R.M. and Balluffi, R.W. 1962 J. appl. Phys. 33, 803.

Tomlinson, H.M. 1958 Phil. Mag. 3, 867.

Tunstall, W.J. 1969 Phil. Mag. 20, 701.

Tweet, A.G. 1958 J. appl. Phys. 29, 1520.

Vandervoort, R. and Washburn, J. 1960 Phil. Mag. 5, 24.

Venables, J.D. and Lye, R.G. 1969 Phil. Mag. 19, 565.

Washburn, J. 1963 "Electron microscopy and strength of crystals", p.301. New York : Interscience.

Washburn, J., Groves, G.W., Kelly, A. and Williamson, G.W. 1960 Phil. Mag. 5, 991.

Weertman, J. 1957 Phys. Rev. 107, 1259.

Weertman, J. and Weertman, J.R. 1964a "Elementary dislocation theory", p.15. New York : Macmillan.

Weertman, J. and Weertman, J.R. 1964b Ibid., p.47.

Westdrop, W., Kimura, H. and Maddin, R. 1964 Acta metall. 12, 495.

Westmacott, K.H., Barnes, R.S., Hull, D. and Smallman, R.E. 1961 Phil. Mag. 6, 929.

Whelan, M.J. 1958 Proc. Roy. Soc. Lond. A. 249, 114.

Whelan, M.J. 1965a J. appl. Phys. 36, 2099.

Whelan, M.J. 1965b J. appl. Phys. 36, 2103.

Wilkens, M. and Hornbogen, E. 1964 Phys. Stat. Sol. 4, 557.

Yoshida, S., Kiritani, M. and Shimomura, Y. 1963 J. Phys. Soc. Japan 18, 175.

Yoshida, S., Shimomura, Y. and Kiritani, M. 1962 J. Phys. Soc. Japan 17, 1196.

Yoshioka, H. 1957 J. Phys. Soc. Japan 12, 618.

Ytterhus, J.A. and Balluffi, R.W. 1965 Phil. Mag. 11, 707.